ALMA MATER STUDIORUM
UNIVERSITÀ DEGLI STUDI DI BOLOGNA

FACOLTÀ DI SCIENZE MATEMATICHE, FISICHE E NATURALI

Dottorato di Ricerca in

Scienze Ambientali: Tutela e Gestione delle Risorse Naturali

XX Ciclo

GEO/02 Geologia stratigrafica e sedimentologica

TUZLA CITY (BIH): AN EXAMPLE OF GEOHAZARD INDUCED BY SALT EXTRACTION

Tesi presentata da: Dott. Francesco Stecchi

Coordinatore:
Prof. Carlo Ferrari

Tutore: Prof. Giovanni Gabbianelli

Relatori: Prof. Marco Antonellini

Dott. Francesco Mancini

Esame finale anno 2008

INDEX

INTRODUCTION

Salt deposits characterize the subsurface of Tuzla (BiH) and made it famous since the ancient times. Archeological discoveries demonstrate the presence of a Neolithic pile-dwelling settlement related to the existence of saltwater springs that contributed to make the most of the area a swampy ground.

Since the Roman times, the town is reported as “the City of Salt deposits and Springs”; "tuz" is the Turkish word for salt, as the Ottomans renamed the settlement in the 15th century following their conquest of the medieval Bosnia (Donia and Fine, 1994). Natural brine springs were located everywhere and salt has been evaporated by means of hot charcoals since pre-Roman times.

The ancient use of salt was just a small exploitation compared to the massive salt production carried out during the 20^{th} century by means of classical mine methodologies and especially wild brine pumping.

In the past salt extraction was practised tapping natural brine springs, while the modern technique consists in about 100 boreholes with pumps tapped to the natural underground brine runs, at an average depth of 400-500 m. The mining operation changed the hydrogeological conditions enabling the downward flow of fresh water causing additional salt dissolution.

This process induced severe ground subsidence during the last 60 years reaching up to 10 meters of sinking in the most affected area. Stress and strain of the overlying rocks induced the formation of numerous fractures over a conspicuous area (3 Km^2). Consequently serious damages occurred to buildings and infrastructures such as water supply system, sewage networks and power lines.

Downtown urban life was compromised by the destruction of more than 2000 buildings that collapsed or needed to be demolished causing the resettlement of about 15000 inhabitants (Tatić, 1979).

Recently salt extraction activities have been strongly reduced, but the underground water system is returning to his natural conditions, threatening the flooding of the most collapsed area.

During the last 60 years local government developed a monitoring system of the phenomenon, collecting several data about geodetic measurements, amount of brine pumped, piezometry, lithostratigraphy, extension of the salt body and geotechnical parameters. A database was created within a scientific cooperation between the municipality of Tuzla and the city of Rotterdam (D.O.O. Mining Institute Tuzla, 2000).

The scientific investigation presented in this dissertation has been financially supported by a cooperation project between the Municipality of Tuzla, The University of Bologna (CIRSA) and the Province of Ravenna. The University of Tuzla (RGGF) gave an important scientific support in particular about the geological and hydrogeological features.

Subsidence damage resulting from evaporite dissolution generates substantial losses throughout the world, but the causes are only well understood in a few areas (Gutierrez et al., 2008).

The subject of this study is the collapsing phenomenon occurring in Tuzla area with the aim to identify and quantify the several factors involved in the system and their correlations.

Tuzla subsidence phenomenon can be defined as geohazard, which represents the consequence of an adverse combination of geological processes and ground conditions precipitated by human activity with the potential to cause harm (Rosenbaum and Culshaw, 2003).

Where an hazard induces a risk to a vulnerable element, a risk management process is required.

The single factors involved in the subsidence of Tuzla can be considered as hazards. The final objective of this dissertation represents a preliminary risk assessment procedure and guidelines, developed in order to quantify the buildings vulnerability in relation to the overall geohazard that affect the town.

The historical available database, never fully processed, have been analyzed by means of geographic information systems and mathematical interpolators (PART I).

Modern geomatic applications have been implemented to deeply investigate the most relevant hazards (PART II). In order to monitor and quantify the actual subsidence rates, geodetic GPS technologies have been implemented and 4 survey campaigns have been carried out once a year.

Subsidence related fractures system has been identified by means of field surveys and mathematical interpretations of the sinking surface, called curvature analysis. The comparison of mapped and predicted fractures leaded to a better comprehension of the problem. Results confirmed the reliability of fractures identification using curvature analysis applied to sinking data instead of topographic or seismic data.

Urban changes evolution has been reconstructed analyzing topographic maps and satellite imageries, identifying the most damaged areas. This part of the investigation was very important for the quantification of buildings vulnerability.

Risk map of Tuzla has been created by means of map algebra calculus that leads to the identification of 5 risk classes

The complexity of the phenomena occurring in Tuzla needed an interdisciplinary approach to identify possible intervention strategies and to delineate the zone where new buildings construction should be forbidden.

PART I

1. STUDY AREA DESCRIPTION

1.1. GENERAL SETTINGS

Tuzla is located in the northeastern part of Bosnia and Herzegovina, settled just underneath the Majevica mountain range at an average height of 239 meters above sea level. The central zone is situated in the plain of the Jala river, with residential areas in the north and south of the city located on the Ilinčica, Kicelj and Gradina hills (Fig. 1.1).

First mentioned in 950 A.D. as a county under Hungarian rule, the town was later referred by historians to “Soli” that means "salts" in the Bosnian, Croatian or Serbian language (Donia and Fine, 1994).

However, there is enough archaeologic evidence to suggest that Tuzla was a rich Neolithic settlement, and hence inhabited continuously for more than 6000 years which makes Tuzla one of the oldest European settlements with sustained living (Bakalović, 2005).

The 2nd of October 1943, Tuzla became the largest liberated town in Europe. It developed into a major industrial and cultural centre during the communist period in former Yugoslavia. In the 1990 elections the Reformists won, and Tuzla was the only municipality in Bosnia where non-nationalists won.

During the Bosnian war, 1992-1995 the town was the only municipality not governed by nationalist authorities, and was besieged by Serb nationalist forces.

Additionally, the town was not spared the atrocities of war. On May 25, 1995, a Serb artillery shell killed 71 youngsters in Kapija square, causing the most deadly shelling of the war in Bosnia and Herzegovina.

After Sarajevo and Banja Luka, Tuzla is nowadays the third largest city in Bosnia and Herzegovina, and the seat of the Tuzla Canton and Tuzla Municipality; administratively, Tuzla is divided into 39 local districts and is currently estimated to have 160,000 inhabitants.

Tuzla is one of the largest industrial cities of Ex-Yugoslavia including a 3.5 Terawatt coal power plant, coal mines, salt mines, and lime factories.

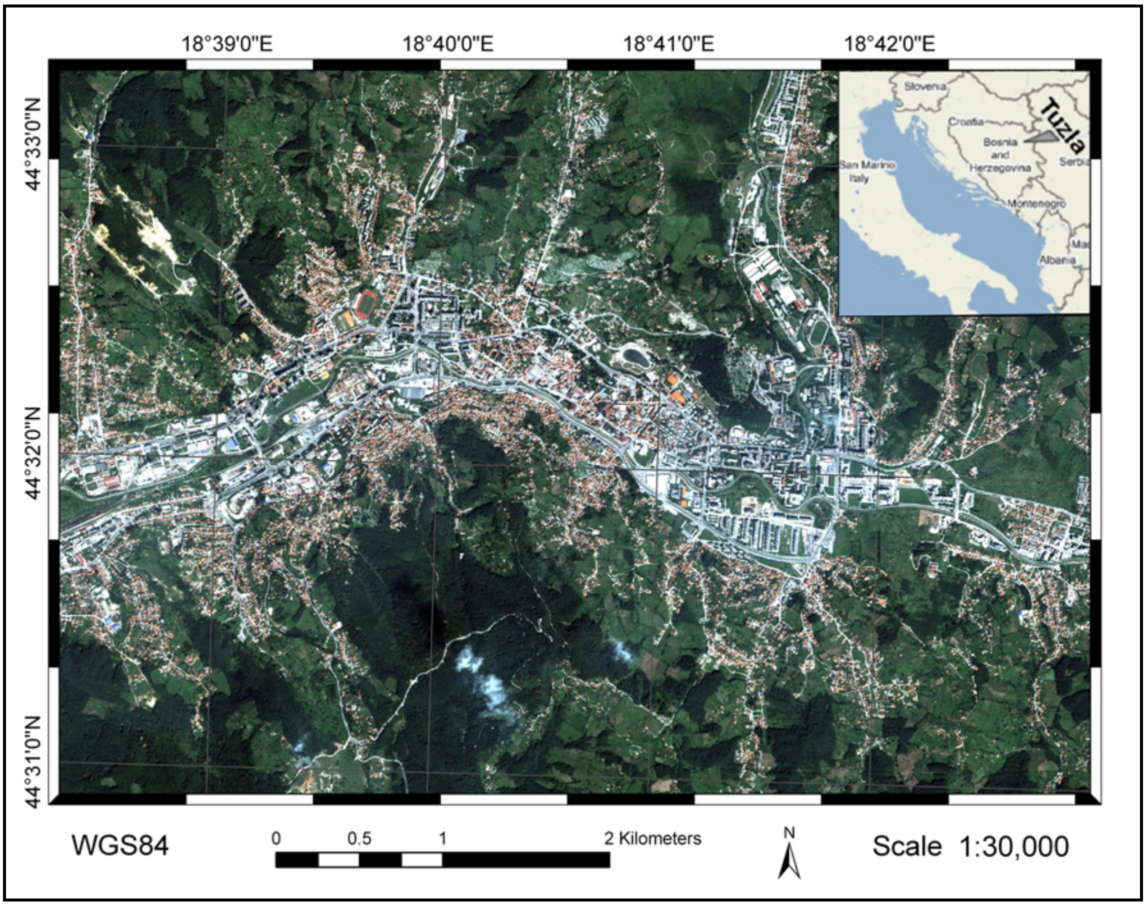

Fig. 1.1: Tuzla city captured in a Quickbird satellite image (2005).

1.2. TECTONICS, GEOLOGY AND STRATIGRAPHY

Tuzla formations are part of the South Pannonian Basin fill. This Neogene basin has been interpreted as a retroarc basin that started by a rifting processes in the Paratethys at the beginning of the Early Miocene.

The Neogene succession consists of limestones, marls, sandstones, and salt of Aquitanian-Burdigalian age (Late Egerian, Eggenburgian, Otthnangian and Karpatian following the Central Paratethyan stratigraphic division; Hrvatović, 2006).

After the termination of the rifting and volcanic activity in the Badenian, slow subsidence continued till the end of the Sarmatian, when a marine regression produced a regional unconformity. Marine conditions were restored in the Early Pannonian as reveals the 600 m thick marl and clayey limestone successions deposited in stagnant, anoxic, carbon-rich, deep basinal areas.

During the Pannonian, tectonic compression produced folds and reverse faults with a dominant N-NE vergence. The depositional environments changed into freshwater basins during the late Pannonian. late Pannonian and early Pontian turbidites are overlain by late Pontian prograding delta slope, delta front and delta flat clastics.

These sequences of interbedded sandstones, siltstones and marls reach the maximum thicknesses of more than 1500 m in the Sava Depression and 2000 m in the Drava Depression.

The Pliocene deposits, composed of various types of mostly unconsolidated sediments, reach their maximum thickness in the middle part of the Drava Depression (Tari and Pamić, 1998) (Fig. 1.2).

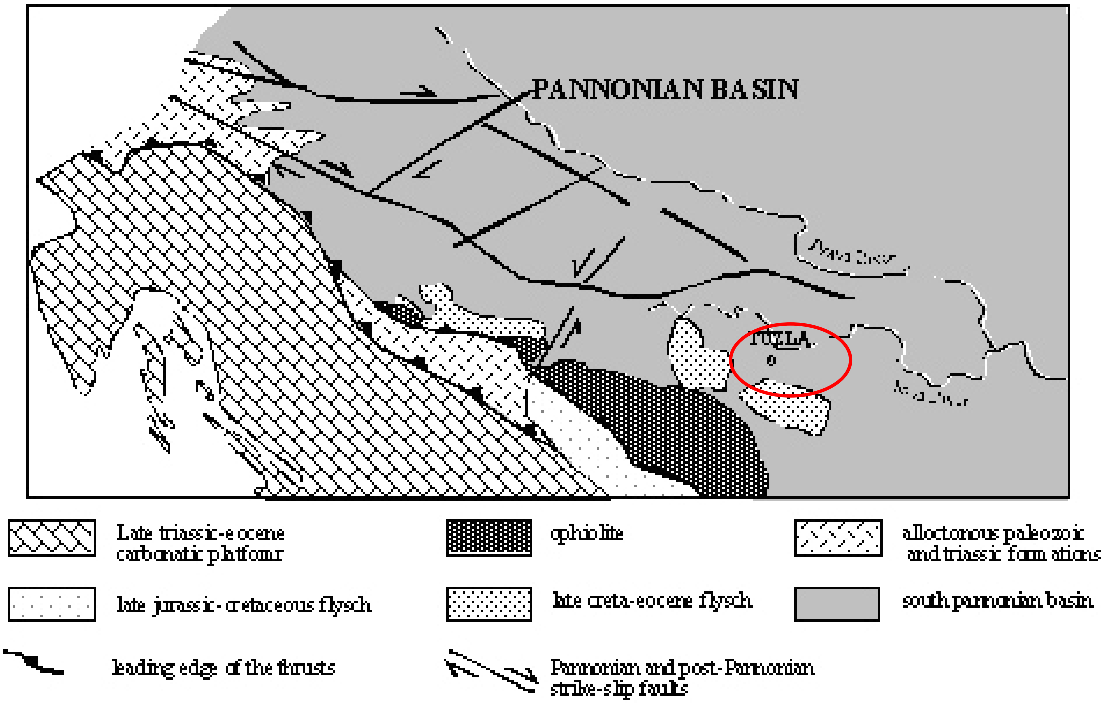

Fig. 1.2: major tectonic features of the study area (Tari and Pamić, 1998; modified.)

Figure 1.3 shows that the salt formations located beneath the city of Tuzla and surrounding areas. They are located beneath the northern part of the town (Tusanj, Hukalo and Trnovac areas) and has an ellipsoidal shape covering about 2 km^2.

The bedrock geology of the study area consists of Miocene formations affected by x-y trending open folds. The city lies on an E-W oriented plain underlain by alluvial deposits of the Jala River. Middle-Upper Miocene marls and sandstones crop out in the surrounding hills.

Detailed description of the geology of Tuzla based on exploration boreholes data has been published by Hrvatović (2006). More information on the geology that underlies the city of Tuzla has been provided by several authors such as Katzer, 1903; Soklić, 1959; 1964; 1982; Stevanović, 1977, Cicić, 2002; Jovanović; 1980; Vrabać 1999.

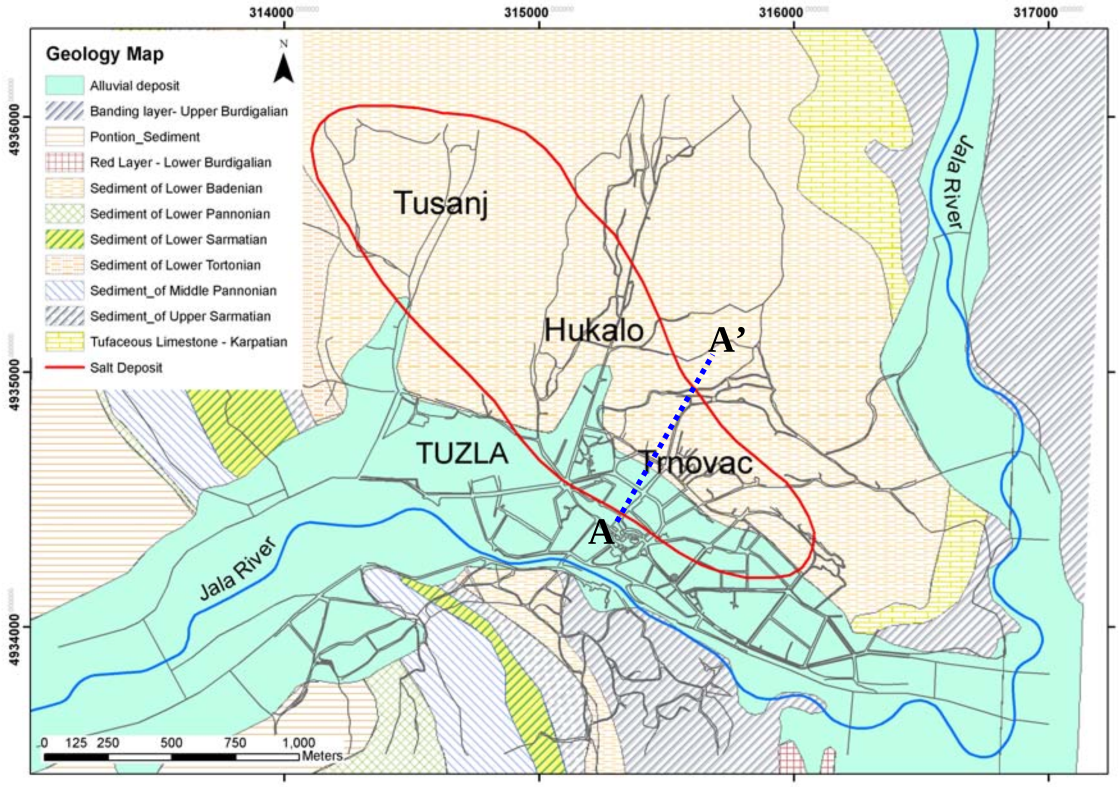

Fig. 1.3: Geological settings of Tuzla area (Redžepović et al., 2005; modified).

Triassic salt formation series date back to Burdigal-Helvetian (Carpathian) age. They are represented with banded marls and marly slates with different stage of schistosity. Banded look is result of alternating replacement of darker and lighter layers (leafs). In these series, composition also presents siltstone, finely grained sandstone, limestone, dolomitic limestone, and tuffs. Halite, anhydrite, gypsum and other evaporites have been created mainly at the same time of marly series. The greatest spread of this formation is located on the northern side of Jala river.

Thickness of evaporite banded series is 400-500 m, and the upper productive part is about 200 m. Considering the salt exploitation within banded series, there are five productive cycles and one non-productive cycle of sedimentation that are labelled from the oldest to the youngest as IV, $\mathrm{III_A}$, $\mathrm{III_B}$, II, and I salt series (Fig. 1.4).

The lowest, IV salt series, lays just over laminated slate and marl, with thickness of about 250 m, which also represents the initial sedimentation of banded series. At some places is frequent a thickness up to 60 m of glauber salt and laminated marl bands, which create wasted intercalation.

Over the IV salt series, marly slates and marls are present, which in upper levels transit into dolomicrite (thickness about 20 m) and represent the floor of the III_A series.

In the slate appear Teri-genetic particles of silty dimensions, coal, pyrite and carbonate, usually pigmented with hematite.

Layer of marl is significantly deformed so the both salt series, in the northwest part of the deposit, have lentil-potbellied shape.

Salt series III_A, reach an average thickness of about 55 m, and are represented by salt rock (halite), with frequent bands of slate and marl. Besides halite, in this series are also found tenardite, while Ca-sulphates (anhydrite and gypsum) are completely absent. Series III_A, present rare minerals such as bradleyite, northupite, nahcolite, probertite and tuzlaite.

These series are also divided in two parts and they are separated by a layer of marl (about 3 meters thick). Lower part starts with a layer of pelite thick about 30 cm, then is mainly composed of pure halite. The upper part is significantly contaminated with bands of marls. At locality of Tušanj, this series have a monocline structure, and in Trnovac area it has expressive monocline form.

Roof of series III_A is a pack of pelite (thickness of about 25 m) banded with marly and clayey dolomicrite and microsparite with thin bands of anhydrite and tenardite.

Salt Series III_B is thick about 31 m and it is separated with marls and besides sporadic concentration of salt, it presents stratified form. Over this series of salt, banded marls and slates are deposited, with thickness up to 30 m, which represents the immediate floor to series II, which is developed within the whole deposit.

Salt series II have the greatest spread in the deposit, the greatest thickness, the greatest content of NaCl and it is the more exploited deposit for production of salt water and salt rock. It represents the most investigated and studied salt body in the deposit. It is composed of halite, anhydrite and layers of banded marls. The layer of anhydrite separates this series into the upper and lower part, but it is not developed in the whole deposit, occurring only in the southwest edge, where its thickness reaches up to 10 meters.

Salt series I, about 15 m thick, is separated from the previous series by banded marls and pelite with an absolute thickness of about 40 m. This series of salt is relatively small in spread so in the bigger part of the deposit it can be considered as layer. Poor folding is most probably due to the floor layer that is mainly composed of pelite-tuffite rock with significantly higher hardness and rigidity.

Salt is more considerably concentrated at some places in Tušanj area, the southwest limit of the deposit. The main part of series I have been drilled for exploitation of salt water at the mining district of Hukalo-Trnovac. Drillings also exploited pelite (it contains 44% NaCl), and it has the biggest influence to previous settlement of the terrain.

All series have been drilled for brine exploitation along one century, and at their edges, due to decreased salt mass, breccia has formed from banded marls, as consequence of marls collapses from the roof to the empty spaces leaved by salt rock dissolution.

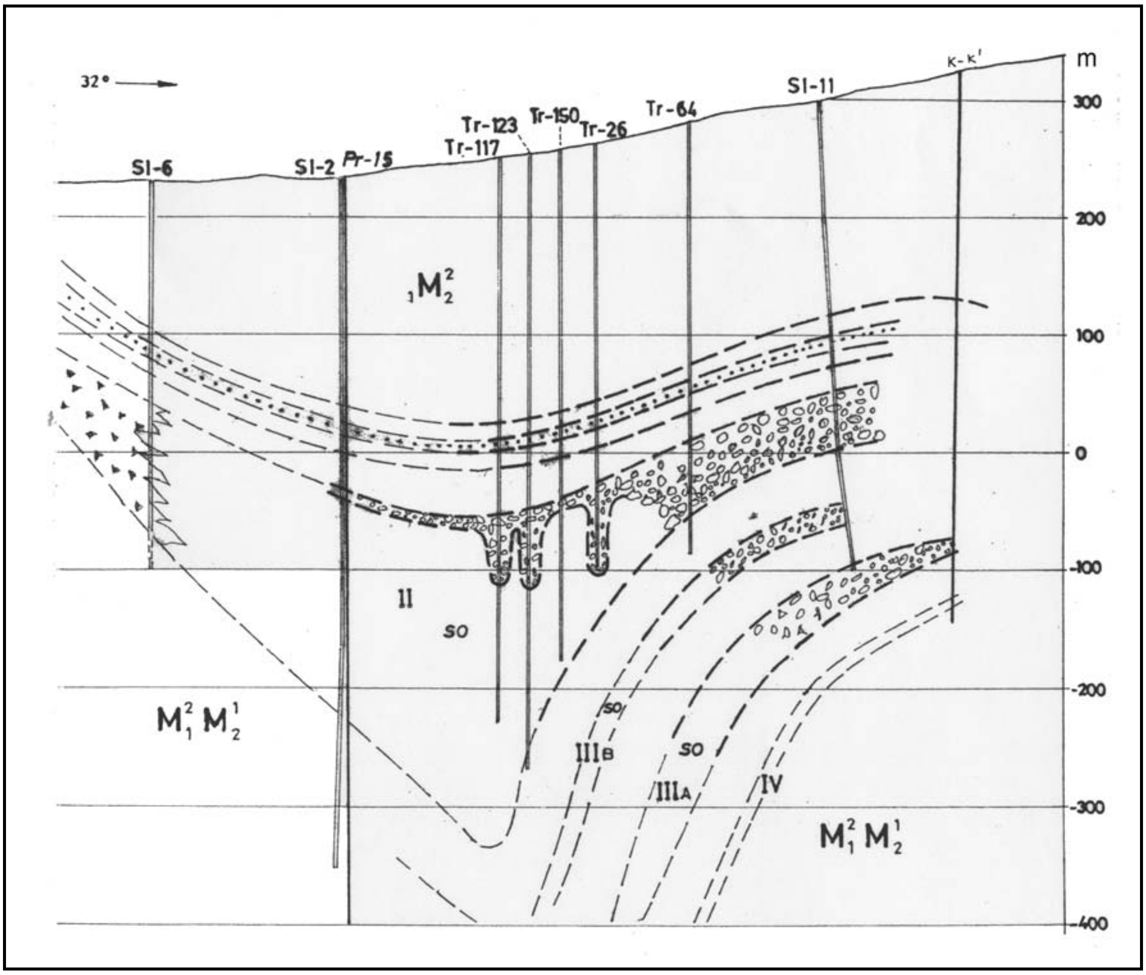

Fig. 1.4: Geological profile AA' (modified from Redžepović et al. 2005). Location of the profile is shown in fig. 1.3. Salt series are labelled as II, III_B, III_A, IV. Seies I is not present along this profile. Geological abbreviations are explained in fig. 1.5.

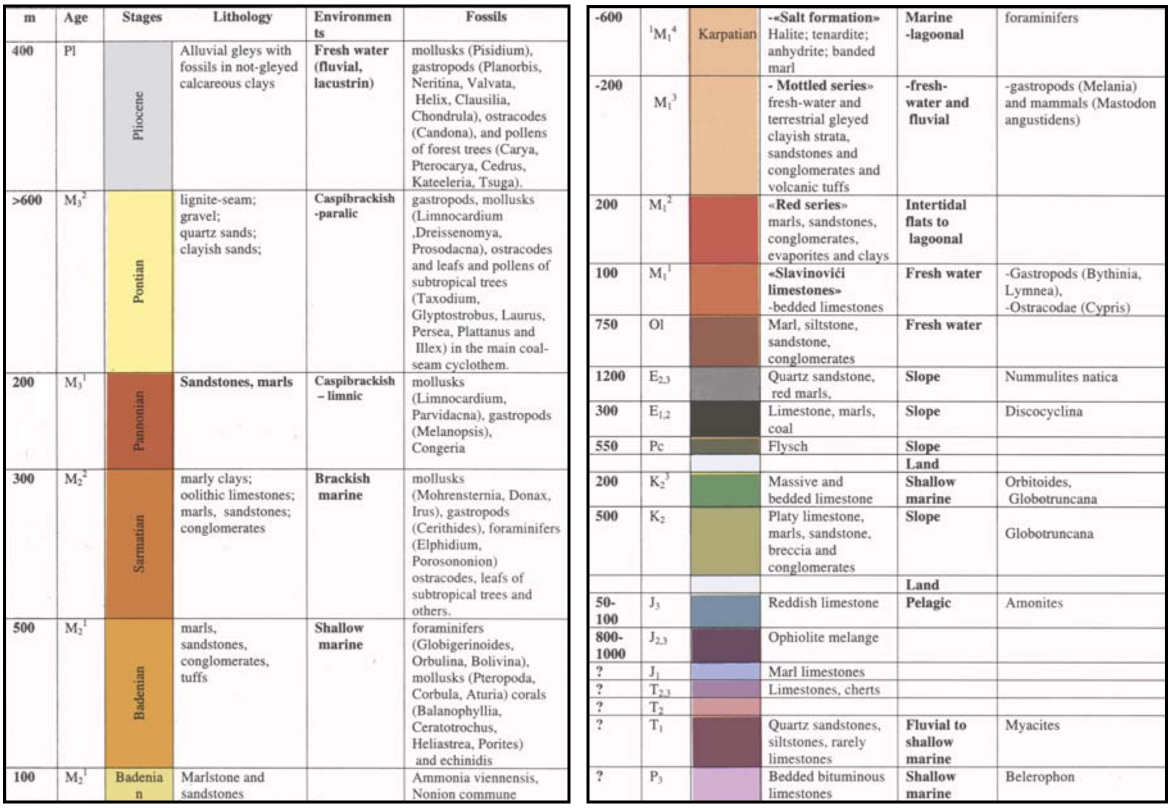

m	Age	Stages	Lithology	Environments	Fossils
400	Pl	Pliocene	Alluvial gleys with fossils in not-gleyed calcareous clays	**Fresh water (fluvial, lacustrin)**	mollusks (Pisidium), gastropods (Planorbis, Neritina, Valvata, Helix, Clausilia, Chondrula), ostracodes (Candona), and pollens of forest trees (Carya, Pterocarya, Cedrus, Kateeleria, Tsuga).
>600	M_3^2	Pontian	lignite-seam; gravel; quartz sands; clayish sands;	**Caspibrackish -paralic**	gastropods, mollusks (Limnocardium ,Dreissenomya, Prosodacna), ostracodes and leafs and pollens of subtropical trees (Taxodium, Glyptostrobus, Laurus, Persea, Plattanus and Illex) in the main coal-seam cyclothem.
200	M_3^1	Pannonian	**Sandstones, marls**	**Caspibrackish – limnic**	mollusks (Limnocardium, Parvidacna), gastropods (Melanopsis), Congeria
300	M_2^2	Sarmatian	marly clays; oolithic limestones; marls, sandstones; conglomerates	**Brackish marine**	mollusks (Mohrensternia, Donax, Irus), gastropods (Cerithides), foraminifers (Elphidium, Porosononion) ostracodes, leafs of subtropical trees and others.
500	M_2^1	Badenian	marls, sandstones, conglomerates, tuffs	**Shallow marine**	foraminifers (Globigerinoides, Orbulina, Bolivina), mollusks (Pteropoda, Corbula, Aturia) corals (Balanophyllia, Ceratotrochus, Heliastrea, Porites) and echinidis
100	M_2^1	Badenian	Marlstone and sandstones		Ammonia viennensis, Nonion commune
-600	$^1M_1^4$	Karpatian	**-«Salt formation»** Halite; tenardite; anhydrite; banded marl	**Marine -lagoonal**	foraminifers
-200	M_1^3		**- Mottled series»** fresh-water and terrestrial gleyed clayish strata, sandstones and conglomerates and volcanic tuffs	**-fresh-water and fluvial**	-gastropods (Melania) and mammals (Mastodon angustidens)
200	M_1^2		**«Red series»** marls, sandstones, conglomerates, evaporites and clays	**Intertidal flats to lagoonal**	
100	M_1^1		**«Slavinovići limestones»** -bedded limestones	**Fresh water**	-Gastropods (Bythinia, Lymnea), -Ostracodae (Cypris)
750	Ol		Marl, siltstone, sandstone, conglomerates	**Fresh water**	
1200	$E_{2,3}$		Quartz sandstone, red marls,	**Slope**	Nummulites natica
300	$E_{1,2}$		Limestone, marls, coal	**Slope**	Discocyclina
550	Pc		Flysch	**Slope**	
				Land	
200	K_2^3		Massive and bedded limestone	**Shallow marine**	Orbitoides, Globotruncana
500	K_2		Platy limestone, marls, sandstone, breccia and conglomerates	**Slope**	Globotruncana
				Land	
50-100	J_3		Reddish limestone	**Pelagic**	Amonites
800-1000	$J_{2,3}$		Ophiolite melange		
?	J_1		Marl limestones		
?	$T_{2,3}$		Limestones, cherts		
?	T_2				
?	T_1		Quartz sandstones, siltstones, rarely limestones	**Fluvial to shallow marine**	Myacites
?	P_3		Bedded bituminous limestones	**Shallow marine**	Belerophon

Fig. 1.5: Stratigraphic column of Tuzla Basin after Soklić 1964, Cicić 2002, Vrabac 1999 (Hratović, 2006; modified).

1.3. SALT EXPLOITATION HISTORY

Tuzla had an important and rich Neolithic pile-dwelling settlement, among the oldest ones in Europe; the creation of this settlement in the area where today is Tuzla, can be related to the existence of saltwater springs which, together with the Jala river have contributed to make the most of the area a swampy ground.

By building pile-dwellings, the Neolithic populations had secured themselves from floods, whilst controlling and exploiting saltwater wells; that is confirmed by the discovery of 3500 BC ceramic fragments of holders which has been used to boil saltwater into salt over hot charcoal (Bakalović, 2005).

Starting with the exploitation of natural brine, these saline spring sites later became the focus for shallow mining and near-surface brine extraction.

The method consist in drill wells or boreholes to intersect the near surface “brine runs”, a technique that is called “wild” brine extraction and which exacerbated the salt karstification (Arup Geotechnics, *1990*; Calvert, *1915*; Collins, *1971*).

The exploitation has been carried out by means of 150 boreholes with pumps tapped to the natural underground brine runs, at an average depth of 200-300 m (Fig. 1.6).

The same exploitation processes are mentioned by Bell (1975) who reported: “natural brine springs were exploited in the valleys of the Weaver and Dane (UK) in medieval times and up to the seventeenth century brine was readily accessible from brine springs which overflowed at the surface”.

However, with increasing output of salt, the brine level fell which meant that pits and wells replaced the brine springs and as the exploitation proceeded these had to be sunk deeper and deeper.

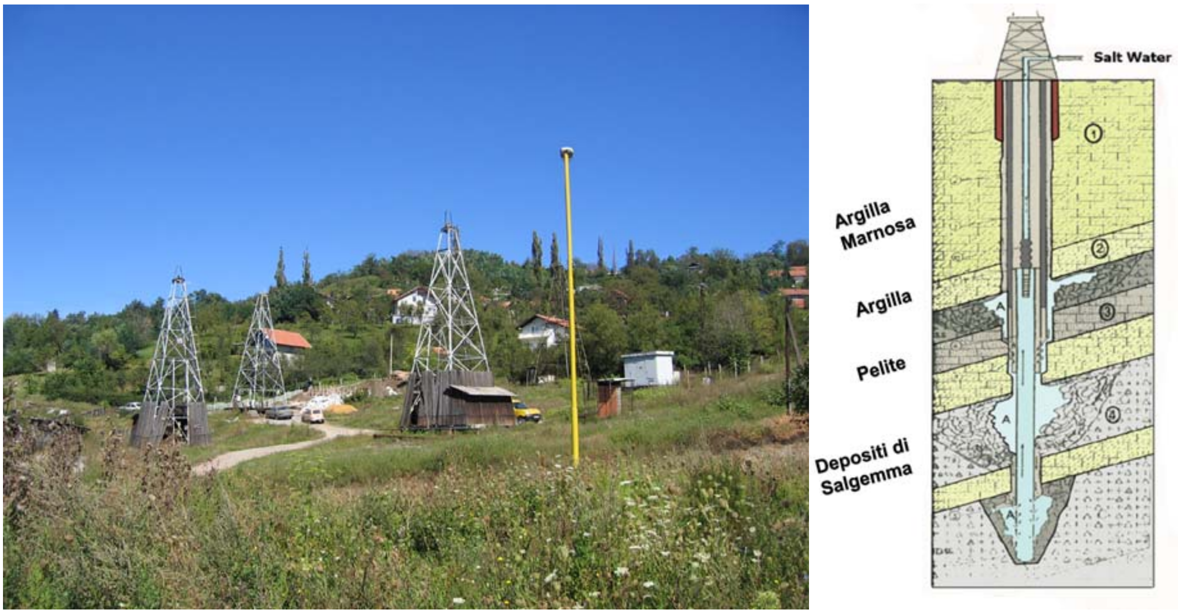

Fig. 1.6: Salt wells in the suburban of Tuzla and scheme of extraction

1.4. SOLUTION MINING SUBSIDENCE

The dissolution of soluble rocks and deposits at the surface, or in the subsurface combined with internal erosion and deformational processes, can produce closed depressions called sinkholes or dolines. These hollows characterize karst landscapes and are usually subcircular in plan, varying in size up to hundreds of meters across and typically from a few meters to tens of meters deep (Williams, 2003).

The word *doline*, derived from the Slavic word dolina, is a term mainly used by European geomorphologists. The term *sinkhole* is most commonly used in the international literature when dealing with engineering and environmental issues.

The generation of these karstic depressions is related to the dissolution of carbonate and evaporitic rocks (Gutierrez et al., 2008).

Because of the higher solubility and lower mechanical strength of evaporites, their susceptibility to sinkhole formation is greater than that of carbonate karst terrains.

The equilibrium solubilities of gypsum ($CaSO_4 \cdot 2H_2O$) and halite (NaCl) in distilled water are 2.4 and 360 g/l, respectively. By comparison, the solubilities of calcite and dolomite minerals in natural environments are commonly lower than 0.5 g/l, depending on the pH, which is largely controlled by the CO_2 partial pressure (Ford and Williams, 1989).

In addition, the evaporites tend to have a more ductile rheology than carbonate rocks, and their common lower strength may be reduced substantially on a human time scale by dissolution processes. Another peculiarity of evaporite karst is that subjacent dissolution may cause ground subsidence on a regional scale. When these subsidence phenomena occur over long time periods, they produce gravitational morphostructures, which may be up to several kilometers in extent and hundreds of meters in structural relief (Gutierrez et al., 2008).

Subsidence problems caused by natural or man-induced dissolution of evaporites have been documented in several European countries.

Papers dealing with such phenomena have been published by Bell (1975) and Cooper (1996, 2002), who studied several cases in Great Britain related to the Permian and Triassic evaporitic (halite deposits) terrain affected by natural and artificial dissolution that produced karstic landforms and subsidence, and by Reuter and Stoyan (1993) who investigated sinkholes in karst regions in Germany.

Large impact of natural Triassic and Tertiary evaporates dissolution have been widely investigated in Spain by Gutiérrez et al. (2001; 2001; 2002). Gutiérrez and Gutiérrez (1998), Gutiérrez-Santolalla et al. (2005) and Soriano and Simón (1995; 2002) analyzed the sinkhole formation in the Ebro Basin.

The Ebro basin area has been also investigated by Benito et al. (1998; 2000) who studied the river response to subsidence related to natural evaporite solution.

Subsidence hazards due to karstification has been also reviewed in the United States by Johnson (1997, 2005).

Subsidence related to natural or induced evaporite solution has been investigated in several cities throughout Europe. Sinkhole in the city of Stuttgart (Germany) has been described in

Garleff et al. (1997); Toulemont (1984) studied ground subsidence in the outskirts of Paris in France. In addition, Cooper (1988), Cooper and Walthan (1999) and Paukštys et al. (1999) discussed the effects related to gypsum dissolution at Ripon (North Yorkshire, Great Britain).

Hazards due to evaporite dissolution in Spain have been investigate by Guerrero et al. (2004) and Soriano and Simón (2005) in the Zaragoza area, while Gutiérrez and Cooper (2002) studied the case of Calatayud historical town (NE Spain). The towns of Birai and Pasvalys, north Lithuania, are also affected by subsidence due to dissolution of gypsum (Paukštys et al., 1999) and a study case has been reported by Andrajchouk and Klimchouk (1993) in the western Ukraine.

Several papers have also dealt with subsidence related to conventional or solution mining. Ground deformation on the Vauvert salt mine (France) has been detected by ERS radar interferometry (Raucoules et al., 2003) whereas salt mining and brine extraction effects have been investigated in the Cheshire and Worcestershire areas (Great Britain) by Bell (1975) and Cooper et al. (2002).

There are different kind of sinkholes and the Tuzla case represents a sinkhole generated by the progressive interstratal dissolution of the evaporitic bedrock and the concurrent gradual sagging of the overlying siltstones and marls bedrock. This process can be termed as *caprock sagging sinkholes*.

This type of subsidence, which is particularly frequent in sequences with halite beds, may result in depressions and troughs several kilometers in length (Kirkham et al., 2002).

Subsidence in the city of Tuzla is related to the extraction of salt from subsurface deposits by means of solution mining practised since the beginning of the last century.

The wild brine pumping changed the hydrogeological conditions enabling the downward flow of fresh water and causing additional salt dissolution. The obvious consequence was registered since the '50 when buildings and roads started to be deformed and fractured.

In some cases, as Tuzla as well, collapses occur as slow subsidence of the land surface over period of years, rather than sudden collapses that occur over period of minutes to days (Veni et al., 2001).

Sudden collapses occurred in Tuzla area just one time (in the year 1987) as consequence of temporary fresh water injection via wells, but the subsidence rates that still affects the town are very high because of strong brine exploitation that deeply modified the natural course of salt dissolution, inducing a severe increase in the sinking processes.

Even after the abovementioned studies it is difficult to ascertain whether subsidence is still occurring or not.

Human-induced salt karst is not as widely understood, and its problem can be very significant (Johnson, 2005).

It is not really possible to predict when or where subsidence due to wild brine pumping will occur and it therefore remains a problem (Bell, 1975).

In fact, the identification of areas affected by evaporite-dissolution subsidence is usually a difficult task, because sinkholes are frequently masked by anthropogenic activities, such as filling and development, or by natural aggradation and erosion processes (Gutierrez et al., 2008).

The following chapters deals with the identification of those factors which contribute to make the area of Tuzla an unsolved geohazard phenomenon.

2. HISTORICAL DATA PROCESSING

Since the first signs of ground deformations (the beginning of nineteenth century), the local government started to collect information and data about brine pumping rates, topographic measurements, boreholes, piezometric level, geotechnical investigations.

The several acquired data were just catalogued as a numerical archive.

A more exhaustive and comprehensive database of the collected information was created within a scientific cooperation between the municipality of Tuzla and the city of Rotterdam (The Nederland) in the year 2000 (D.O.O. Mining Institute Tuzla, 2000).

Nevertheless the abovementioned cooperation didn’t fully describe and correlate the several factors involved in the subsidence phenomena.

The first objective of this dissertation has been to obtain a better cataloging and comprehension of the problem by means of geographic information systems; all the following investigations have been developed by means of ArcGIS^{TM} software by ESRI, which permits to link large databases with a geographic visualization interface.

2.1. TOPOGRAPHIC SUBSIDENCE MONITORING

2.1.1 Available data and investigation methodologies

Although the first geodetic surveys dates back to the year 1914, a systematic survey, aimed at measuring subsidence rates, started in the year 1956, when traditional trigonometric and spirit levelling surveys began with annual periodicity and over a dense benchmarks network (around 800 points).

This systematic approach of ground deformation monitoring ended in 1992 because of the Civil Balkan War. In the following decade (from 1992 to 2003) measurement acquisition was very scarce and the evaluation of subsidence rates was not as reliable as in previous times. Starting from the year 2003 field activities were completely stopped.

The fifty years-long altimetric dataset has never been fully processed by means of advanced interpolation procedures.

After a measurements reorganization and cleaning, data (structured in terms of X, Y, Z) have been interpolated by means of different techniques in order to reconstruct respectively the annual and overall subsidence rates. The total of significant sample data amounts to about 400 points.

Particularly careful has been taken when to select the technique for the interpolation of sampling data points.

Many interpolation techniques exist. The question of which is the most appropriate in different contexts has stimulated several comparative studies about interpolation accuracy (Weber and Englund, 1992, 1994; Carrara et al., 1997; Robeson, 1997).

The existing literature, however, tends to be equivocal about which interpolation technique is the most accurate. Some studies (Laslett 1994; Burrough and McDonnell, 1998; Zimmerman et al., 1999; Wilson and Gallant, 2000) indicate that, among the many existing interpolation techniques, geostatistical ones perform better than the others. In particular, Zimmerman et al. (1999) showed that *Kriging* yielded better estimations of elevation than inverse distance weighting (IDW) did, irrespective of the sampling pattern.

This result is probably due to the ability of kriging to take into account the spatial structure of data. However, in other studies (Weber and Englund, 1992; Gallichand and Marcotte, 1993; Brus et al., 1996; Declercq, 1996; Aguilar et al., 2005), neighborhood approaches such as *Inverse Distance Weighted* or *Radial Basis Functions* were as accurate as Kriging or even better (Chaplot et al. 2006).

Tuzla annual subsidence rates have been calculated by means of two different interpolation techniques (TIN and Natural Neighborhood) in order to analyze the different results.

Triangular Irregular Networks (TINs) are nets of triangular facets defined by nodes and edges that cover a surface. TINs are constructed from a set of known values, sometimes called "spot heights" that are used as initial nodes in the triangulation. TINs are usually used to represent terrain surfaces in engineering applications, as the spot heights can be irregularly distributed to accommodate areas of high variability in the surface and their values and exact positions are retained as nodes in the TIN.

The values at locations between nodes can be derived for a TIN using linear interpolation from the nearest nodes. There are different methods of interpolation to form these triangles, such as Delaunay triangulation or distance ordering.

ArcGIS supports the Delaunay triangulation method, which ensures that no vertex lies within the interior of any of the circumcircles of the triangles in the network. If the Delaunay criterion is satisfied everywhere on the TIN, the minimum interior angle of all triangles is maximized. The result is that long, thin triangles are avoided as much as possible (ArcGIS Desktop Help – ESRI 2006).

Natural neighbor interpolation finds the closest subset of input samples to a query point and applies weights to them based on proportionate areas in order to interpolate a value (Sibson, 1981). It is also known as Sibson or “area-stealing” interpolation.

Its basic properties are that it's local, using only a subset of samples that surround a query point, and that interpolated heights are guaranteed to be within the range of the samples used. It does not infer trends and will not produce peaks, pits, ridges or valleys that are not already represented by the input samples.

The surface passes through the input samples and is smooth everywhere except at locations of the input samples. It adapts locally to the structure of the input data, requiring no input from the user pertaining to search radius, sample count, or shape. It works equally well with regularly and irregularly distributed data (Watson, 1992).

Natural Neighborhood estimates surface values for each cell using the value and distance of nearby points; data points used to interpolate the surface values for each cell are identified and weighted using a Delauney triangulation, as in a TIN. Natural Neighbors interpolation reliably works with much larger datasets than the other interpolation methods (ArcGIS Desktop Help – ESRI, 2006).

Due to the high density of usable altimetric points (about 400) compared with the sampled area (approximately 5 Km^2) the TIN, Natural Neighborhood and Radial Basis Function interpolation techniques work good as well, honoring the sampling data, especially considering that, with such high values of annual subsidence, the associated interpolation error is quite irrilevant. From an esthetical point of view, surfaces obtained with natural neighborhood technique have a better layout because they are more smoothed than TIN maps that are accurate but generally sharp.

2.1.2 Subsidence evolution results

Focusing on the topographic surveys performed during the 1956-2003 period, a maximum cumulative subsidence of 12 m has been detected (Fig. 2.1). It produced severe damage to the water supply system, the sewage network and the traffic lines.

From the year 1956 subsidence rates have been rapidly increased, reaching the maximum values at the beginning of the ’70.

Strong ground collapses were persisted until the year 1983 when, due to a consistent reduction in brine pumping activities, subsidence appreciably decreased.

After the 1992 topographic surveys started to be less accurate and detailed, anyway the results of sinking data interpolations still present high subsidence values, especially for urbanized areas.

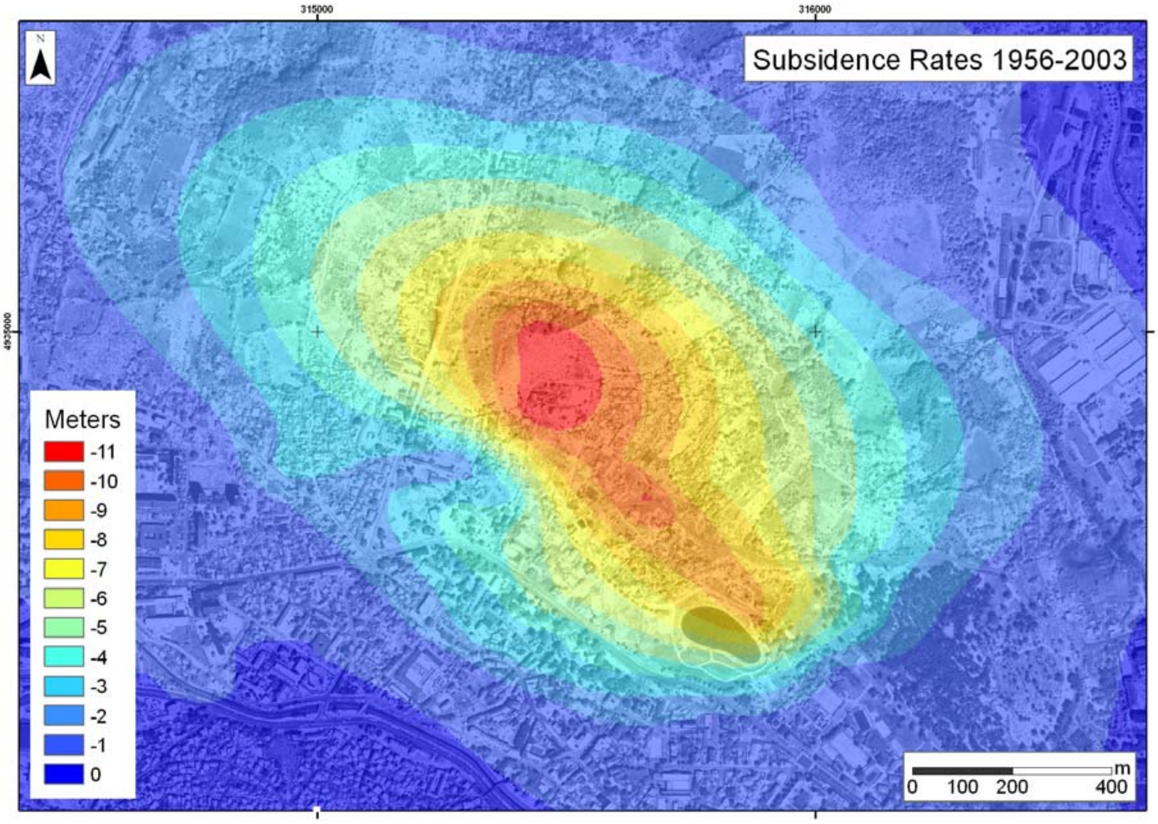

Fig. 2.1: Overall subsidence occurred in the area of Tuzla along the period 1956-2003

2.2. BRINE EXPLOITATION ACTIVITIES

2.2.1 Available data and investigation methodologies

Brine pumping activity data started to be officially collected in the year 1906, and stored as annual m^3 brine per well. The total installed pumping wells are 150, but exploitations have been carried out by means of at most 25 wells simultaneously. In the year 2005 salt exploitation has been stopped, but pumping activities continue in order to prevent the water table rise (see paragraph 2.3).

Wells data have been stored in a database reporting: wells coordinates (UTM-WGS84) and pumping activities per year. This have permitted to import the information in ArcGIS^{TM} software and to display pumping wells superimposed to a satellite image of the area.

2.2.2 Exploitation activities trend

From the year 1906 to the 1950, annual extraction rates were very low (about 170,000 m^3) compared to the strong increase occurred in the second half of the century; the exploitation reached his maximum in the year 1982 with more than 2 million m^3 pumped brine (Fig. 2.2).

Fig. 2.3 shows the location of brine pumping wells in relation to the amount of activities.

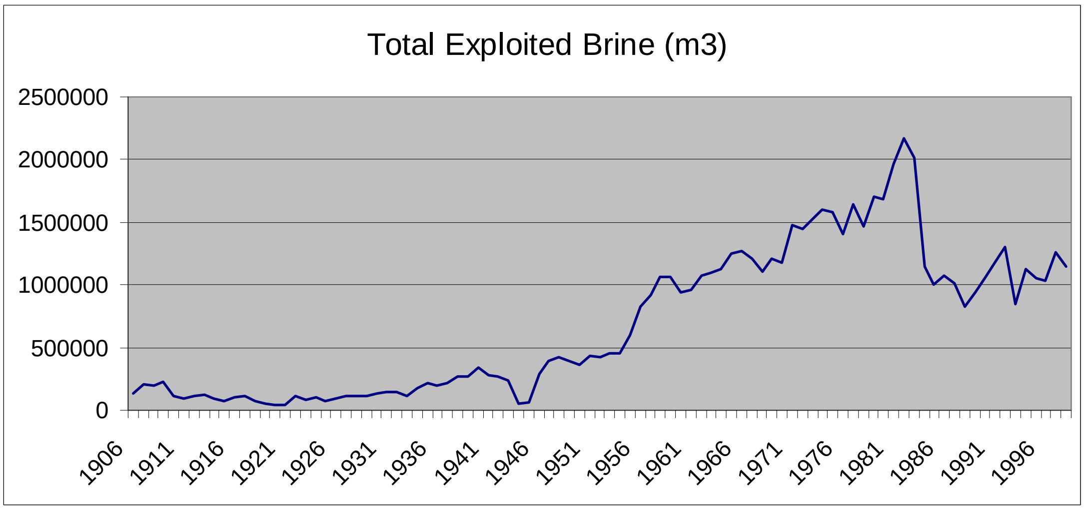

Fig. 2.2: Annual brine exploitation trend for the period 1906-1998.

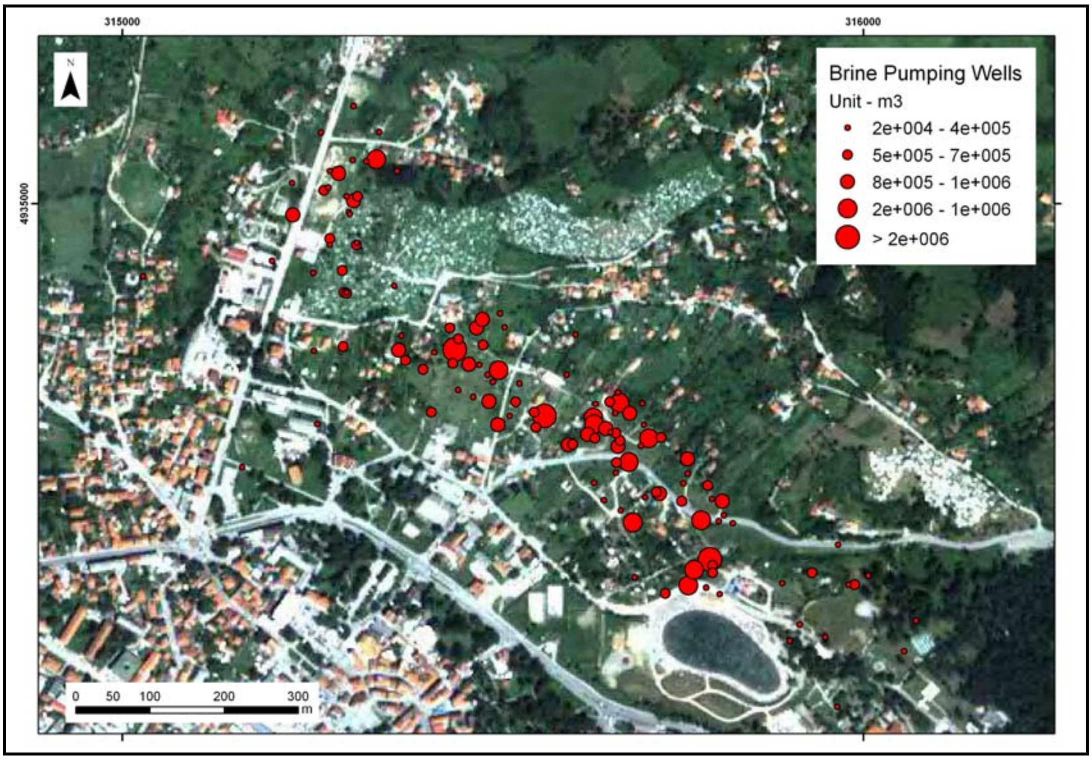

Fig.2.3: Total brine pumping wells used for salt exploitation during the period 1906-1998.

2.3. WATER TABLE MONITORING

2.3.1 Available data and investigation methodologies

Topographic depressions occurring in evaporite karst areas are frequently prone to flooding either by the concentration of surface runoff or by groundwater flooding when the water table rises above their ground level (Gutierrez et al, 2008).

Understanding the hydrogeology of the study area is a crucial aspect of sinkhole hazard analysis. The groundwater flow is the geological agent responsible for the karstification of evaporite rocks and commonly one of the most important conditioning and triggering factors involved in the generation of sinkholes. Numerous aspects need to be investigated, especially the position of the water table (or piezometric level) and how it changes through time and space, naturally or by anthropogenic means. It is important to find out whether the evaporites and the overlying sediments are affected by a downward vadose flow or by a phreatic/artesian flow controlled by the piezometric gradient (Gutierrez et al, 2008).

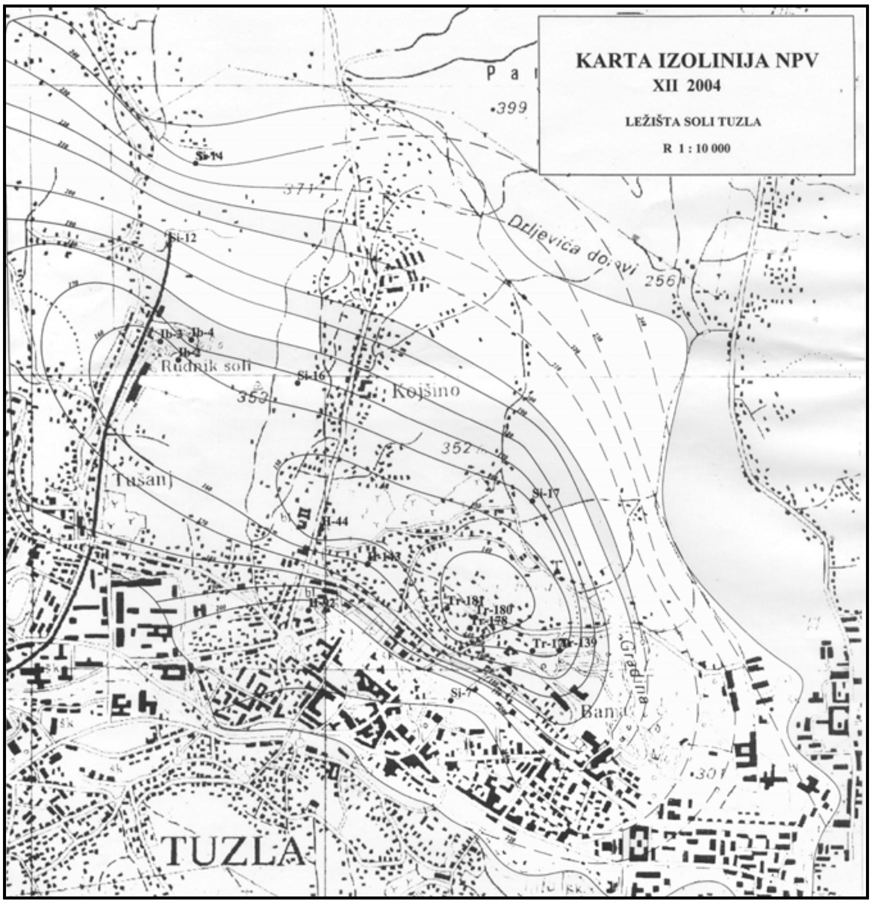

Fig. 2.4: Water table map for the year 2004 obtained by the piezometric monitoring (Oruč et al., 2005).

Wild brine pumping, carried out in Tuzla area along almost 100 years, strongly influenced the groundwater level. A piezometric monitoring carried out by the University of Tuzla (Faculty of Mining, Geology and Civil Engineering) leads to the creation of water table maps respectively for the years 1979, 1985, 1990, 1995, 2000, 2004 (Oruč et al., 2005). An example is reported in fig. 2.4

The most collapsed part of Tuzla is presently subjected to flooding during strong rainfalls (Fig. 2.5), but the biggest threaten is represented by the water table rise that affects the area as consequence of brine pumping suspension.

Fig. 2.5: Flooding in the center of Tuzla after a strong summer rainfall (June 2005).

Isophreatic maps have been digitalized and interpolated by means of ArcGIS^{TM}; the resulted TIN and grid maps allowed the spatial investigation of water table movements during the period 1979-2004.

In order to identify the most flooding-threatened areas of the town, water table levels have been correlated with the available DTMs (Digital Terrain Models) by means of map algebra procedures (ArcGIS Raster Calculator).

ArcGIS Spatial Analyst includes advanced map algebra functions for combining multiple maps, performing suitability analysis, assigning weights, and identifying relationships.

Map algebra is a process of adding, subtracting, multiplying, and dividing maps by applying mathematical operations to map themes. Map algebra utilities allow the user to specify mathematical relationships between map layers. In Tuzla case for example, a new map has been generated by determining the difference in elevation between a topographic map and the corresponding map of the water table.

In practice, a single expression can be constructed to find the combined value of two datasets (Raster1 + Raster2). These algebraic expressions can be simple arithmetic expression or can consist of complex spatial and algebraic functions (Fig. 2.6).

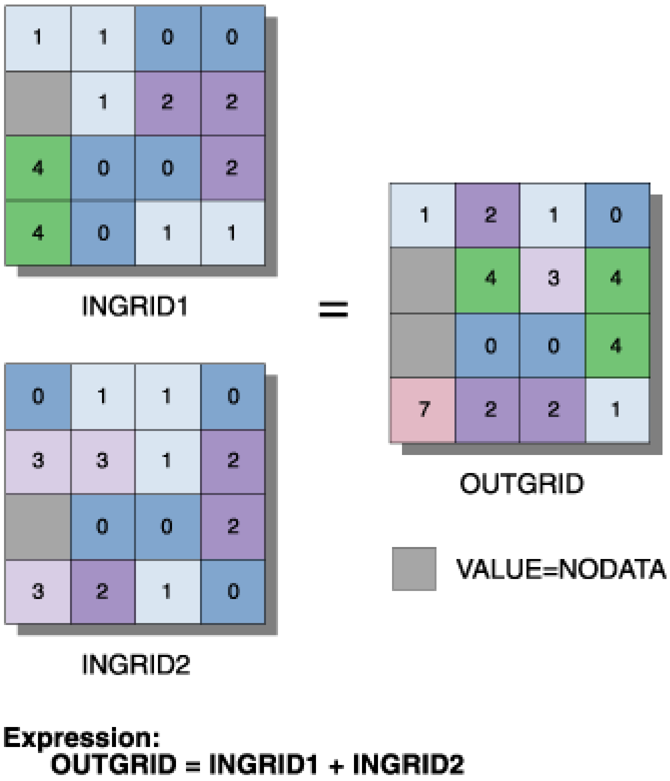

INGRID1

1	1	0	0
▨	1	2	2
4	0	0	2
4	0	1	1

INGRID2

0	1	1	0
3	3	1	2
▨	0	0	2
3	2	1	0

=

OUTGRID

1	2	1	0
▨	4	3	4
▨	0	0	4
7	2	2	1

▨ VALUE=NODATA

Expression:
OUTGRID = INGRID1 + INGRID2

Fig. 2.6: This graphic illustrates how mathematical operators and functions can be used to combine data on a cell-by-cell basis to derive new information.

That allowed the quantification of water table depth below the terrain surface highlighting the areas where the groundwater is close to the surface.

DTM has been extrapolated by the contour lines map of the year 1965 (Fig. 2.7) then adapted to the abovementioned years by means of map algebra procedure (subtraction of the corresponding subsidence surface to the DTM).

The comparison of water table depths of different years has been also carried out by map algebra procedures, that leads to the creation of maps indicating the rates of water table rise.

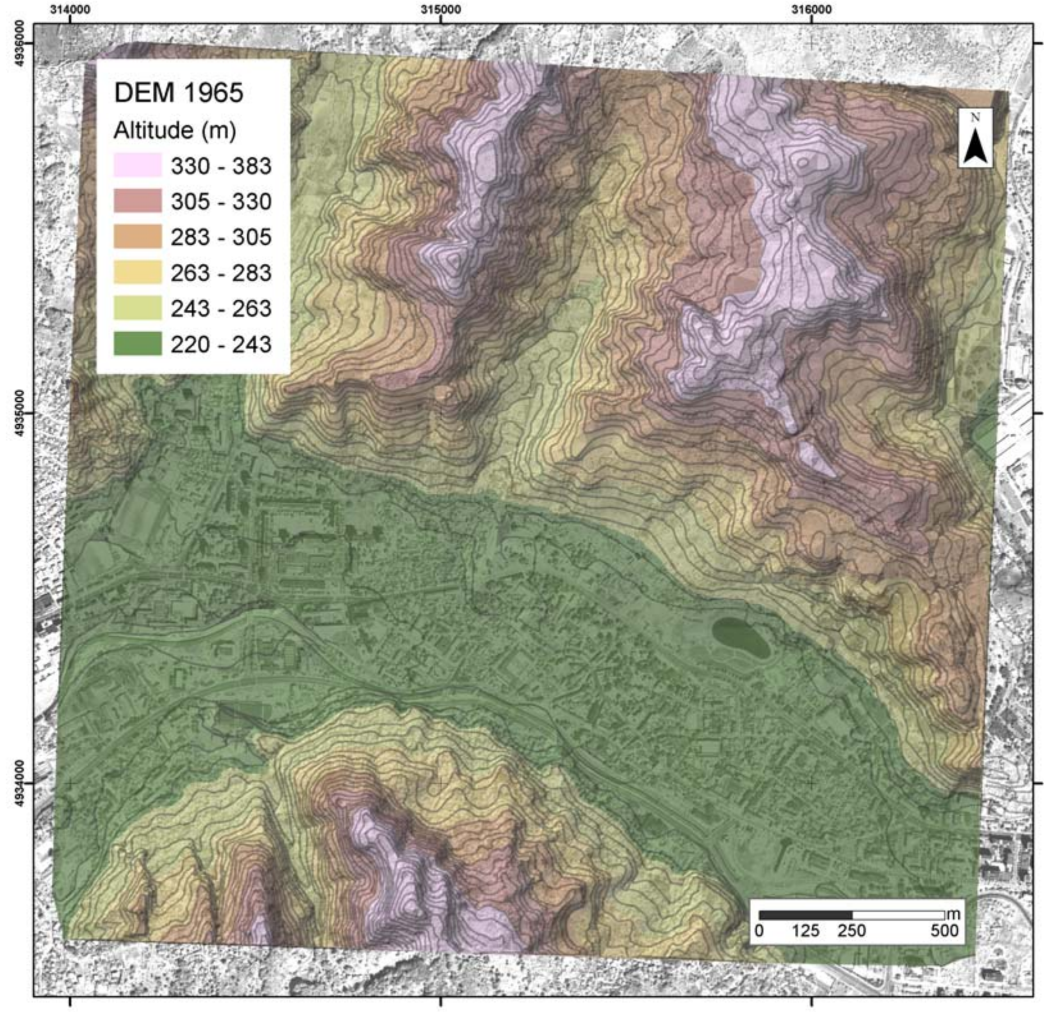

Fig. 2.7: Digital Terrain Model obtained by the interpolation of 1965 contour lines (in grey)

2.3.2 Water table evolution results

The map algebra calculus depicts an intense water table lowering from the year 1979 to 1985, that corresponds to the increased brine pumping activities.

Then, from the year 1985, all the following periods (1990, 1995, 2000 and 2004) present a gradual water table rise that globally have reached about 90 meters in the most affected area (fig. 2.8).

Fig. 2.9 represents a 3D view of the groundwater levels for the years 1985 (light green) and 2004 (blue). Water table in the year 2004 is clearly higher than the year 1985.

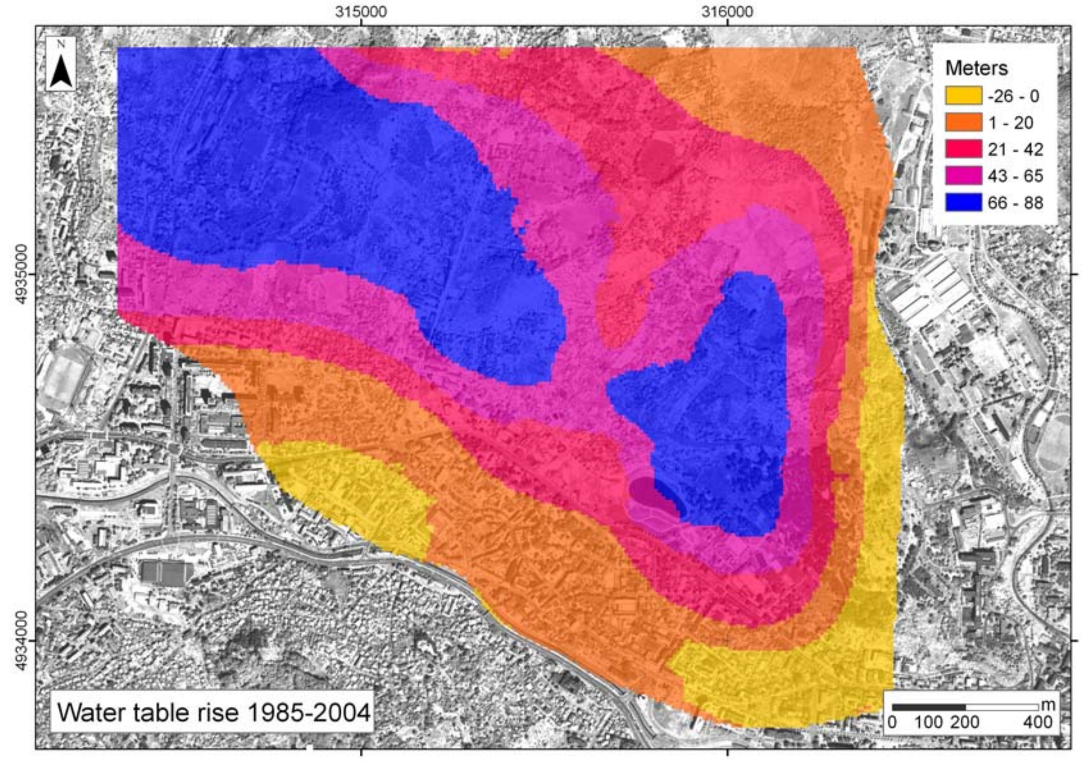

Fig.2.8: Rates of water table rise from the year 1985 to the 2004.

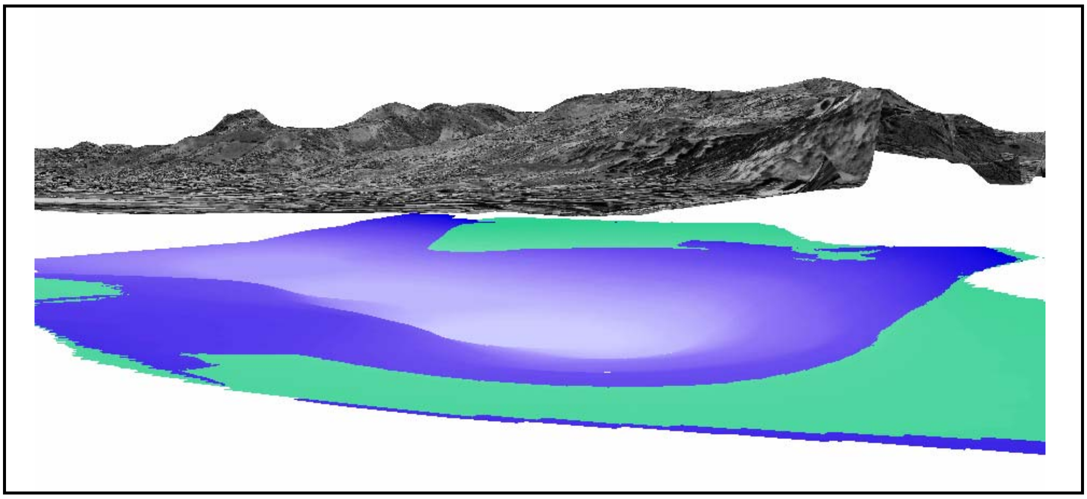

Fig. 2.9: In the year 2004 the water table (in blue) is clearly higher than the year 1985 (in light green) when brine pumping reached the maximum rates. Height values (Z) are exaggerated in order to highlight the water rise process.

2.4. CORRELATION BETWEEN EXPLOITATION AND SUBSIDENCE

2.4.1 Available data and investigation methodologies

In order to investigate the relationship between the rates of subsidence and salt exploitation, annual average rates of subsidence have been compared with the yearly volume of pumped brine.

The annual volume of brine extracted has been derived from the database, whereas an annual mean value of subsidence rate for the 1956-1992 period has been computed from a regular grid with a cell size of 50 m and 338 nodes (see grid cells in figure 2.10).

The first comparison between the distribution of salt wells and the subsidence zone reveals that sinking phenomena affect a wider area compared to wells distribution. Brine wells area covers approximately 1,5 km^2 whilst the subsidence area is around 5 km^2.

In this investigation the subsidence zone considered for the comparison extends over an area of about 2 km^2 because the rest is subjected to very low subsidence that strongly influences the calculus of mean rates.

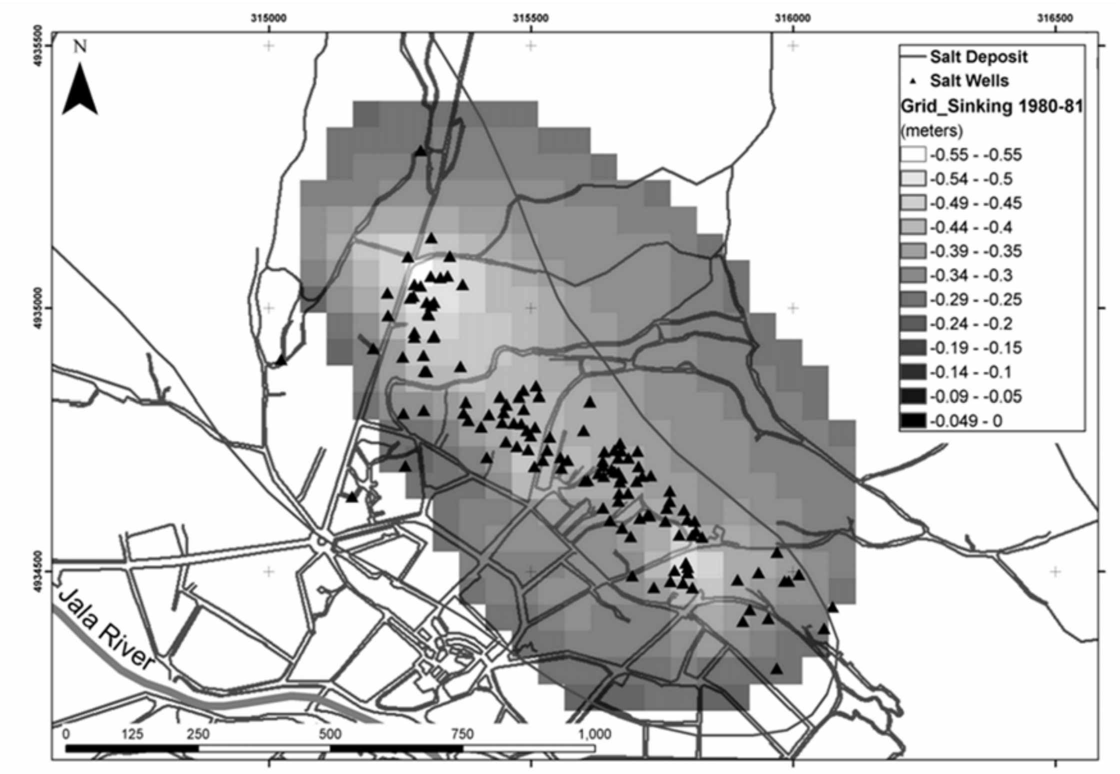

Fig. 2.10: Distribution of salt wells and subsidence rates derived from traditional surveys (plotted as

grey levels) from 1980 to 1981, Rectangles indicate the grid used for the extrapolation of average annual subsidence rates.

2.4.2 Results and considerations

The plot in figure 2.11 represents a comparison between trends of mean yearly subsidence (dashed line) and amount of extracted brine per year (solid line).

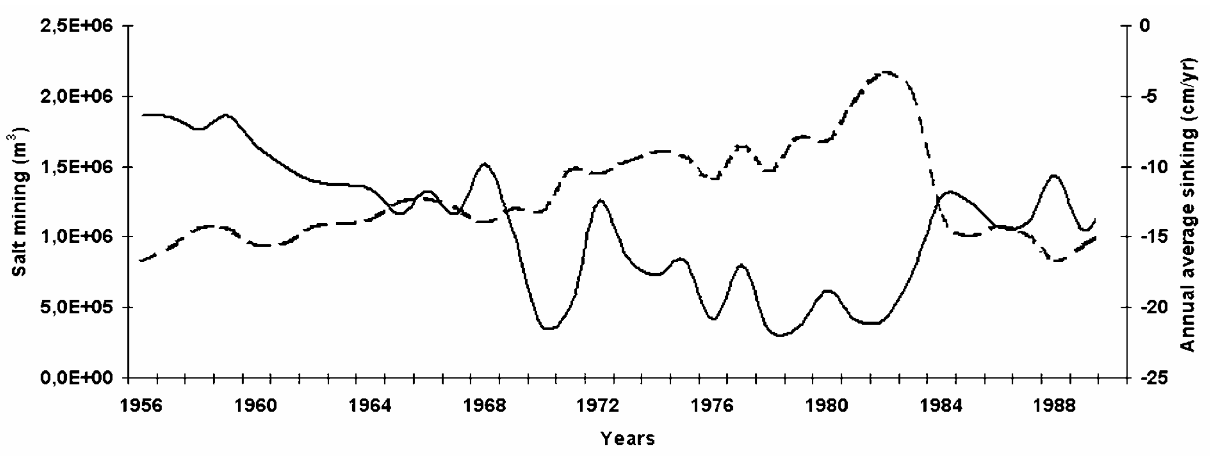

Fig. 2.11: Comparison between the annual volume of exploited salt water (m^3, dashed line) and the average values of annual subsidence rates (cm, solid line) sampled by the gridding procedure.

The correlation between the amount of salt exploited and the subsidence rates could also be verified by a quick computation of the whole dataset. The brine extracted from 1950 to 1998 amounts to about 64 millions m^3. Considering that salt solubility in water at 15°C is 35 g/l and mean salt density is 2150 kg/m^3, it is possible to calculate that the total volume of extracted salt rock (halite) is more than 10 millions m^3.

Since the salt body covers approximately 1.5 km^2, it can be estimated that the average thickness of the exploited salt is about 6.5 m.

The mean annual subsidence rates, provided by the interpolation over the established grid throughout the exploitation period (50 years), results to exactly 6.5 m of total average subsidence. That means that the volume of dissolved and extracted salt corresponds to the volume of the bowl created by ground subsidence. The good correlation between the volume of salt exploited and the subsidence rates is also proved by the reduction in the subsidence rates during periods of lower exploitation. For instance, the halving of salt mining occurred from the year 1982 produced a subsidence rates reduction of approximately one half of the previous value. That reveals a close relationship between the amount of salt exploited and the loss of volume caused by subsidence, demonstrating that the exploitation rate is the main factor that controls the settlement process.

PART II

3. SUBSIDENCE GPS MONITORING

The measurement of ground deformation in the city of Tuzla by traditional total station surveys was no longer performed after the Balkan War. In the year 2004 a more productive and cost effective technology has been chosen by a collaboration project between the Municipality of Tuzla and the University of Bologna.

New information on modern subsidence rates were needed as a basis for urban planning and to appraise the risks related to solution mining activities.

Various papers have recently addressed the capability of GPS technique for detecting ground deformations related to subsidence (Bitelli et al., 2000; Chrzanowski et al., 2000; Chilingarian et al., 1996; Gili et al., 2000; Hofmann-Wellenhof et al., 2001; Li et al., 2004; Malet et al., 2002; Coe et al., 2003; Teatini et al., 2005).

Some preliminary investigations in the city of Tuzla by means of space geodesy and high resolution satellite image processing have been also discussed in Mancini et al. (2005) and Stecchi et al. (2006).

3.1. GLOBAL POSITIONING SYSTEM INTRODUCTION

The comprehension of the methodologies used for the subsidence monitoring of Tuzla requires to mention some theoretical concepts and terms of the GPS system. In order to be concise, basic information will be skipped.

3.1.1 Satellite Signal Structure

To calculate a point position, GPS receivers need to acquire a signal from the satellites. The official description of the GPS signal is given in the GPS Interface Control Document ICD-GPS-200 (Arinc Research Corporation, 2000).

Every satellite transmits a complex signal constituted by several components that are generated by the same electromagnetic wave (fundamental frequency $fo=10.23$ *MhZ*) (Hofmann-Wellenhof et al., 2001). The components are:

- *Carrier L1, L2*: waves with frequency respectively 154 and 120 times bigger than f_0 and wavelength of 19 and 24 cm. The use of double frequencies leads to considerable advantages because the ionospheric effect on the signal propagation can be quantified (ionosphere presents different effect in function of the frequency signal);

- *C/A, P and W codes*: these pseudorandom codes consist of a sequence with the state +1 and -1, corresponding to the binary values 0 and 1. The C/A-code (Coarse/Acquisition or Clear/Access) has the frequency *fo/10* and is repeated every millisecond. The P-code (Precision or Protected) has the frequency *fo* and is repeated every one week. The W-code (known just by qualified users) has a frequency *fo/20*, and is used to encrypt the P-code when a denying access is required. The sum of P and W codes represents the Y code.
- *Message D*: it contains information about health satellite, clocks and orbital parameters (broadcast ephemerids).

Both the L1 and L2 carrier are modulated by the P-code (more precisely by the Y-code); the C/A-code is placed on the carrier L1 in phase quadrature (i.e., 90° offset) with the P-code.

Denoting the unmodulated carriers by $Li(t)=a_i \cos(f_i t)$ and the state sequences of the P-code, the C/A-code, the W-code, and the navigation message by P(t), C/A(t), W(t), and D(t) respectively, the modulated carriers are represented by the equations (Eq. 5.7 in Hofmann-Wellenhof et al., 2001, p. 74):

$$\begin{aligned} L_1(t) &= a_1 \cdot P(t) \cdot W(t) \cdot D(t) \cdot \cos(f_1 t) + a_1 \cdot C/A(t) \cdot D(t) \cdot \sin(f_1 t) \\ L_2(t) &= a_2 \cdot P(t) \cdot W(t) \cdot D(t) \cdot \cos(f_2 t) \end{aligned} \tag{3.1}$$

During the acquisition, a GPS receiver continues to track the available satellites but it records the observables code and phase at defined intervals (called *Acquisition Epochs*).

3.1.2 Methodologies of survey: absolute, relative and differential positioning

GPS positioning could be obtained in different modalities that differ in the kind of surveys and data processing.

1. Absolute Positioning: using just one receiver that determines the absolute position in the GPS global reference system. This modality gives a low accuracy;

2. Relative positioning: using at least two receivers at the same time, it leads to the calculation of the vector (baseline) that join the points. It gives the possibilities to delete the most characteristic errors giving the best accuracy;

3. Differential positioning: similar to the absolute positioning, the position calculation is corrected from systematic errors by the information received from another station located at a known site. Differential positioning modality gives medium-high accuracy.

All the abovementioned modalities can be carried out as *static* or *kinematic* positioning. The first one can be generally used for the acquisition of points whereas the kinematic can be used to determine trajectories. A temporary loss of signal lock in static mode is not as critical as in kinematic mode.

Tuzla GPS network and surveys have been carried out by means of the static relative positioning method with carrier phase measurement that is explained with all the specific in the next paragraph.

However, to comprehend the mathematical model used for this positioning method, more general consideration about point positioning must be done.

In concept, the GPS observables are ranges (distances between satellite and receiver) which are deduced from measured time or phase differences, based on a comparison between received signal and receiver generated signal.

Unlike the terrestrial electronic distance measurements, GPS uses the "one way concept" where two clocks are used, namely one in the satellite and the other in the receiver. Thus, the ranges are biased by satellite and receiver clock errors and, consequently, they are denoted as pseudoranges (Hofmann-Wellenhof et al., 2001).

All the mathematical descriptions presented in this and next chapters (3.1.2, 3.1.3, 3.1.4) can be found in Hofmann-Wellenhof et al., 2001, cap. 8). More detailed information are available on the same textbook.

In the point positioning with code ranges, the pseudorange at an epoch *t* can be modeled, (cf. Eq. 6.2 in Hofmann-Wellenhof et al., 2001, cap. 6, p. 87) by

$$R_i^j(t) = \rho_j^i(t) + c\Delta\delta_i^j(t) \tag{3.2}$$

Here $R_i^j(t)$ is the measured code pseudorange between the observing site *i* and the satellite j, $\rho_i^j(t)$ is the geometric distance between the satellite and the observing point and c is the speed of light. The last item to be explained is $\Delta\delta_i^j(t)$.

This clock bias represents the combined clock offsets of the receiver and a satellite clocks with respect to GPS time (cf. Eq. 6.1 in Hofmann-Wellenhof et al., 2001, pag. 87).

Examining Eq. 3.2, the desired point coordinates to be determined are implicit in the distance $\rho_i^j(t)$, which can explicitly be written as

$$\rho_i^j(t) = \sqrt{(X^j(t) - X_i)^2 + (Y^j(t) - Y_i)^2 + (Z^j(t) - Z_i)^2} \tag{3.3}$$

where $X^j(t), Y^j(t), Z^j(t)$ are the components of the geocentric position vector of the satellite at epoch t, and X_i, Y_i, Z_i are the three unknown ECEF (Earth-Centered-Earth-Fixed) coordinates at the observing site.

Now, the clock bias $\Delta\delta_i^j(t)$ must be investigated in more detail. Consider a single epoch; a single position *i* is automatically implied. Each satellite contributes one unknown clock bias which can be recognized from the superscript *j* at the clock term.

Neglecting, for the present, the site *i* clock bias, the pseudorange equation for the first satellite would have four unknowns. These are the three site coordinates and one clock bias of this satellite.

Each additional satellite adds one equation with the same site coordinates but with a new satellite clock bias. Thus, there would always be more unknowns than measurements.

Even when an additional epoch is considered, new satellite clock biases must be modeled due to clock drift. Fortunately, the satellite clock information is known and transmitted via broadcast navigation message in the form of three polynomial coefficients a_o, a_1, a_2 with a reference time t_c.

Therefore, the equation

$$\delta^j(t) = a_o + a_1(t - t_c) + a_2(t - t_c)^2 \tag{3.4}$$

enables the calculation of the satellite clock bias at epoch *t*. It should be noted that the polynomial (3.4) removes a great deal of the satellite clock bias, but a small amount of error remains. The combined bias term as, $\Delta\delta_i^j(t)$ is divided into two parts by:

$$\Delta\delta_i^j(t) = \delta_i(t) - \delta^j(t) \tag{3.5}$$

where the satellite related part is known by (3.4) and the receiver related term $\delta_i(t)$ remains unknown. Substituting (3.5) into (3.2) and shifting the satellite clock bias to the left side of the equation yields:

$$R_i^j(t) + c\delta^j(t) = \rho_i^j(t) + c\delta_i(t) \tag{3.6}$$

The left side of the equation contains observed or known quantities, while the terms on the right side are unknown. Basic configurations are defined by the condition that the number of observations must be equal or greater than the number of unknowns. This condition is sufficient but does not necessarily give a solution. The number of observations is $n_j \cdot n_t$ where n_j denotes the number of satellites and n_t the number of epochs.

For static point positioning, the three coordinates of the observing site and the receiver clock bias for each observation epoch are unknown. Thus, the number of unknowns is $3 + n_t$. The basic configuration is defined by:

$$n_j \cdot n_t \geq 3 + n_t \tag{3.7}$$

which yields the explicit relation

$$n_t \geq \frac{3}{n_j - 1} \tag{3.8}$$

The minimum number of satellites to get a solution is $n_j = 2$ leading to $n_t \geq 3$ observation epochs. For $n_j = 4$, the solution $n_t \geq 1$ is obtained. This solution rejects the instantaneous positioning capability of GPS, where the four unknowns at any epoch are solved if at least four satellites can be tracked.

The basic configurations must be considered from a theoretical point of view. For example, the solution $n_j = 2$, $n_t \geq 3$ for static point positioning means that simultaneous observations of two satellites over three epochs would theoretically suffice. In practice, however, this situation would yield unacceptable results or the computation would fail because of an ill-conditioned system of observation equations unless the epochs were widely spaced (e.g., hours).

A solution is also possible if observations of three epochs for two satellites are made, followed by three additional epochs (e.g., seconds apart) for two other satellites.

Such an application will be rare but is imaginable under special circumstances (e.g., in urban areas).

Pseudoranges can also be obtained from carrier phase measurements. The mathematical model for these measurements is given by:

$$\Phi_i^j(t)=\frac{1}{\lambda}\rho_i^j(t)+N_i^j+f^j\Delta\delta_i^j(t) \tag{3.10}$$

where $\Phi_i^j(t)$ is the measured carrier phase expressed in cycles, λ is the wavelenght, and $\delta_i^j(t)$ is the same as for the code range model. The time independent phase ambiguity N_i^j is an integer number and, therefore, often called integer ambiguity or integer unknown or simply ambiguity.

The term f^j denotes the frequency of the satellite signal, and $\Delta\delta_i^j(t)$ is the combined receiver and satellite clock bias. Substituting Eq. (3.5) into Eq. (3.10) and shifting the satellite clock bias, known from Eq. (3.4), to the left side of the equation yields:

$$\Phi_i^j(t)+f^j\delta^j(t)=\frac{1}{\lambda}\rho_i^j(t)+N_i^j+f^j\delta_i(t) \tag{3.11}$$

Using the same notations as before, the number of observations is again $n_j \cdot n_t$. The number of unknowns, however, is increased by the number n_j because of the ambiguities. For static point positioning, the number of unknowns is composed of 3 coordinates of the observing station, n_j unknown ambiguities, and n_t unknown receiver clock biases.

The model in the form (3.11) comprises a rank deficiency of 1; this means that one of the unknown parameters may (and must) be arbitrarily chosen.

Supposing that a receiver clock bias at one epoch is chosen, then, instead of n_t unknown receiver clock biases, only n_t-1 clock biases remain. Therefore, the basic configuration for static point positioning without rank deficiency is defined by the relation :

$$n_j \cdot n_t \geq 3+n_j+(n_t-1) \tag{3.12}$$

which yields explicitly the required number of epochs as:

$$n_t \geq \frac{n_j + 2}{n_j - 1} \tag{3.13}$$

The minimum number of satellites to get a solution is $n_j = 2$ leading to $n_t \geq 4$ observation epochs. Another integer solution pair is $n_j = 4$, $n_t \geq 2$.

3.1.3 Main GPS positioning errors

The position of a point on the Earth is determined measuring the distance between satellite and receiver; the satellite position at every time is considered known by means of the ephemeris. Therefore, is clear that accuracy of positioning is influenced by a series of errors that strongly affect the absolute positioning, but that can be eliminated by relative or differential positioning.

Satellite orbits and clocks errors

Real time surveys use broadcast ephemeris transmitted by satellites, but usually these could be inexact; these errors can strongly affect the absolute positioning. Data post processing normally implements the use of Precise Ephemeris, routinely provided by the IGS (International GPS Service for Geodynamics).

Data are available on the Web after 2 days (rapid solution) or two weeks (final solution) (Web site: http://igscb.jpl.nasa.gov or http://igs.bkg.bund.de).

Clocks satellite errors also heavily influence the absolute positioning, but can be eliminated by the Single-differences technique in the relative positioning.

Signal propagation errors

When signal crosses the atmosphere is influenced by refraction phenomena especially in the ionosphere and troposphere. Ionosphere is a dispersive medium and the propagation delay depends on the signal frequency.

Using a double frequency (L_1 e L_2) receivers is possible to evaluate a ionosphere model and to avoid refraction delays (Hofmann-Wellenhof et al., 2001). Inospheric effects induce in the final solution a distortion quantifiable with one scale factor. The contemporary use of the two frequency permits to evaluate a ionospheric model that corrects the observables. The effect is in inverse proportion with the satellite elevation, because the higher the elevation, the shortest is the path through ionosphere.

Tropospheric effect is a limiting factor of the precision, especially for the height. Obviously the longest is the baseline the biggest is the effect, which is also affected by the satellite elevation.

Furthermore the tropospheric delay doesn't depend from the signal wavelenght, so double frequency receivers cannot do anything. Several models have been defined with results that have improved in final positioning, even at high latitude were numeric parameter have to be modelled at global scale.

Another disturb in the signal propagation is due to the reflection phenomena near the antenna receiver (multipath). Signals that reach the antenna could have been reflected by particular surfaces such as glasses, mirrors, rock faces and that could introduce a data noise. It's very important to take into account this factor when it is necessary to establish a new GPS station. The new generation of geodetic antennas can minimize the multipath effects.

Ambiguities and cycle slip

As said before, the signal is mainly represented by an electromagnetic wave; along the path between the satellite and the receiver, the signal completes a number of cycles N that is unknown by the receiver and is called "phase ambiguity".

If a receiver is tracking a satellite, after several minutes of recording, it can solve the ambiguities N that will be constant for the rest of the survey, but if the receiver loses the satellite even for few seconds, the ambiguity value has to be recalculated (cycle Slip).

Other errors

The GPS system is influenced by other errors related to the characteristics of the receiver such as frequency oscillator instability, different delay in acquisition channels, antenna phase centre variations.

Also the user has an important role during the installation of the receiver on benchmarks, levelling the tripod bubbles, measuring the antenna height, etc.

3.1.4 Static Relative positioning

Static relative positioning is the most common method used to create geodetic and topographic networks and to determine ground deformations relative to infrastructures, subsidence and slides (Bitelli et al., 2000; Gili et al., 2000; Hofmann-Wellenhof et al., 2001; Malet et al., 2002; Coe et al. 2003; Teatini et al., 2005).

In order to limit or delete the most of the errors affecting the satellite positioning (clocks error, ionosphere refraction effects, etc.), is necessary to combine the contemporary signal observations of different receivers (Hofmann-Wellenhof et al., 2001).

The objective of relative positioning is to determine the coordinates of an unknown point with respect to a known point which, for most applications, is stationary. In other words, relative positioning aims at the determination of the vector, which is often called the baseline vector or simply baseline, between the two points (Fig 3.1). Let A denotes the known reference point, B the unknown point, and $\underline{b}_{AB}$ the baseline vector. Introducing the corresponding position vectors $\underline{X}_A, \underline{X}_B$, the relation:

$$\underline{X}_B = \underline{X}_A + \underline{b}_{AB} \tag{3.14}$$

may be formulated, and the components of the baseline vector $\underline{b}_{AB}$ are:

$$\underline{b}_{AB} = \begin{bmatrix} X_B - X_A \\ Y_B - Y_A \\ Z_B - Z_A \end{bmatrix} = \begin{bmatrix} \Delta X_{AB} \\ \Delta Y_{AB} \\ \Delta Z_{AB} \end{bmatrix} \tag{3.15}$$

The coordinates of the reference point must be given in the ITRF00 system and are usually approximated by a code range solution.

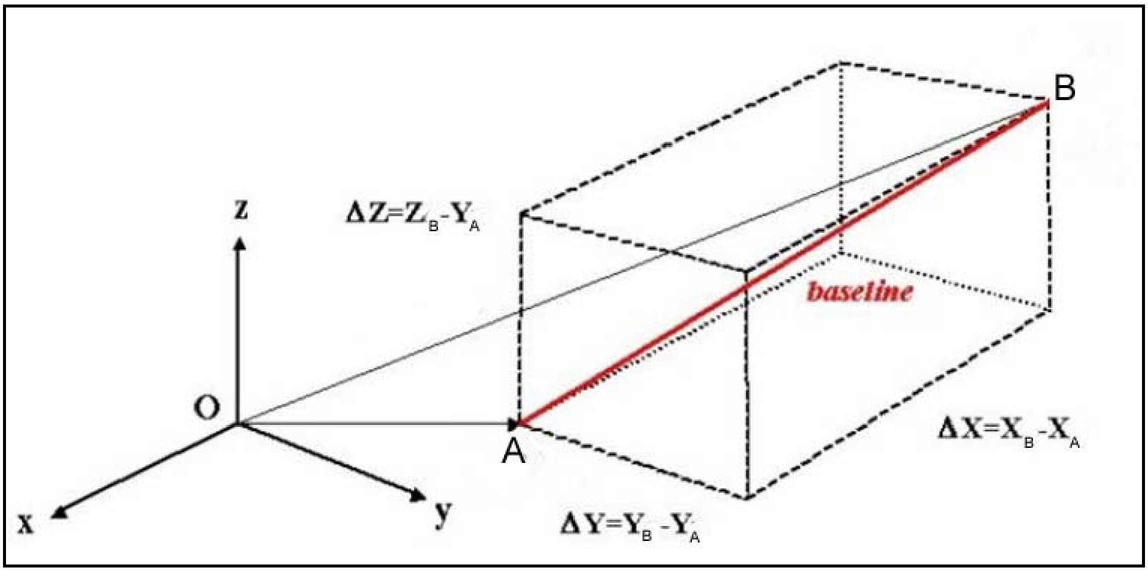

Fig. 3.1: The baseline AB oriented in the XYZ reference system

Relative positioning can be performed with code ranges (cf. Eq. 3.6), or with phase ranges (cf. Eq. 3.11).

Subsequently, only phase ranges are explicitly considered. Relative positioning requires simultaneous observations at both the reference and the unknown point. This means that the observation time tags for the two points must be the same. Assuming such simultaneous observations at the two points A and B to satellites j and k, linear combinations of phase observations can be formed leading to single-differences (SD), double-differences (DD) and triple-differences (TD).

Differencing can basically be accomplished in three different ways: across receivers, across satellites, across time.

SD corresponds to across-receiver difference, DD corresponds to across-receiver and across satellite difference, TD corresponds to across-receiver, across-satellites and across-time difference.

Most postprocessing software uses these three different techniques, so their basic mathematical modelling is shown in the following sections.

Single-differences

Two points and one satellite are involved (Fig.3.2).

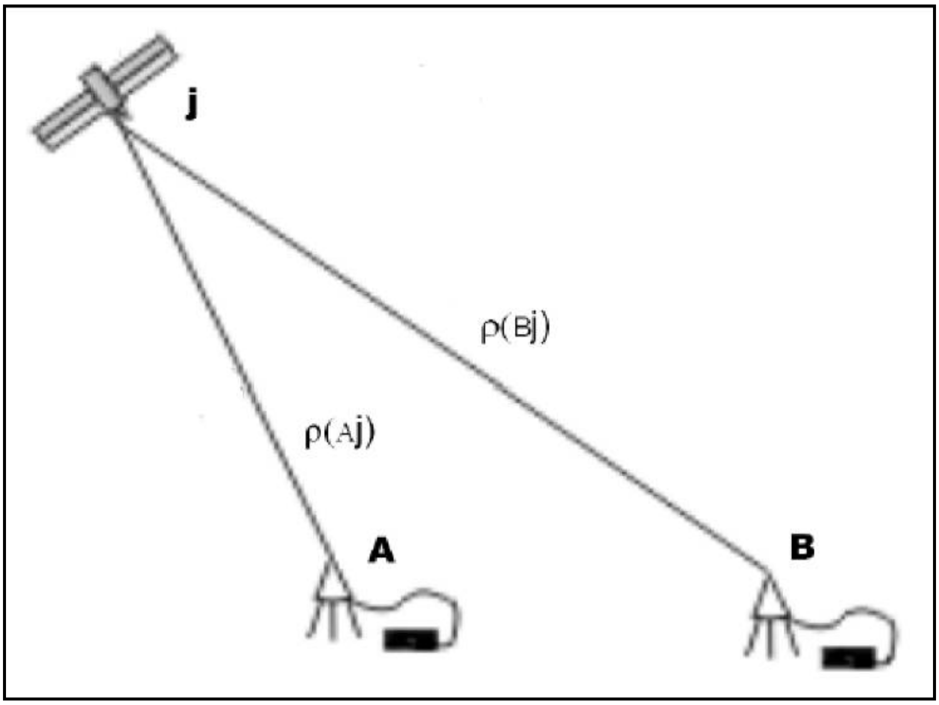

Fig. 3.2: Single-differences - Contemporary observations of one satellites by two receivers

Denoting the points by A and B and the satellite by *j* and using Eq. (3.11), the phase equations for the two points are:

$$\begin{aligned} \Phi_A^j(t) + f^j \delta^j(t) &= \frac{1}{\lambda}\rho_A^j(t) + N_A^j + f^j \delta_A(t) \\ \Phi_B^j(t) + f^j \delta^j(t) &= \frac{1}{\lambda}\rho_B^j(t) + N_B^j + f^j \delta_B(t) \end{aligned} \tag{3.16}$$

and the difference of the two equations is:

$$\Phi_B^j(t) - \Phi_A^j(t) = \frac{1}{\lambda}\left[\rho_B^j(t) - \rho_A^j(t)\right] + N_B^j - N_A^j + f^j\left[\delta_B(t) - \delta_A(t)\right] \tag{3.17}$$

Equation (3.17) is referred as the single-difference equation. This equation stresses one aspect of the solution for the unknowns on the right side.

A system of such equations would lead to a rank deficiency even in the case of an arbitrarily large redundancy. This means that the design matrix of the adjustment has linearly dependent columns and a rank deficiency exists.

Therefore, the relative quantities are introduced:

$$\begin{aligned} N_{AB}^{j} &= N_{B}^{j} - N \\ \delta_{AB}(t) &= \delta_{B}(t) - \delta_{A}(t)_{A}^{j} \end{aligned} \tag{3.18}$$

Using additionally the shorthand notations:

$$\begin{aligned} \Phi_{AB}^{j}(t) &= \Phi_{B}^{j}(t) - \Phi_{A}^{j}(t) \\ \rho_{AB}^{j}(t) &= \rho_{B}^{j}(t) - \rho_{A}^{j}(t) \end{aligned} \tag{3.19}$$

and substituting (3.18) and (3.19) into (3.17) results:

$$\Phi_{AB}^{j}(t) = \frac{1}{\lambda}\rho_{AB}^{j}(t) + N_{AB}^{j} + f^{j}\delta_{AB}(t) \tag{3.20}$$

which is the final form of the single-difference equation. Note that the satellite clock bias has canceled, compared to the phase equation (3.11).

Double-differences

Assuming the two points A, B, and the two satellites *j, k* (fig. 3.3), two single-differences according to Eq. (3.20) may be formed:

$$\begin{aligned} \Phi_{AB}^{j}(t) &= \frac{1}{\lambda}\rho_{AB}^{j}(t) + N_{AB}^{j} + f^{j}\delta_{AB}(t) \\ \Phi_{AB}^{k}(t) &= \frac{1}{\lambda}\rho_{AB}^{k}(t) + N_{AB}^{k} + f^{k}\delta_{AB}(t) \end{aligned} \tag{3.21}$$

To obtain a double-difference, these single-differences are subtracted. Assuming equal frequencies $f^{j} = f^{k}$ for the satellite signals, the result is:

$$\Phi_{AB}^{k}(t) - \Phi_{AB}^{j}(t) = \frac{1}{\lambda}\left[\rho_{AB}^{k}(t) - \rho_{AB}^{j}(t)\right] + N_{AB}^{k} - N_{AB}^{j} \tag{3.22}$$

Using shorthand notations for the satellites *j* and *k* analogously to (3.19), the final form of the double-difference equation is:

$$\Phi_{AB}^{jk}(t)=\frac{1}{\lambda}\rho_{AB}^{jk}(t)+N_{AB}^{jk} \tag{3.23}$$

The canceling effect of the receiver clock biases is the reason why double-differences are preferably used. This cancellation resulted from the assumptions of simultaneous observations and equal frequencies of the satellite signals.

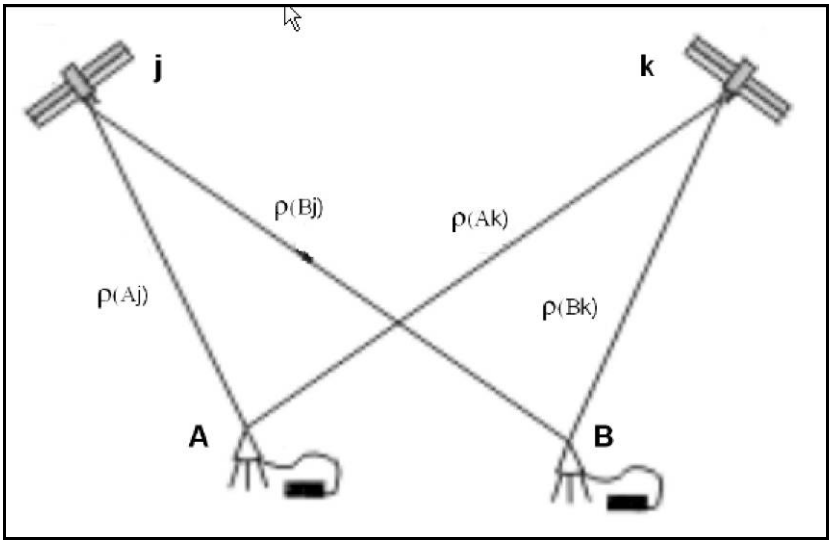

Fig. 3.3: Double-differences - Contemporary observations of two satellites by two receivers

Triple-differences

So far only one epoch *t* has been considered. To eliminate the time independent ambiguities, Remondi (1984) has suggested differencing double-differences between two epochs. Denoting the two epochs by t_1 and $t2$, then:

$$\begin{aligned}\Phi_{AB}^{jk}(t_1)&=\frac{1}{\lambda}\rho_{AB}^{jk}(t_1)+N_{AB}^{jk}\\ \Phi_{AB}^{jk}(t_2)&=\frac{1}{\lambda}\rho_{AB}^{jk}(t_2)+N_{AB}^{jk}\end{aligned} \tag{3.24}$$

are the two double-differences, and:

$$\Phi_{AB}^{jk}(t_2)-\Phi_{AB}^{jk}(t_1)=\frac{1}{\lambda}\left[\rho_{AB}^{jk}(t_2)-\rho_{AB}^{jk}(t_1)\right] \tag{3.25}$$

is the triple-difference which may be written in the simplified form:

$$\Phi_{AB}^{jk}(t_{12})=\frac{1}{\lambda}\rho_{AB}^{jk}(t_{12}) \tag{3.26}$$

The advantage of triple-differences is the canceling effect for the ambiguities and, thus, the immunity from changes in the ambiguities. Such changes are called *cycle slips* and are treated in more detail in Sect. 9.1.2 of Hofmann-Wellenhof et al. 2001, pp. 205-212).

In a static survey of a single baseline vector between points A and B, the two receivers must stay stationary during the entire observation session. The single, double, and triple-differencing are investigated with respect to the number of observation equations and unknowns. It is assumed that the two sites A and B are able to observe the same satellites at the same epochs. The practical problem of satellite blockage is not considered here. The number of epochs is again denoted by n_t , and n_j denotes the number of satellites.

The undifferenced phase, as shown in Eq. 3.11 (where the satellite clock is assumed to be known), is not included here, because there would be no connection (no common unknown) between point A and point B. The two data sets could be solved separately, which would be equivalent to point positioning.

A single-difference may be expressed for each satellite and for each epoch.

The number of measurements is, therefore, $n_j\ n_{t.}$ The number of unknowns is written below the corresponding terms of the single-difference equation:

$$\begin{aligned}&\Phi_{AB}^{j}(t)=\frac{1}{\lambda}\rho_{AB}^{j}(t)+N_{AB}^{j}+f^{j}\delta_{AB}(t)\\&n_j\cdot n_t\geq 3+n_j+(n_t-1)\end{aligned} \tag{3.26}$$

From above, the relation may be derived:

$$n_t \geq \frac{n_j + 2}{n_j - 1} \tag{3.27}$$

Although this equation is equivalent to Eq. 3.13, it is useful to repeat the minimum requirements for a solution. A single satellite does not provide a solution because the denominator of (3.27) becomes zero. With two satellites, there results $n_t \geq 4$ and for the normal case of four satellites, $n_t \geq 2$ is obtained.

For double-differences, the relationship of measurements and unknowns is achieved using the same logic. Note that for one double-difference two satellites are necessary. For n_j satellites, therefore, $n_j - 1$ double-differences are obtained at each epoch so that the total number of double-differences is $(n_j - 1)\, n_t$. The number of unknowns is written below the corresponding terms of the double-difference equation, cf. Eq. (3.24):

$$\begin{gathered} \Phi_{AB}^{jk}(t) = \frac{1}{\lambda} \rho_{AB}^{jk}(t) + N_{AB}^{jk} \\ (n_j - 1) n_t \geq 3 + (n_j - 1) \end{gathered} \tag{3.28}$$

From above, the relation

$$n_t \geq \frac{n_j + 2}{n_j - 1} \tag{3.29}$$

is obtained, which is identical with Eq. (3.27) and, therefore, the basic configurations are again given by the pairs $n_j = 2,\ n_t \geq 4$ and $n_j = 4,\ n_t \geq 2$.

To avoid linearly dependent equations when forming double-differences, a reference satellite is used, while the measurements of the other satellites are differenced.

For example, take the case where measurements are made to the satellites 6, 9, 11, 12, and 6 is used as reference satellite. Then, at each epoch the following double-differences can be formed: (9-6), (11-6), and (12-6). Other double-differences are linear combinations and, thus, linearly dependent. For instance, the double-difference (11-9) can be formed by subtracting (11-6) and (9-6).

The triple-difference model includes only the three unknown point coordinates. For a single triple-difference, two epochs are necessary. Consequently, in the case of n_t, epochs, $n_t - 1$ linearly independent epoch combinations are possible. Thus, are the resulting equations.

$$\Phi_{AB}^{jk}(t_{12}) = \frac{1}{\lambda}\rho_{AB}^{jk}(t_{12})$$
$$(n_j - 1)(n_t - 1) \geq 3 \tag{3.30}$$

From above, is obtained the relation:

$$n_t \geq \frac{n_j + 2}{n_j - 1} \tag{3.31}$$

This equation is identical to Eq. (3.27) and, hence, the basic configurations are again given by the pairs $n_j = 2,\ n_t \geq 4$ and $n_j = 4,\ n_t \geq 2.$

This completes the discussion on static relative positioning. As shown, each of the mathematical models, single-difference, double-difference and triple- difference may be used.

At present, the GPS data processing models of the most adopted packages use the DD equations as observation to be solved in the normal equations. It has been demonstrated that the TDs have a level of correlations between parameters that is might potentially corrupt the final parameters estimations.

3.1.5. Data post-processing

The relative static positioning requires the data post processing that allows the minimization or elimination of the main problems and errors, such as systematic effects modelling, ambiguities resolution, clocks errors, elevation mask.

The classical procedure can be summarized in four main steps:

1. *Data import* - Rinex (Receiver INdependent Exchange format)or receiver dependent format;
2. *Data management* – Reference system, antenna type and height, eventual known coordinates fixed points;
3. *Baselines processing* – Accuracy evaluation based on statistical model, eventual data correction. As said, most of the post-processing software uses the Single, Double and Triple-differences techniques to calculate the baselines, the last basically for cycle slip detection. The level of accuracy provided by such data processing in the network analysis could be verified by the dimension of the semi-axis of the error ellipses;

4. *Network adjustment* – Final results of a baseline vector computation are the coordinate differences in the ECEF system. The coordinates of a point are then determined by combining these coordinate differences in a network adjustment procedure where one (or more) point is kept fixed. Generally a minimally constrained least squares adjustment that analyzes the overall network is computed. If the network can be tied only to one ground position (permanent station), it can freely move during adjustment. Any measurement blunders on your part are therefore more likely to be isolated and detected. On the other hand, once a network is constrained to two or more control stations, it is forced to accommodate itself, plus the previously established control. This introduces errors from prior surveys into your network, making it more difficult to locate any errors in your field work. Ideally, a constrained adjustment should not be performed until all obvious outliers have been detected and removed or remeasured (Hofmann-Wellenhof et al., 2001).

3.1.6. Reference Systems

GPS system provides the measured point coordinates in the same reference system used to describe the satellite orbits. *Space fixed* system (inertial) and *Earth fixed* system (respect to the earth system) have to be distinguished in GPS applications. Both the two systems are geocentric and constituted by a Cartesian tern XYZ which has the origin in the earth mass center and Z axis coincident with the earth rotation axis.

In the Space fixed system Y axis is oriented in the vernal point direction (the intersection between the equatorial plane and ecliptic plane), while in the Earth fixed it is identified by the intersection between the equatorial plane and the Greenwich meridian. X axis completes the dextrorotatory tern.

The GPS networks are definitively installed on the earth surface. The satellite ephemeris defined in a space system have to be therefore connected to the earth fixed system as initial stage of data processing.

The two Conventional Terrestrial Reference System are:

1. *World Geodetic System 1984* (WGS84). From the year 1987, this geocentric system has been determinate using more than 1500 terrestrial sites. It represents the standard reference system for most of GPS users, and it is associated to an ellipsoid with the same parameters. It has to be mentioned that WGS84 system has been update by DMA *(Defense Mapping Agency, USA)* using more precise measures.

2. *ITRF* (*International Terrestrial Reference Frame*) has been determinate by IERS *(International Earth Rotation Service)* using spatial geodesy measures in more than 180 terrestrial sites (*SLR, Satellite Laser Ranging; VLBI, Very Long Baseline Interferometry*), and considering as well the tectonics effect. Besides ITRF is more precise than WSG84, and it is generally used for GPS data post processing.

The transformation between the two systems is obtained by a rotation with 7 parameters:

$$X_{WGS} = T + sRX_{TRF} \qquad \text{(Eq. 3.32)}$$

Where T is the translation vector, *s* the scale factor and R the matrix rotation.

The insertion of GPS surveys is actually favoured by the IGS network (*International GPS Service for Geodynamics*) which expresses the coordinate of fixed points and satellite orbits to the ITRF. That permitted the creation of successive ITRF and the current is ITRF2005.

The framing of GPS measures in a ITRF can be performed in different ways:

1. Using precise ephemerids provided by IGS. This is possible if there are not other constrains in the network elaboration, and the station coordinates can be converted between the different ITRF using the available parameters:
2. Using ephemerids of a generic systems then constraining the adjustment of one or more points in any ITRF. All the linked points will be also expressed in the same ITRF.

Broadcast ephemerids are in the WGS84 system and precise ephemerid are in the ITRF.

3.2 TUZLA GPS NETWORK

A GPS network based on relative static methodology has been established around Tuzla subsidence area. Six reference benchmarks have been installed on stable sites around the sinking area and a denser network composed of about 50 points has been installed within the collapsing area.

The two networks will be analyzed separately. Data have been post-processed by means of Geogenius^{TM} (Spectra Precision Terrasat), one of the most suitable software processing short sessions of measurements performed in a restricted area.

Official reports of results can be found in ANNEX 1 .

3.2.1 Reference network

Field activities for the reference network have been carried out in the 2004, 2005 and 2007.

During data post-processing the network has been framed in the International Terrestrial Reference Frame (ITRF, epoch 2000); in particular permanent stations of Medicina (MEDI - I), Matera (MATE - I), Sofia (SOFI - BG) and Penc (PENC - H), have been linked to the Tuzla network., using precise ephemerids provided by IGS.

The ITRF is characterized by movements related to tectonics and Earth axis oscillation; single movement of permanent stations are calculated by IGS and available at the Web site: http://itrf.ensg.ign.fr/ITRF_solutions/2000/sol.php

Using on-line interactively HTDP (Horizontal Time Dependent Positioning) software, (Web site: http://geodesy.noaa.gov/cgi-bin/HTDP/htdp.prl?f1=1&f2=1), local displacements of the permanent stations have been calculated in relation to surveys times, and inserted as constrains in the processing software. In this way the network has been connected to the ITRF of the permanent stations coordinates.

Long baselines (300-600 Km) have been processed in L*c* mode that reduces the Ionosphere effects, while short baselines have been processed in L_1, that gives better results for 5-10 Km long baselines.

Level of accuracy of single-baselines processing can be verified by the dimension of the semi-axis of the error ellipses which are lower than 5 mm (fig. 3.4).

The specific time period chosen for an observation is called session; the static surveys for Tuzla reference network have been carried out with sessions of 2-3 hours on average, and few sessions of 7-8 hours.

At the time of the first field campaign (2004) permanent stations were not available so close as preferred in the baseline processing. Thus the abovementioned stations have been used (MEDI, MATE, SOFI, PENC) even if far from Tuzla area (300-600 Km). For this instance the accuracy of long baselines is not as good as short baselines.

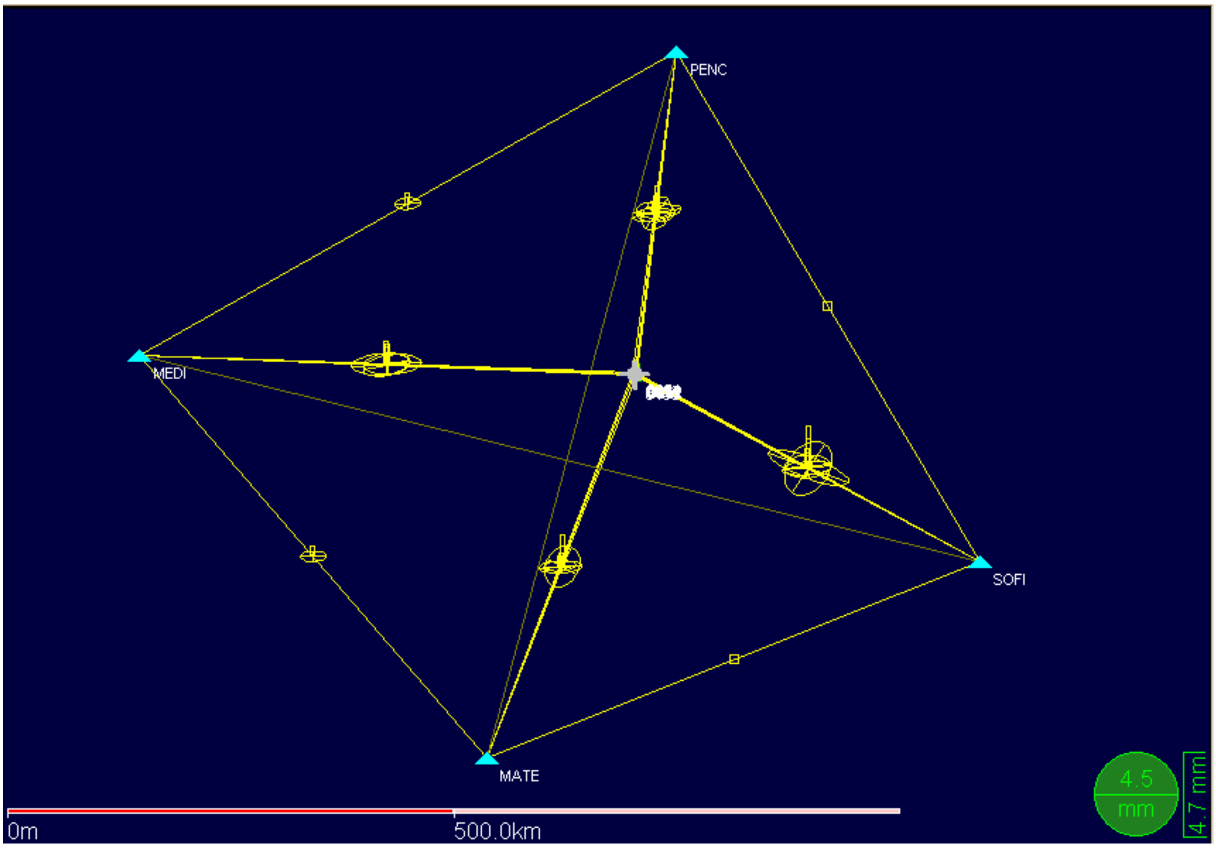

Fig. 3.4: Capture of a particular stage in the processing of 2004 GPS data in static mode, where baseline and errors are computed. Errors, shown as 3-dimensional ellipses at 95% level of significance, are generally lower than 5 mm.

The reference network has been constrained by a least squares adjustment; that spreads the final error ellipses of the reference points surrounding the densification network. The mentioned accuracies are valid for all the three performed campaigns, and have to be intended as references in an area were GPS geodetic activities were not carried out before.

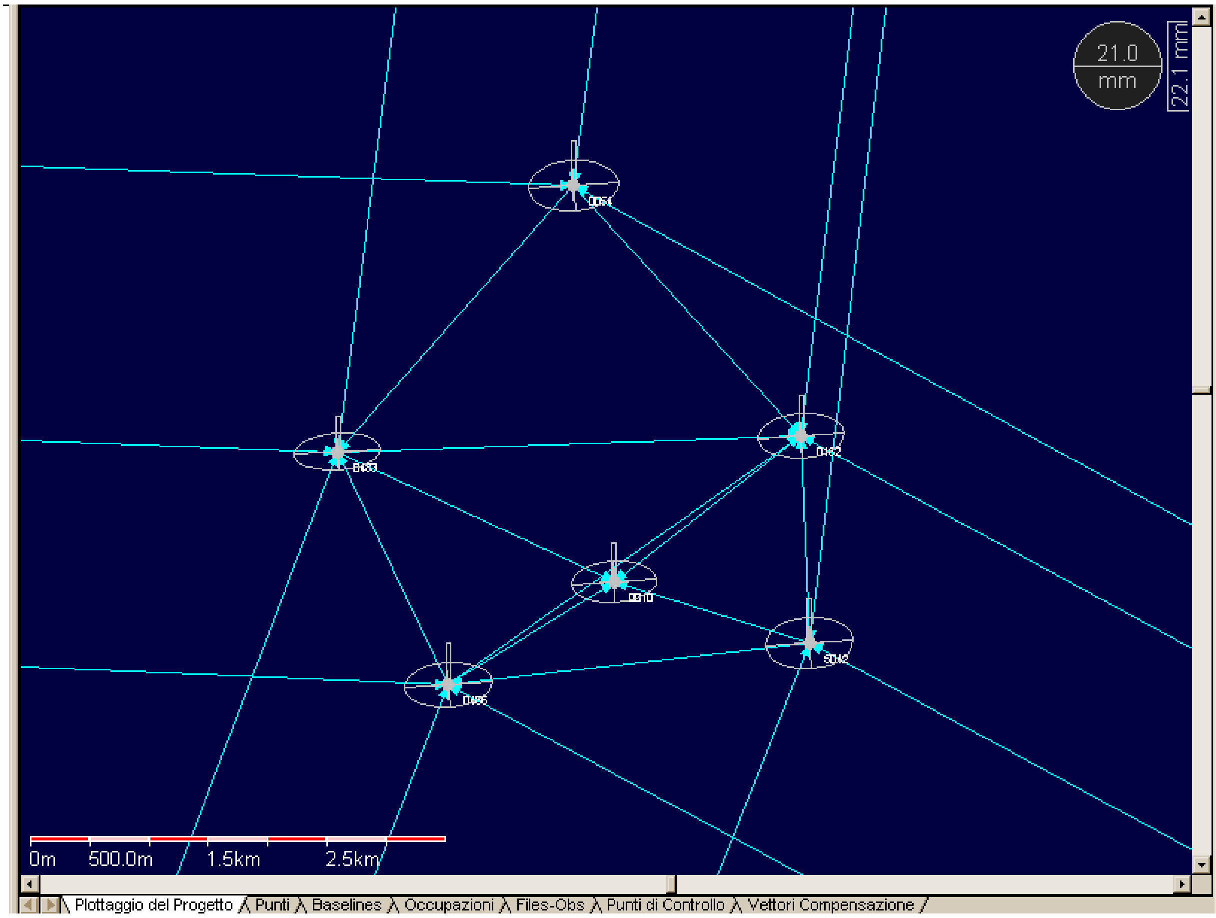

Fig. 3.5: Particular of the adjustment procedure of 2004 GPS network. Errors, shown as 3-dimensional ellipses at 95% level of significance, are lower than 2 cm.

The quality of data processing, in terms of data management, inserted values and procedures adopted, has been verified by a cross-comparison between the results of the different campaigns, previously uptated to the same reference epoch.

It was therefore possible to validate the stability of the reference stations with respect to the external Reference Frame, avoiding underestimation of the sinking rate due to possible, but not detected subsidence of the reference stations.

3.2.2 Subsidence densification network

The surveys of the network inclusive of the sinking points have been carried out in the 2004, 2005, 2006 and 2007, by means of static and fast-static GPS survey methodologies with sessions not shorter than 30 minutes.

Single-baselines of all campaigns have been processed in L_1 mode. The level of accuracy can be verified by the dimension of the semi-axis error ellipses (fig. 3.6), which are lower than 1 cm.

The sinking network has been constrained by a least squares adjustment, where the six points of the reference network have been fixed to a set of coordinates values verified during the repetitions of the abovementioned measurements.

The results of adjustment (fig. 3.7) reveals for the most of the points an accuracy of 3-5 mm, while for some bad positioned points the accuracy decreases to 2-3 cm. Very bad solution points have been rejected.

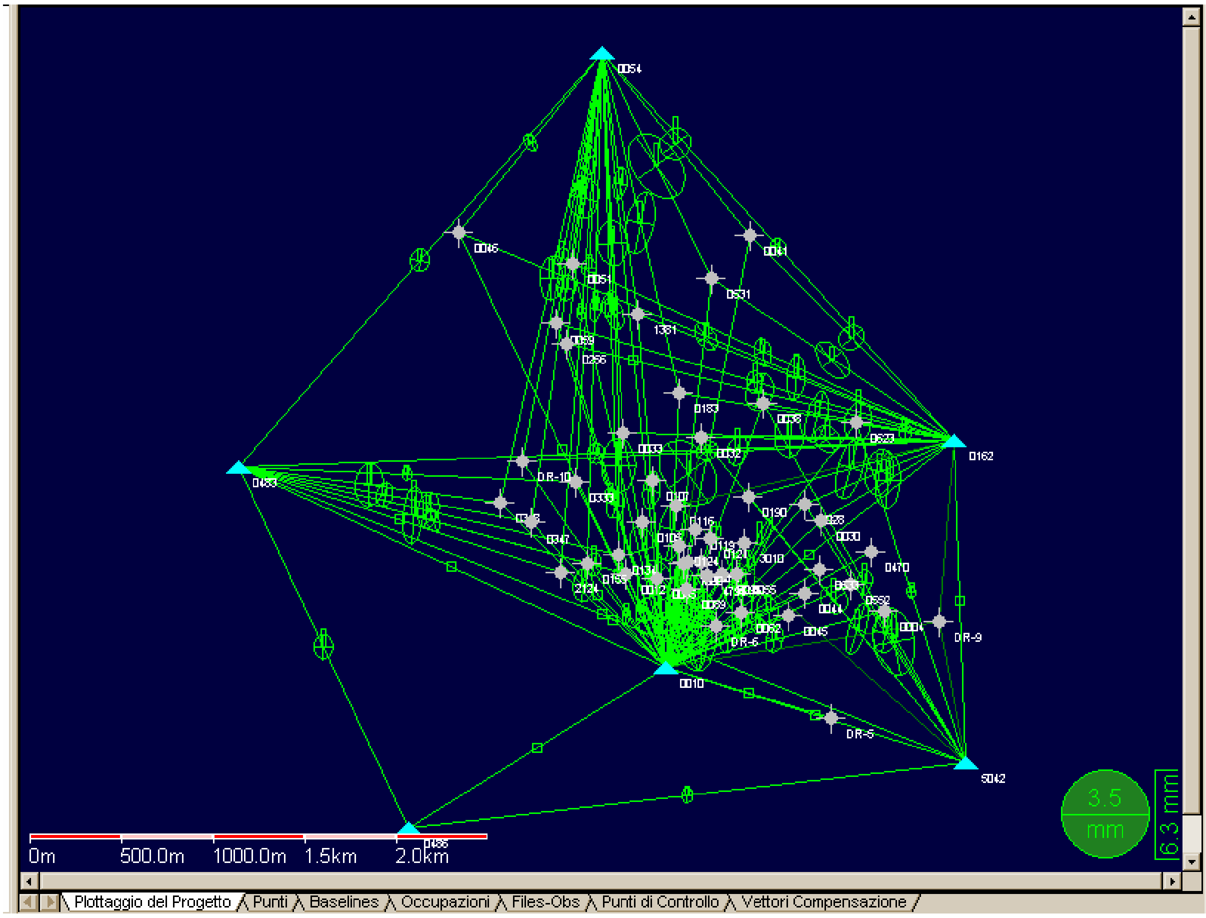

Fig. 3.6: Capture of a particular stage in the processing of 2005 GPS network in static mode, where baseline and errors are computed. Errors, shown as 3-dimensional ellipses at 95% level of significance, are lower than 7 mm.

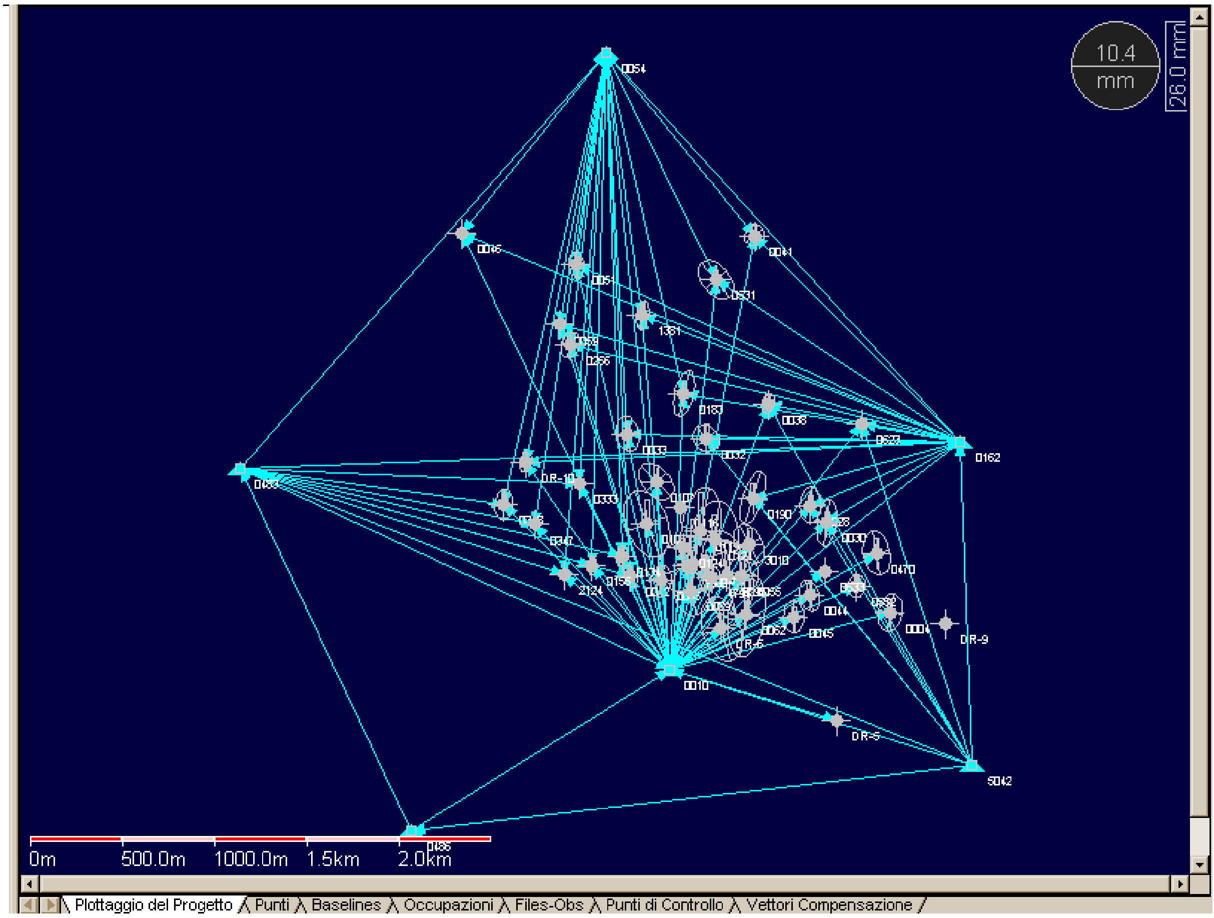

Fig. 3.7: Capture of adjustment procedure of 2005 GPS network. Errors, shown as 3-dimensional ellipses at 95% level of significance, are lower than 1 cm for the most of points. Note that error ellipses for the reference points are equals to zero.

3.4. CURRENT SUBSIDENCE RATES

Once it was established that the reference network is free from elevation changes or local deformations, we compared the solutions provided by the processing of data collected during the 2004, 2005, 2006 and 2007 GPS campaigns.

The comparison between the first two campaigns (fig. 3.8), shows that a considerable part of the town was still subjected to 10-20 cm/y subsidence rates; as consequence of previous collapses this area is currently not very urbanized. Part of the historical centre is subjected to 2-5 cm/y rates which can still cause stability problems to buildings and infrastructures, but they are not so devastating as in previous periods.

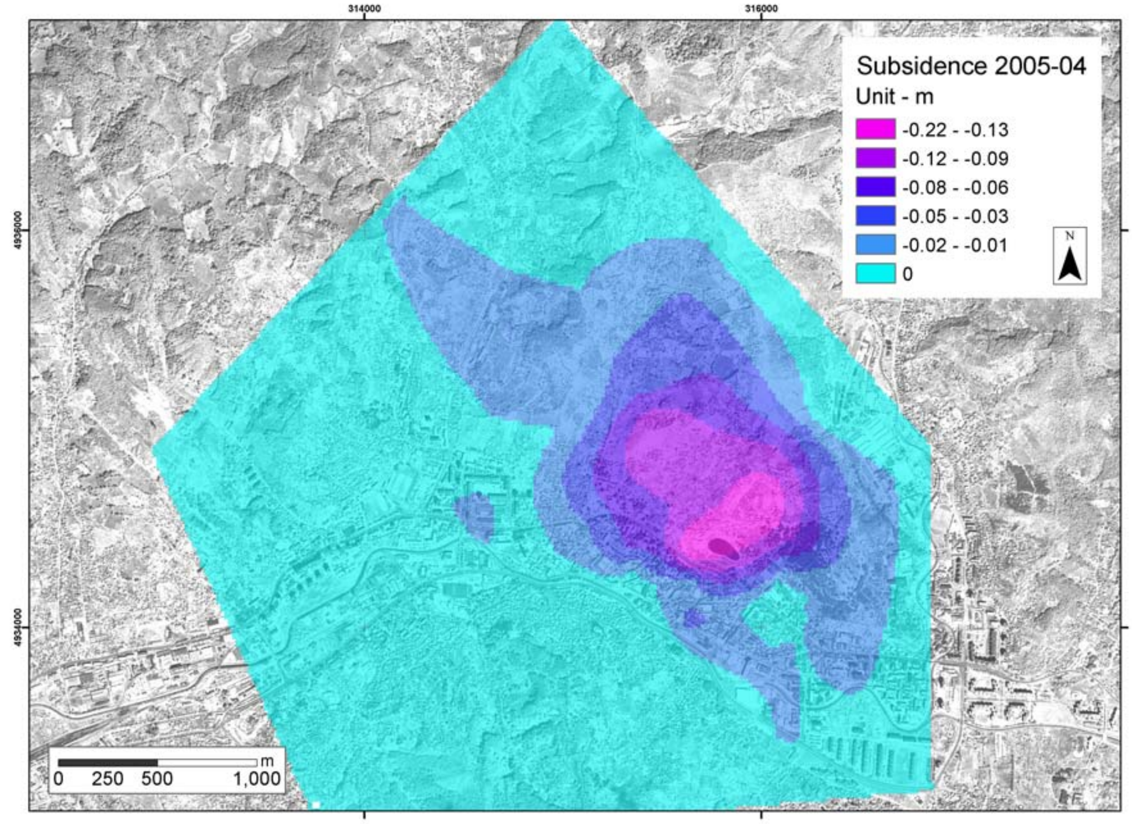

Fig. 3.8: Subsidence rates 2004-2005 obtained by the comparison of the first two campaigns

The second comparison (2006-2005, fig. 3.9) depicts an evident decrease in the subsidence rates: the most collapsing area (in proximity of Pinga lake) was the only one where sinking reached 20 cm/y, while the rest of the town was affected by 5 cm/y. The historical town was subsiding of 1-2 cm/y.

The last comparison reveals that subsidence is presently turning to the end everywhere, except for the Pinga area where sinking rates are decreasing but still around 10 cm/y (fig. 3.10).

The latest subsidence rates derived from GPS observations is consistent with the decreasing trend that started from 1984 as a consequence of the reduction in salt mining activities (cf. Fig. 2.10).

In particular the GPS-derived subsidence rates for the 2004-2005 interval, should match the 730000 m^3 of brine exploited per year by 10-12 wells still active in that period. The relationship illustrated in figure 2.9 appears to be valid until today. In fact, a 30% of reduction in salt withdrawal with respect to the ’90 values (an annual average rate of 1 millions m^3 can be selected as reference), corresponds to a decrease of sinking rates at the same level.

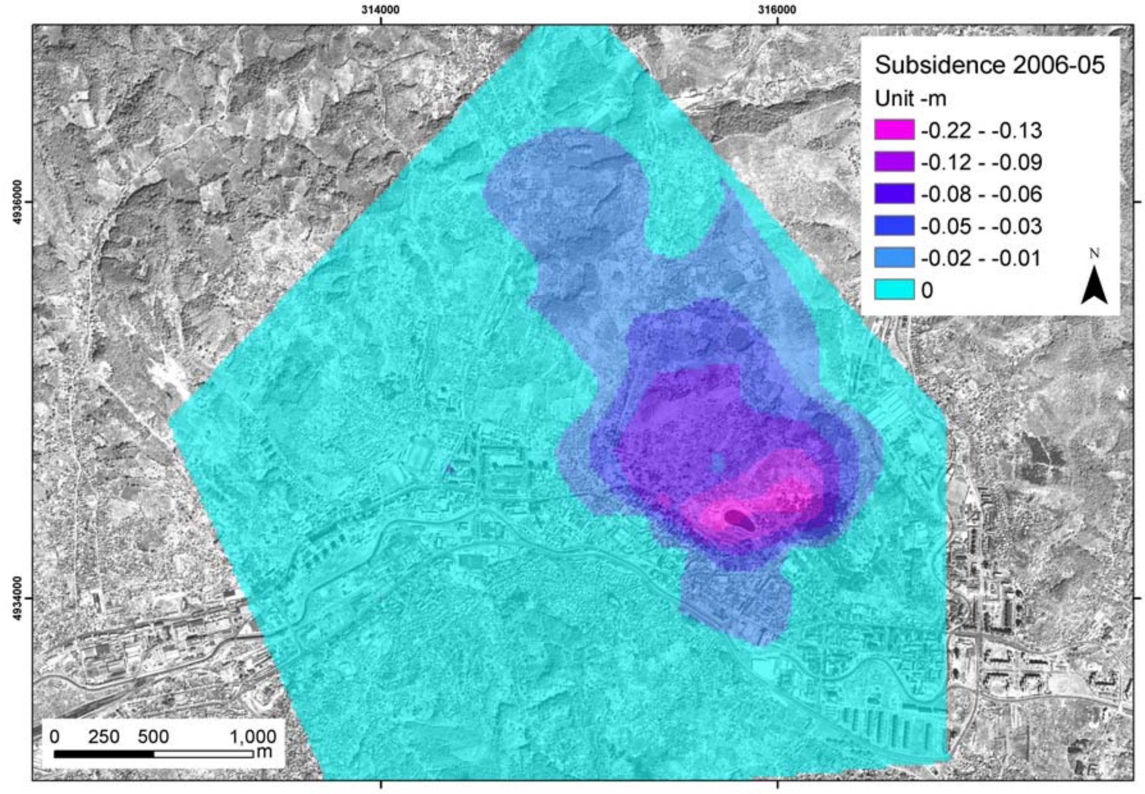

Fig. 3.9: Subsidence rates 2005-2006 obtained by the comparison of the second and third campaign.

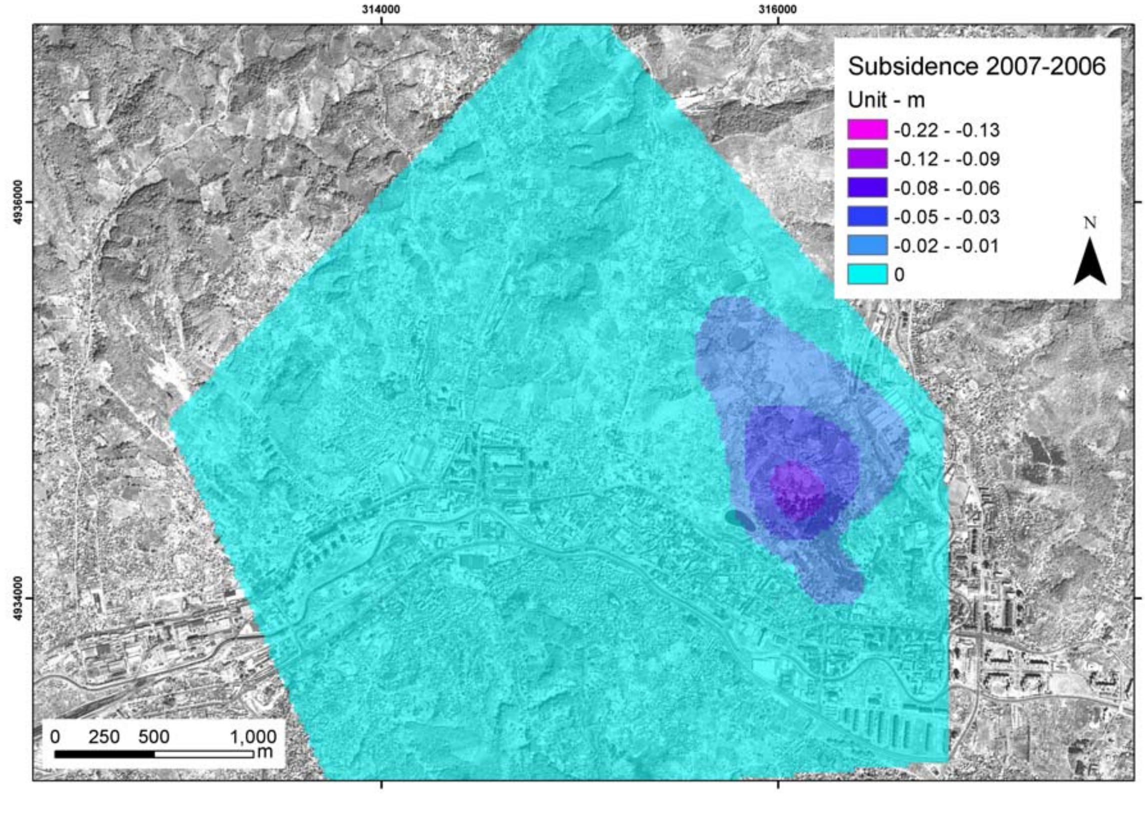

Fig. 3.10: Subsidence rates 2006-2007 obtained by the comparison of the last two campaigns.

4. CURVATURE ANALYSIS AND FRACTURES IDENTIFICATION

4.1. TUZLA FRACTURES SYSTEM

As proved in laboratory with several tests and models by Hongxing and Martin (1998), salt exploitation also induced the formation of many faults and fractures.

The deformation and the evolution of the collapsing phenomenon induced in Tuzla are strictly connected with salt dissolution. Several techniques were used to investigate the underground composition and the location of the deformed structures, such as borehole drillings, geo-electric resistivity surveys and seismic refraction surveys, but they didn’t lead to any significant results to the comprehension of the collapse phenomena (Basić personal communication 2005).

Boreholes were, in fact, too widely spaced to reconstruct the three dimensions of the subsurface structures, seismic surveys strongly resented of the existence of a low velocity layer (salt rock) below higher seismic velocity rocks as are the deposits just under the city of Tuzla (Basić personal communication 2005). Finally, resistivity surveys are limited in depth and strongly influenced by the saline groundwater movement (Telford 1967).

The comprehension of fracturing in fold and dome structures is critical in the planning and management of a wide range of practical engineering and scientific activities.

Fractures are known to have a strict relation with the charge, seal and trapping potential of hydrocarbons and fluids reservoirs. Determining the style, orientation, and density of fractures in folded or domed strata in the subsurface, is a critical step in any successful aquifer/reservoir management.

Several studies have been proposed in geoscience literature to describe geological surfaces and to predict the distribution of deformation in folded or domed strata.

Various authors suggest the use of “surface attributes”, such as the surface curvature and rate of dip change, in the attempt to determine the location and “amount” of deformation in folded subsurface strata (Bergbauer and Pollard, 2003-a)

4.2 CURVATURE ANALYSIS

Given the inadequacy of most of the geophysical methods, in this chapter is presented a novel approach to identify the localization of faults and fractures in the subsurface and the delineation of high risk zones in Tuzla area. We propose and present the effectiveness of curvature analysis (Lisle, 1994) applied to cumulative sinking data envelope surfaces, as a replacement or an aid to classical topography and geophysics.

Curvature analysis allows to identify areas on a surface where the deformation is more or less localized and, therefore, helps in the identification of zones that are potentially faulted and fractured (Fischer and Wilkerson, 2000; Roberts, 2001; Masaferro et al. 2003).

The study of surface curvature is routinely used in oil exploration of fractured reservoirs to identify areas with the largest potential for fracture porosity and permeability (Lisle, 1994; Hennings et al., 2000). Calibration studies using boreholes, seismic and curvature analysis data show that curvature is particularly effective in identifying faulted areas (Nelson 2003).

In particular, conclusions concerning the state of strain in folded surface can be drawn on the basis of variation of Gaussian curvature across the concerned structure. The parts of the structure with highest fracture densities broadly match those areas with highest absolute values of Gaussian curvature (Nelson 2003).

Recent studies (Allwardt et al., 2007) also confirms the correlation between high curvature values and fracture set orientations by coupling fracture mapping (GPS) with structural mapping.

Curvature has been calculated using two different methods:

- Directional two-dimensional curvature calculating the second derivative of surface displacement along a defined direction:
- Analytical calculation of Normal and Gaussian curvature (Fischer and Wilkerson, 2000; Bergbauer and Pollard, 2003; Pearce et al., 2006).

4.2.1 Concept of curvature

Curvature is the amount by which a geometric object deviates from being flat, but this is defined in different ways depending on the context. Extrinsic curvature is defined for objects embedded in another space (usually an Euclidean space) and it relates to the radius of curvature of circles that touch the object, while intrinsic curvature is defined and calculated by means of a differential geometry.

For a plane curve C, the curvature at a given point P has a magnitude equal to the reciprocal of the radius of an osculating circle (a circle that "kisses" or closely touches the curve at the given point), and is a vector pointing in the direction of that circle's center (Fig. 4.1). The smaller is the radius *r* of the osculating circle, the larger is the magnitude of the curvature *(1/r)*; hence where a curve is "nearly straight", the curvature will be close to zero, and where the curve undergoes a tight turn, the curvature will be large in magnitude.

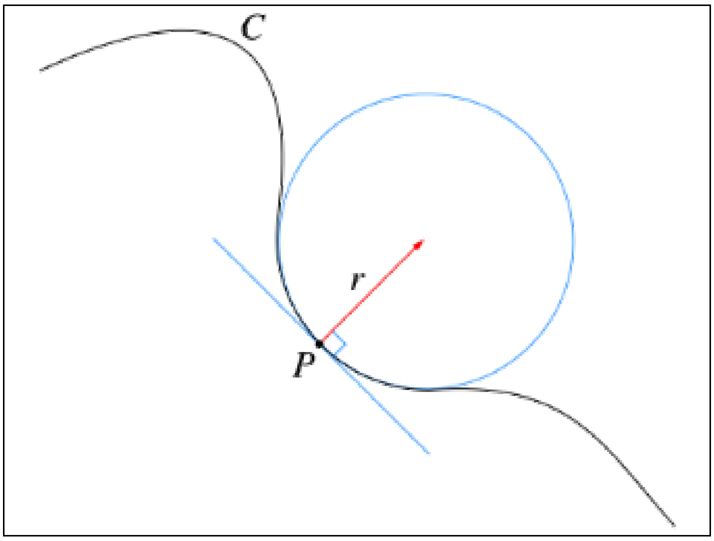

Fig.4.1: The osculating circle closely touches the curve at a given point P

From an analytical three-dimensional point of view, consider the intersection of the surface with a plane containing the normal vector and one of the tangent vectors at a particular point; this intersection is a plane curve and has a curvature .

The curvature of a surface is defined in terms of the curvature of an arbitrary line that lies in that surface. The curvature of a line equals the change of the tangent vector (t) as one proceeds a differential distance (*ds*) along the line (Fig. 4.2-a). The arc length *ds* equals the absolute value of the difference (*d*r) of position vectors r and r’ defining the two endpoints of the arc. As one proceeds over a curved surface along a meandering path, the direction of the path with respect to a global coordinate changes for two reasons: first because the surface is curved, and second because the path meanders over the surface. Thus the curvature vector (k) is composed of two vectors, one normal to the surface, and the second lying in the tangent plane to the surface (Bergbauer and Pollard, 2003a):

$$dt / ds = k = k_n + k_g \tag{4.1}$$

where k_n is the *normal curvature vector*, and k_g is the *geodesic (or tangent) curvature vector* (Fig. 4.2-b). The normal curvature vector points toward the center of curvature of the surface, and its magnitude is the *normal surface curvature* (Bergbauer and Pollard, 2003a).

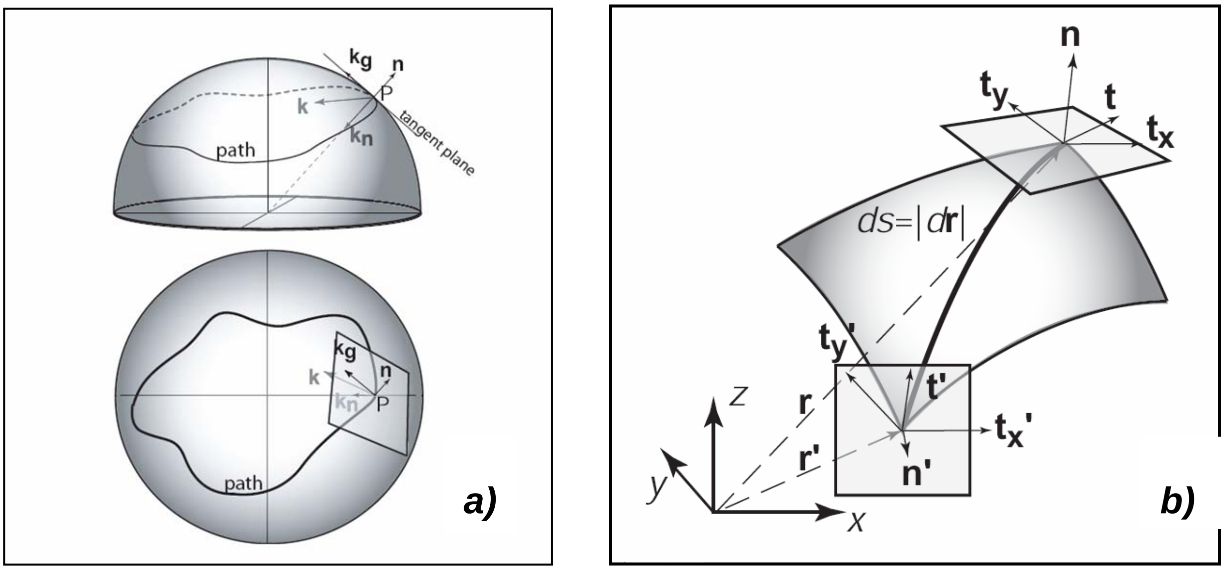

Figure 4.2. The curvature of an arbitrary surface is defined as the rate of change of tangent vector t as one moves along the arc of a curve ds on the surface (modified after Bergbauer and Pollard, 2003a).

On a sphere, for example, the value of the normal curvature remains constant and the vector points to the center of the sphere from any point on the surface, independent of the path taken over the surface. The geodesic curvature vector, in contrast, lies in the tangent plane to the surface at point P and is a measure of the meandering of the path across the surface. The magnitude of the geodesic curvature is not necessarily constant and will change depending on the path taken across the sphere.

Focusing only on evaluating the normal curvature vector is therefore sufficient to describe the curvature of the surface itself. Normal surface curvature is calculated along paths across the surface.

For surfaces other than a sphere, the normal curvature depends on the direction of the path in which it is calculated.

For the cylindrical fold shown in Fig. 4.3, the normal surface curvature is zero along the fold axis and maximum in the direction perpendicular to the fold axis.

The magnitude of the normal surface curvature at point P depends on the direction of the path (gray lines) through point P. At every point P on the surface there are two orthogonal directions (path 1 and path 3) in which the normal curvature magnitudes assume extreme values: the principal curvature directions.

Normal curvature magnitudes calculated in any other direction at P will fall between these two principal values. There are an infinite number of possible directions that cross a point P on a surface, and there are an infinite number of normal surface curvatures one could evaluate.

The magnitude of the calculated normal curvature vector at this point will vary depending on the path taken through the point P, but the direction of this vector is always parallel to the unit normal vector *n* on the surface at P. There are two orthogonal directions at P in which the normal curvature takes on extreme values, called the *principal surface curvatures*. All other curvature values at P fall between these two extreme values (Bergbauer and Pollard, 2003a).

Normal surface curvatures can be calculated in any direction, for example along strike or dip of the surface (Roberts, 2001).

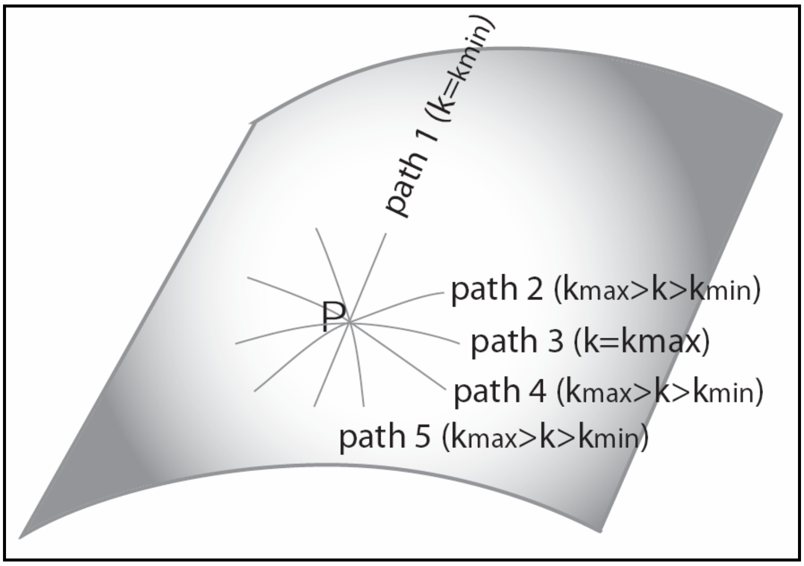

Fig. 4.3: The magnitude of the normal surface curvature at point P depends on the direction of the path (gray lines) through point P (modified after Bergbauer and Pollard, 2003a).

In previous studies curvature has been calculated on topography (GPS and Total Station), isobaths of structural surfaces or seismic data time surfaces (Lisle, 1994; Hennings et al., 2000).

These surfaces need a prior data filtering, in order to clear the surface from micro-scale variations that add noise and are not relevant for fractures and faults identification (Bergbauer and Pollard, 2003; Allwardt et al., 2007).

4.2 2 Data source surface

The subsidence affecting Tuzla is accommodated by both areal collapse and strain localization as shown by the surface faults and fractures (Fig. 4.4) that have been detected at the surface in the areas of largest deformation.

The surface envelope of the total subsidence has therefore recorded the strain partitioning within the Tuzla city and, given its small scale smoothness, is an ideal surface on which to study curvature.

Fig. 4.4: Examples of fractures in the downtown of Tuzla related to strain localization

Curvature has been calculated on the surface obtained by gridding the sinking rates of the cumulative period 1956-2003. In this way the changes in slope are only connected with ground movements, and curvature calculation doesn't take into account the micro-scale variations of topography (Fig. 4.5).

The data source consists of about 100 points over a 1 Km^2 area; before actually calculating the curvature over the mentioned data source, several interpolation techniques have been tested, such as Inverse Distance Weighting, Regularized Spline, Ordinary Kriging, Multiquadratic Radial Basis Function, to see which one would have given the best results. As many authors already suggested (Chaplot V. et Al., 2006), we decided to use the Radial Basis Functions to interpolate the sinking surface

Fig. 4.5: The sinking surface of the period 1956-2003, used as data source to calculate curvature

4.2.4 Directional two-dimensional surface curvature computation

The directional curvature measures the change rate of the inclination angle of tangential planes on a profile line defined by the surface along a specified direction. The calculus has been carried out by means of Golden Software Surfer^{TM}, where curvature is reported as the absolute value of the rate of change and is, therefore, a positive number.

This method aims to identify possible sharp changes in slope of the subsidence envelope, that may represent the position of a fault's scarp or where a shear zones displacement has been concentrated (Fig.4.6).

Directional curvature has been calculated perpendicularly to the axis of the valley, because the direction of surface faults and the anisotropy of the deformation ellipse have the same trend.

In case of steeply dipping surfaces, approximating the normal curvature of a surface, either by the second partial derivative or by the curvature of a planar curve, leads to erroneous results. Errors in calculated curvature magnitudes exceed 50% on strata folded to dips of about 30° (Bergbauer et al, 2003). The sinking map obtained from the altimetric data shows a maximum slope of 3.5° and that guarantees the accuracy of calculated curvature magnitudes (Fig. 4.7).

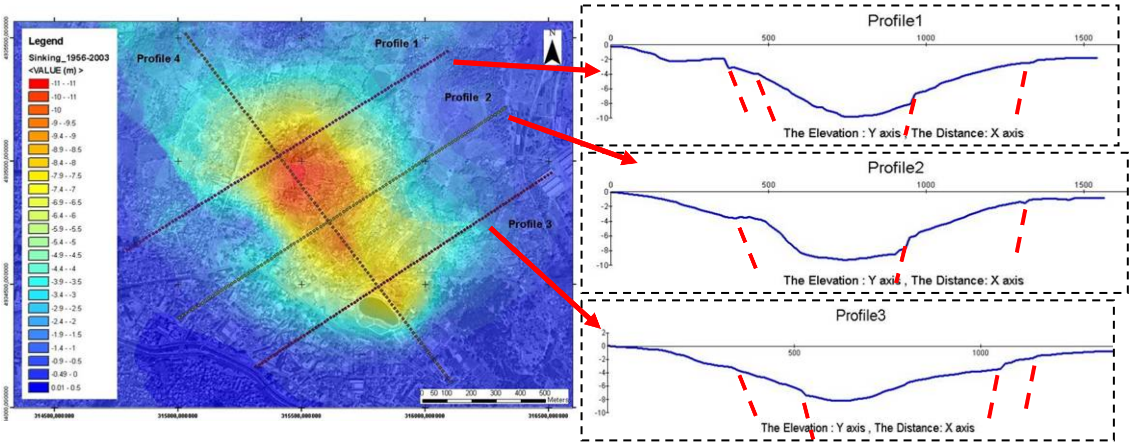

Fig. 4.6: Functioning principle of directional curvature. A sharp change in slope along one of the profiles, may represents the position of a fault's scarp or where a shear zones displacement has been concentrated. Golden software Surfer^{TM} performs infinite profiles over the subsidence surface instead of just three profiles.

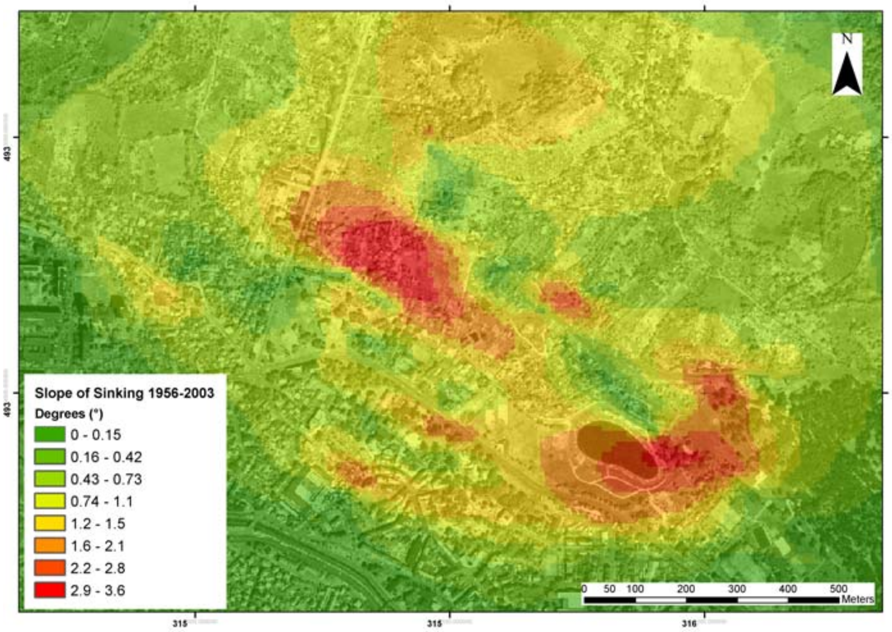

Fig. 4.7: Slope Map of the sinking surface 1956-2003. The slope value never exceeds 3.5°.

4.2.5 Analytic three-dimensional surface curvature computation

The mathematical method used for the calculation of the Gaussian and Mean curvature is the one proposed by Bergbauer and Pollard (2003a), and is based on the fundamental forms of differential geometry.

First Fundamental Form

In 3-D Euclidean space, a surface is sufficiently described by two quadratic differential equations, the so-called *First and Second Fundamental Forms*. The normal surface curvature can be calculated from these two fundamental forms.

The First Fundamental Form follows directly from the Pythagorean representation of a differential arc length *ds* on the surface (Fig. 4.8).

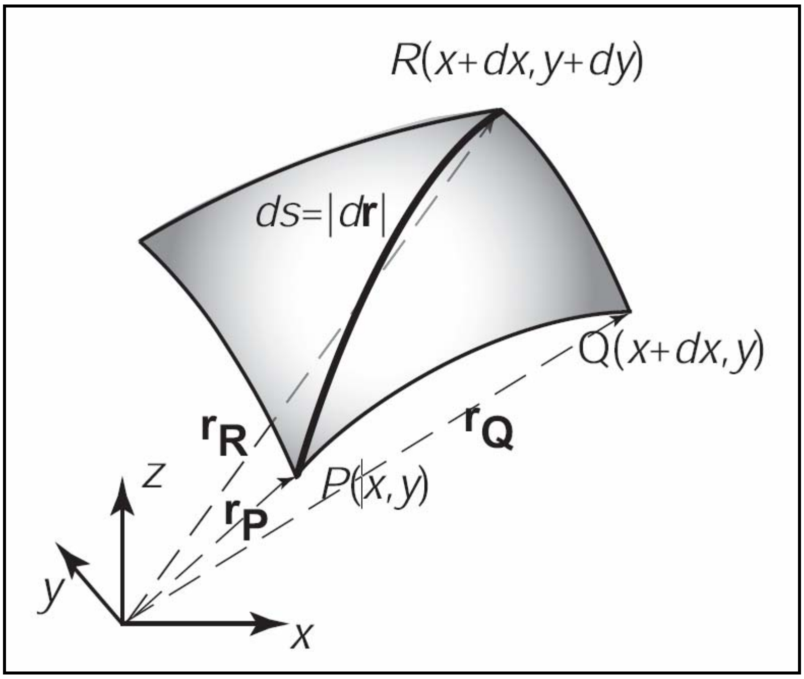

Fig. 4.8: The arc length ds *between two points P and R on a surface can be expressed in terms of the vectors* **r***P,* **r***Q and* **r***R. The First Fundamental Form follows directly from the square of the arc length.*

The arc length *ds* between the points P and R on a surface can be expressed in terms of the position vectors **r**Q, **r**P, and **r**R. The square of *ds* is related to these vectors as:

$$ds^2 = d\mathbf{r}^2 = (\mathbf{r}_{PQ} + \mathbf{r}_{QR})^2 = \mathbf{r}_{PQ} \cdot \mathbf{r}_{PQ} + 2\, \mathbf{r}_{PQ} \cdot \mathbf{r}_{QR} + \mathbf{r}_{QR} \cdot \mathbf{r}_{QR} \tag{4.2}$$

Here

$$\mathbf{r}_{PQ} = \mathbf{r}_Q - \mathbf{r}_{P,} \text{ and } \mathbf{r}_{QR=} \mathbf{r}_R - \mathbf{r}_Q$$

are the distances between points P and Q, and points Q and R, respectively, and the dot indicates the scalar product of two vectors. In vector notation, a surface can be expressed as:

$$\mathbf{r}(x,y) = x \cdot \mathbf{e}x + y \cdot \mathbf{e}\mathrm{y} + \mathrm{z(x,y)} \cdot \mathbf{e}x \tag{4.3}$$

where r is the position vector of every point on the surface, x and y are two independent parameters, $z(x,y)$ is an elevation measurement with respect to the x-y parameter plane, and $\mathbf{e}_x$, $\mathbf{e}_y$, and $\mathbf{e}_z$ are the unit vectors in the direction of the Cartesian coordinate system axes. The vectors defining ds in Eq. (4.2) can be expressed using Eq. (4.3):

$$\mathbf{r}_{PQ} = x_Q\mathbf{e}_x + y_Q\mathbf{e}_y + z_Q(x,y)\mathbf{e}_z - [x_P\mathbf{e}_x + y_P\mathbf{e}_y + z_P(x,y)\mathbf{e}_z],$$
$$\mathbf{r}_{QR} = x_R\mathbf{e}_x + y_R\mathbf{e}_y + z_R(x,y)\mathbf{e}_z - [x_Q\mathbf{e}_x + y_Q\mathbf{e}_y + z_Q(x,y)\mathbf{e}_z].$$

Using the coordinates of the points P, Q, and R as shown in Fig. 5.8, the partial derivatives (slopes of the surface) in the directions of the two parameters are (in the limit as dx and dy go to zero):

$$\frac{\partial z}{\partial x} = \frac{z_Q - z_P}{dx}, \text{ and}$$
$$\frac{\partial z}{\partial y} = \frac{z_R - z_Q}{dy}$$

Eq. (2) can now be recast as (Eq. 5-8 in Chap. 2 of Struik, 1961):

$$\mathbf{I} = ds^2 = \mathrm{d}\mathbf{r}^2 = \alpha_{xx}\, dx^2 + 2\, \alpha_{xy}\, dxdy + \alpha_{yy}\, dy^2 \tag{4.4a}$$

where

$$\alpha_{xx} = 1 + \left(\frac{\partial z}{\partial x}\right)^2, \alpha_{xy} = \left(\frac{\partial z}{\partial y}\right) \cdot \left(\frac{\partial z}{\partial y}\right), \alpha_{xx} = 1 + \left(\frac{\partial z}{\partial y}\right)^2 \tag{4.4b}$$

α_{xx}, α_{xy}, and α_{yy} are called the *metric coefficients* of the surface (Eq. 2-7 in Chap. 2 of Struik, 1961). Eq. (4.4) is called the First Fundamental Form of surfaces (I).

Since the First Fundamental Form is the square of an arc length *ds*, it is always positive. This fundamental form provides a basis for a metric representation of distances, angles, and areas on a surface. Considering that the arc length between two points on a surface is constant regardless of the coordinate system in which it is measured, the First Fundamental Form is invariant with respect to coordinate transformation.

Second Fundamental Form

The Second Fundamental Form describes the spatial rate of change of the unit normal vector **n** to a surface and the spatial rate of change of position on that surface (*d***n** · *d***r**). As shown in Fig. 4.2a, the unit normal vector **n** at a point is perpendicular to the tangent plane at this point.

The tangent plane is defined by two tangent vectors that point in the directions defined by the parameters x and y, respectively (Eq. 3-1 in Chap. 2 of Struik, 1961):

$$\mathrm{t}_{\mathrm{x}} = \frac{\partial \mathrm{r}}{\partial x} = \mathrm{e}_{\mathrm{x}} + \left(\frac{\partial z}{\partial x}\right) \cdot \mathrm{e}_{\mathrm{z}} \text{, and}$$

$$\mathrm{t}_{\mathrm{y}} = \frac{\partial \mathrm{r}}{\partial y} = \mathrm{e}_{\mathrm{y}} + \left(\frac{\partial z}{\partial y}\right) \cdot \mathrm{e}_{\mathrm{z}}$$

The unit normal vector **n** to the tangent plane is given by the cross product of these two tangent vectors divided by the magnitude of this product (Eq. 3-2 in Chap. 2 of Struik, 1961):

$$\mathrm{n} = \frac{\mathrm{t}_{\mathrm{x}} \times \mathrm{t}_{\mathrm{y}}}{\left|\mathrm{t}_{\mathrm{x}} \times \mathrm{t}_{\mathrm{y}}\right|} = \frac{\mathrm{e}_{\mathrm{z}} - \frac{\partial z}{\partial x}\mathrm{e}_{\mathrm{x}} - \frac{\partial z}{\partial y}\mathrm{e}_{\mathrm{y}}}{\sqrt{\alpha_{\mathrm{xx}}\alpha_{yy} - \alpha_{xy}^{2}}} \tag{5}$$

Using Eqs. (4.3) and (4.5), *d*n and *d*r are defined by their total derivatives:

$$d\mathrm{n} = \frac{\partial \mathrm{n}}{\partial \mathrm{x}} dx + \frac{\partial \mathrm{n}}{\partial \mathrm{y}} dy \text{, and}$$

$$d\mathrm{r} = \frac{\partial \mathrm{r}}{\partial \mathrm{x}} dx + \frac{\partial \mathrm{r}}{\partial \mathrm{y}} dy \text{,}$$

The Second Fundamental Form can be written as (Eq. 5-8 in Chap. 2 of Struik, 1961):

$$\mathrm{II} = -\,d\mathbf{n} \cdot d\mathbf{r} = \beta_{xx}dx^2 + 2\,\beta_{xy}dxdy + \beta_{yy}dy^2 \tag{4.6a}$$

where

$$\beta_{xx} = \frac{\frac{\partial^2 z}{\partial x^2}}{\sqrt{\alpha_{\mathrm{xx}}\alpha_{yy} - \alpha_{xy}^2}}, \beta_{xy} = \frac{\frac{\partial^2 z}{\partial x \partial y}}{\sqrt{\alpha_{\mathrm{xx}}\alpha_{yy} - \alpha_{xy}^2}}, \beta_{yy} = \frac{\frac{\partial^2 z}{\partial y^2}}{\sqrt{\alpha_{\mathrm{xx}}\alpha_{yy} - \alpha_{xy}^2}} \tag{4.6b}$$

are the coefficients of the Second Fundamental Form (Eq. 5-10 in Chap. 2 of Struik, 1961).

These coefficients are sometimes called the curvature coefficients, as they, in conjunction with the metric coefficients, provide information about the deviation of the surface from its tangent plane. The Second Fundamental Form is also invariant with respect to coordinate transformation.

Normal surface curvature

The magnitude of the normal curvature of a surface is calculated by dividing the two fundamental forms. From Eqs. (4) and (6) it follows (Eq. 5-6 in Chap. 2 of Struik, 1961):

$$k_n = \frac{\mathrm{II}}{\mathrm{I}} = \frac{\beta_{xx}dx^2 + 2\beta_{xy}dxdy + \beta_{yy}dy^2}{\alpha_{xx}dx^2 + 2\alpha_{xy}dxdy + \alpha_{yy}dy^2} \tag{4.7}$$

This equation shows that different normal surface curvature magnitudes k_n are calculated for different directions taken through the point of interest by varying dx and dy. k_{n} is also an invariant property of a surface.

Eq. (4.7) reduces to the standard formula for calculating the curvature at points along a curved line lying in the (x, z)-plane that can be found in most books on calculus (e.g., Stewart, 1995):

$$k_x = \frac{\frac{\partial^2 z}{\partial x^2}}{\left[1 + \left(\frac{\partial z}{\partial x}\right)^2\right]^{3/2}} \tag{4.8}$$

The one above is the form of the equation cited by Murray (1968), Ivanov (1989), Nothard et al. (1996) and Stewart and Podolski (1998), and referred as *the* curvature, but it is a very special case of the normal surface curvature.

Principal curvature directions

Relative to the arbitrarily chosen differential parameters *dx* and *dy*, two orthogonal directions can be found in the tangent plane in which the normal curvature obtains extreme values (the principal curvatures of a surface, k_1 and k_2). Dividing by dx^2, Eq. (4.7) can be recast as (Eq. 6-3 in Chap. 2 of Struik, 1961):

$$k_{n(\lambda)} = \frac{\mathrm{II}}{\mathrm{I}} = \frac{\beta_{xx} + 2\beta_{xy}\lambda + \beta_{yy}\lambda^2}{\alpha_{xx} + 2\alpha_{xy}\lambda + \alpha_{yy}\lambda^2} \tag{4.9}$$

where $\lambda = dy/dx$. The principal directions λ_1 and λ_2 (lines of curvature) are found by solving:

$$\frac{\partial k_n(\lambda)}{\partial \lambda} = 0$$

It follows that:

$$\lambda_{1,2} = -\frac{\sqrt{\frac{1}{4}(\alpha_{xx}\beta_{yy} - \alpha_{yy}\beta_{xx})^2 - (\alpha_{xy}\beta_{yy} - \alpha_{yy}\beta_{xy})(\alpha_{xx}\beta_{xy} - \alpha_{xy}\beta_{xx})}}{\alpha_{xy}\beta_{yy} - \alpha_{yy}\beta_{xy}} \tag{4.10}$$

Principal curvature magnitudes

Once the principal directions $\lambda 1$ and $\lambda 2$ are found by solving Eq. (4.10), the magnitude of the principal curvatures *k1* and *k2* can be calculated by substituting $\lambda 1$ and $\lambda 2$ into Eq. (4.9).

Gaussian curvature

The Gaussian curvature *G* (Gauss, 1827) is defined as the product of the two principal curvatures (Eq. 7-3 in Chap. 2 of Struik, 1961):

$$G = k_1 \cdot k_2 = \frac{\beta_{xx}\beta_{yy} - \beta_{xy}^2}{\alpha_{xx}\alpha_{yy} - \alpha_{xy}^2} \tag{4.11}.$$

Gaussian curvature is an important quantities useful for surface description. Surfaces can be distinguished based on a second important quantity, namely the mean curvature (M) (Roberts, 2001), but for the purpose of this study it is not strictly necessary because Gaussian curvature already identify strain localization by itself.

$$M = \frac{1}{2}(k_1 + k_2) = \frac{\alpha_{xx}\beta_{yy} + \beta_{xx}\alpha_{yy} - 2\alpha_{xy}\beta_{xy}}{2(\alpha_{xx}\alpha_{yy} - \alpha_{xy}^2)} \tag{4.12}$$

The curvature calculation in Matlab™ consists of three different scripts carried out to calculate respectively:

- the first partial derivatives;
- the second partial derivatives;
- the principal curvatures, the Gaussian and Mean curvature.

The Matlab script proposed by (Bergbauer et al 2003) can be found at ANNEX 2

4.3. RESULTS AND COMPARISONS

The first objective of this mathematical approach has been to confirm the reliability of the method in identifying areas of strain localization where faults and fractures have accommodated surface deformation.

In order to accomplish this, visible faults and fractures on the terrain have been mapped. Unfortunately, the most fractured and faulted areas correspond to where the buildings have been demolished and the ground levelled. These areas, therefore, have been deeply modified by human restoring activities and it has been difficult to find clear evidence of fractures. On the contrary, fractures and faults on the roads of the downtown centre are still evident, where old buildings are still present (Fig. 4.4).

Figure 4.9 shows the results for the curvature magnitudes obtained with Surfer™ in a direction normal to the valley's axis (30° North): high curvature values indicate possible fractured and faulted areas where strain has been localized.

A sharp change in slope of the subsidence envelope, in fact, may represents the position of a fault's scarp or where a shear zones displacement has been concentrated. Note the good correlation between mapped faults/fractures position and direction with the curvature magnitude especially in the southern part of the map where the buildings have not been completely destroyed and the ground has not been levelled.

The areas of large curvature in the north-eastern part of the town, correspond to the areas that have been mostly damaged by subsidence. In this parts, some of which are on a gentle slope, buildings have been completely destroyed and the traces of the original surface faults have been obliterated by the restoration activities.

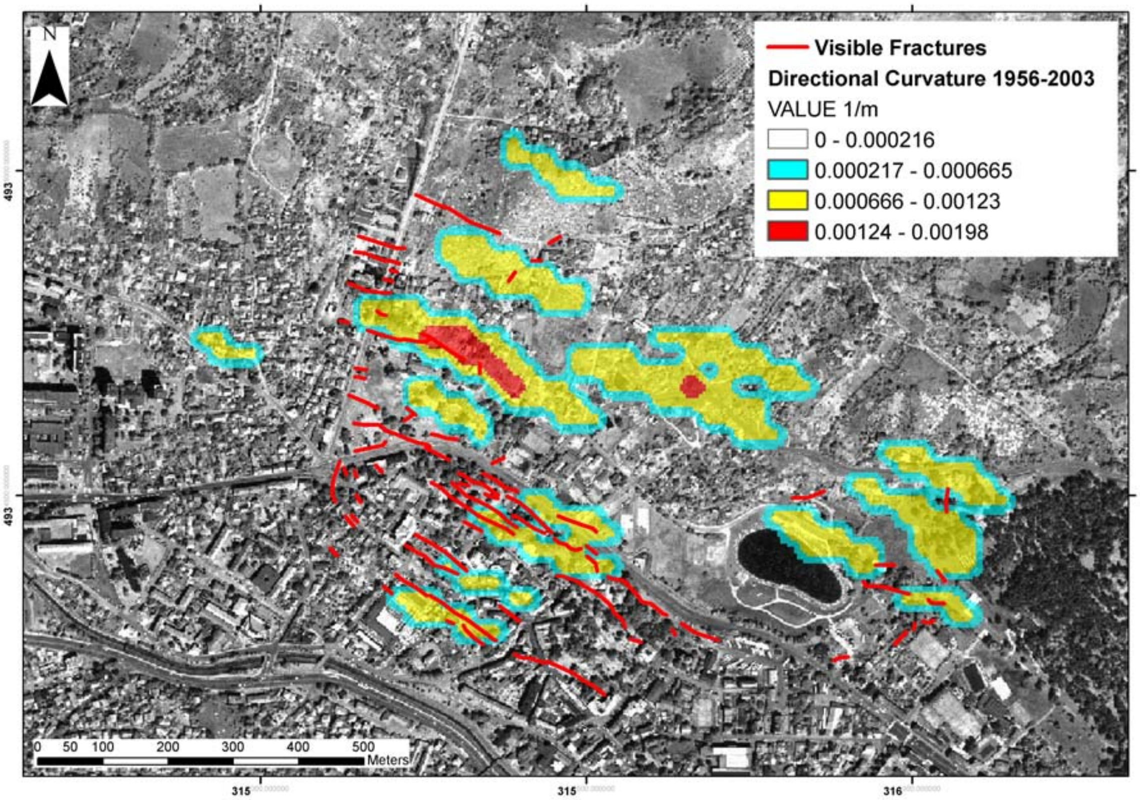

Fig. 4.9: The directional curvature map of 1956-2003 sinking data obtained by means of Golden Software Surfer.

The analytical method of Bergbauer and Pollard (2003a) gives an exact form of Gaussian curvature and it has been used as an indicator for the presence of structures that caused differential subsidence, inducing the formation of dome and sink structures in the subsidence envelope. Positive Gaussian curvature values are interpreted as indicators for "horst structures" or, more in general, for the footwall of a subsurface fault. On the other hand, negative gaussian curvature values are interpreted as “sink” or basin-like features related to “graben” structures or, more in general, to the hanging wall of normal faults. Figure 5.10 shows that gaussian curvature captures well the dome and sink structures connected to the displacement on subsurface normal faults, but does a poorer job in the correlation with surface areas of strain localization (faults and fractures).

There are more evident deformed areas in Fig. 4.9 than in Fig. 4.10, obtained with directional curvature in Surfer, even if the correspondence with surface fractures is less significant.

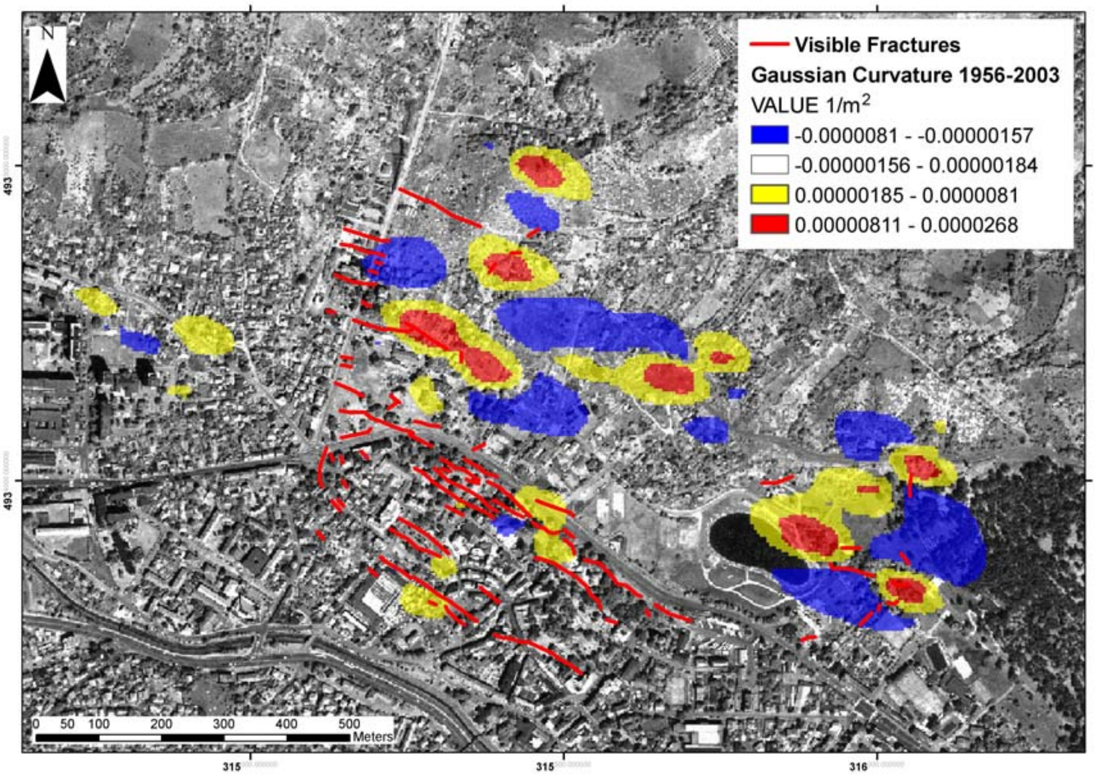

Fig. 4.10: The Gaussian Curvature map obtained by the 1956-2003 sinking data using the fundamental forms of differential geometry.

In conclusion the results of the calculation show how directional curvature is reliable for the identification of shallow fractures, while the Gaussian curvature, obtained by the analytical method, works good in the localization of horst and graben structures which are related to subsurface normal faults connected with the deformations.

5. URBAN CHANGES EVOLUTION

The wild brine pumping has caused dramatic effects on the buildings of Tuzla (damages and collapses) leading to the evacuation of parts of the town. The sequence of such urban changes has been tracked analysing historical maps of the city and recent high resolution satellite images. For this purposes, in addition to the latest available maps updated to the year 1965, a couple of high resolution satellite images have been acquired (Ikonos and QuickBird sensors). The basic characteristics of the satellite data are summarized in Table 5.1.

	IKONOS	**QUICKBIRD**
Date of collection	2000-06-09	2005-07-25
Spatial Resolution (PAN)	1 m	0.6 m
Off nadir angle	20.07°	8.3°
Level of geometric correction*	Standard geometrically corrected	LV2A
Cloud Cover	0%	0%
RPC	✓	✓
PAN	✓	✓
MS	✓	✓

Tab. 5.1: description of metadata supplied by SpaceImaging and DigitalGlobe.

The comparison between Fig. 5.1, 5.2 and 5.3, depicts the urban changes occurred from 1965 to 2005 in the area strongly affected by ground deformations. By moving to the Ikonos satellite image (2000), it is clear that the same area is almost completely free from settlements due to the collapse and demolition of buildings.

The last QuickBird imagery (2005) shows the change in land use of this area, now devoted to parks and recreational services. Unfortunately, official data regarding the loss of properties due to ground deformations are very poor.

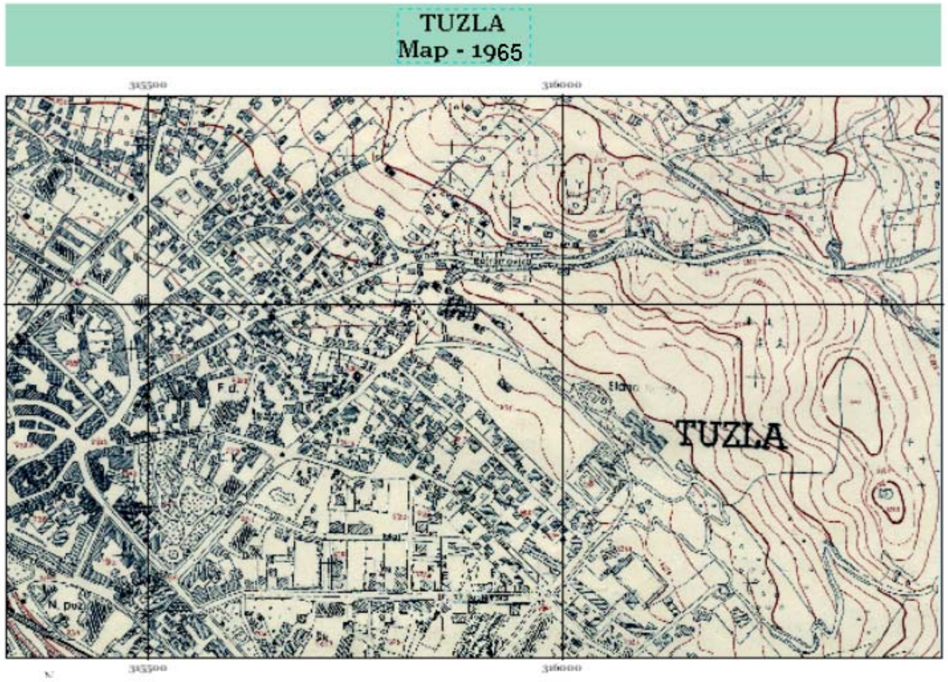

Fig. 5.1: The topographic map of the year 1965 represents the first documentation in terms of buildings location and amount, and it ahs been as basis for the urban changes analysis.

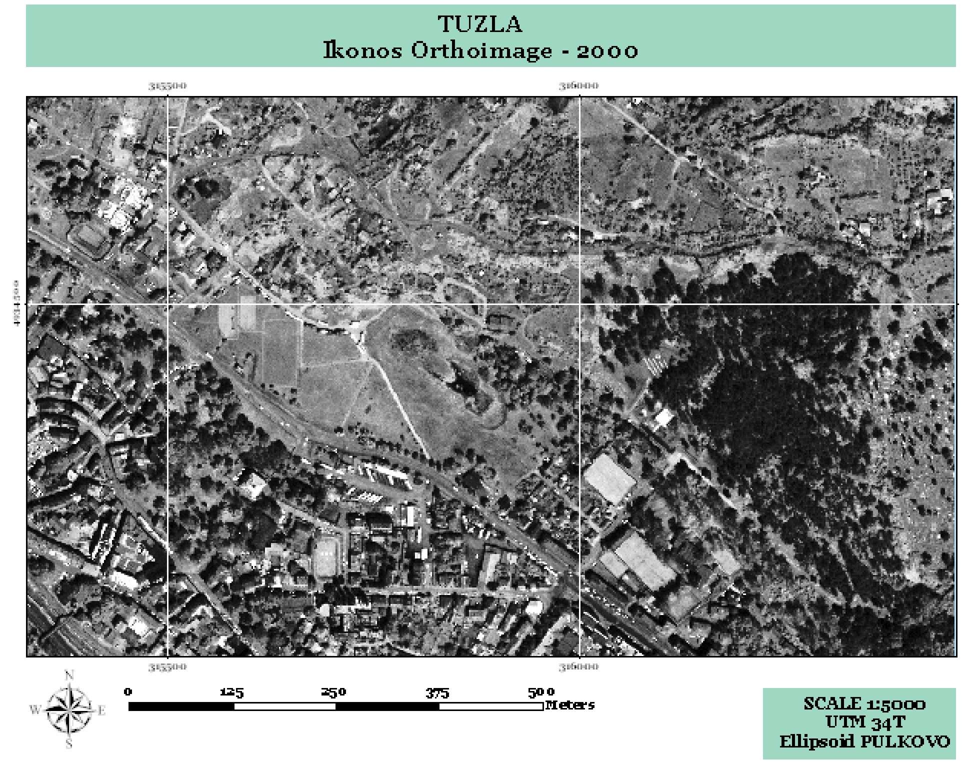

Fig. 5.2: Ikonos orthoimage of the year 2000. Note the large abandoned area up north to the center town

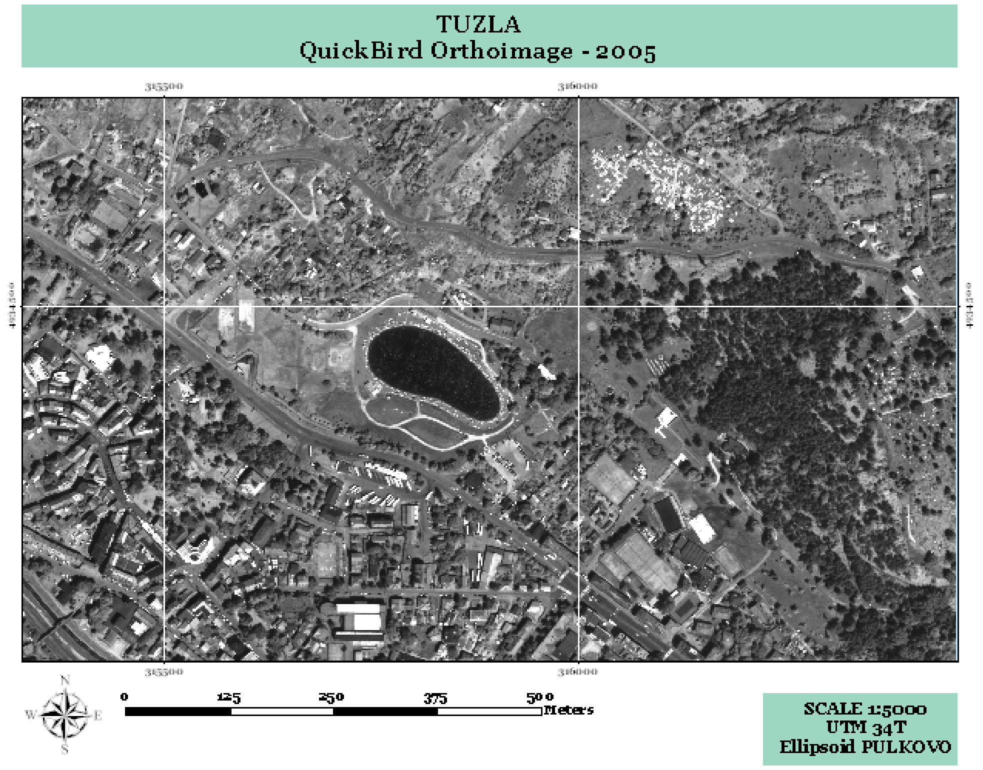

Fig. 5.3: Quickbird orthoimage of the year 2005. The abandoned marshy area of the center has been converted into a recreational salt lake.

Tatić (1979) supposed that 2,350 apartments were demolished and 10,000 people lost their home "..during the last period..", with a likely further loss of 1,500 buildings in the following two years. The lack of recent information about this aspect has leaded to carry out a detailed analysis of urban change. This was performed in a G.I.S. (Geographical Information System) environment by transforming raster topographic and satellite data into vector data, resulting in a net balance of 1027 buildings lost from 1965 to 2005 (Fig. 5.4).

In order to verify the correlation between the subsidence phenomena and the collapses of buildings, destroyed objects have been classified in terms of density per cell size (50 m). The cells have been divided in 5 density classes, where classes 4 and 5 represent the most damage areas (Fig. 5.5). More details about the use of the GIS density tool will be explained in the next chapter.

The comparison of the subsidence map for the period 1963-2003 (Fig. 5.6) with the map of the destroyed buildings density (Fig.5.5), indicates a strict relation between the two processes, even if the most collapsed zone is located in a suburban hilly area that has never been deeply urbanized.

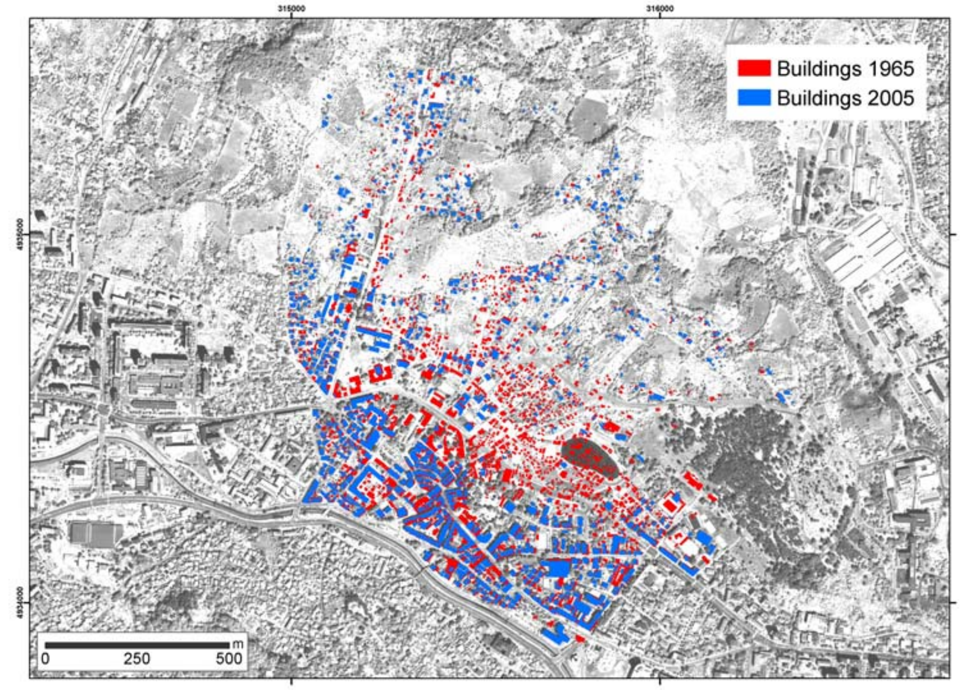

Fig. 5.4: Urban changes detected transforming raster topographic and satellite data into vector data, resulting in a net balance of 1027 buildings lost from 1965 to 2005

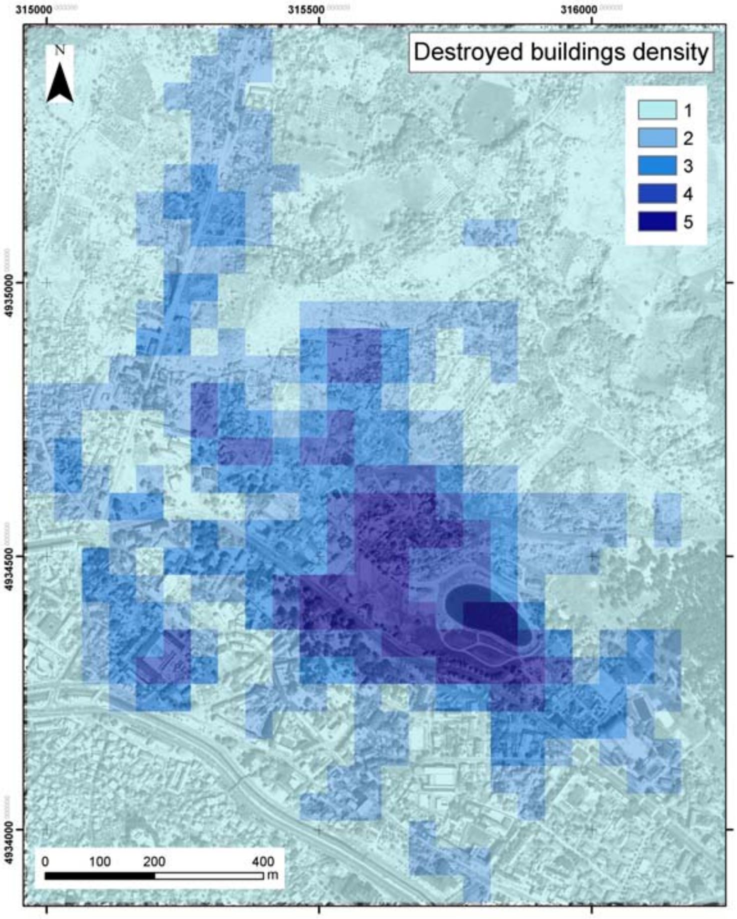

Fig. 5.5: Destroyed buildings (in red) have been classified in terms of objects density per cell size (50 m). The cells belonging to classes 4 and 5 are the most damaged

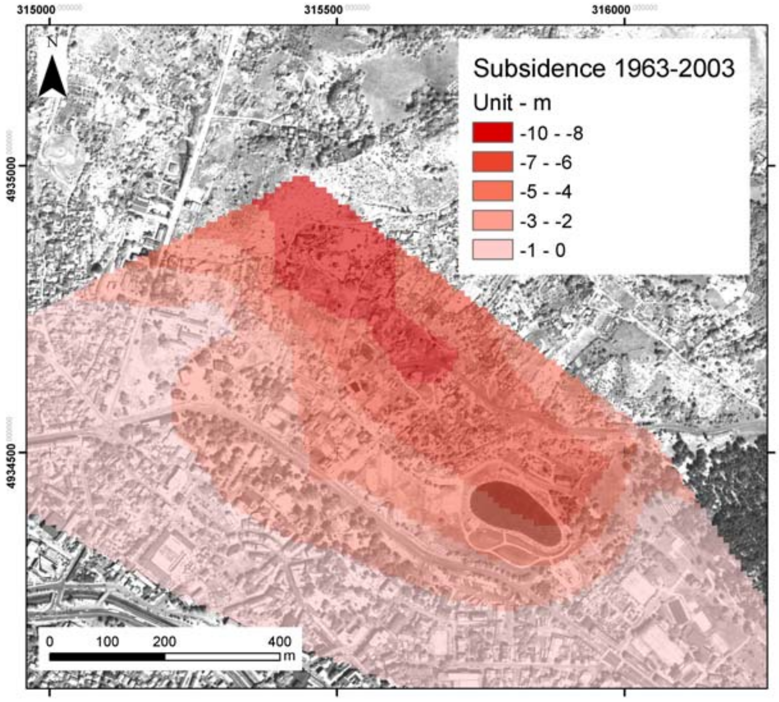

Fig. 5.6: The subsidence map for the period 1963-2003, obtained interpolating the historical data series, verifies that the most collapsed area correspond to the most damaged zones in terms of destroyed buildings (cf. fig. 5.5).

PART III

6. TUZLA RISK ASSESSMENT

Risk analysis of natural and anthropic disasters is presently adopted for several environment issues. Guidelines for risk analysis have been defined by numerous documents of national and international organizations which evidence the necessity of a logic-procedural standardized system which permits a reliable approach to the problems.

The global exposure to natural and man-made risks is nowadays very high and strictly related to development processes. For this reason risk mitigation of disastrous events is one of the development objectives adopted by the United Nation in September 2000 (UNDP/BCPR, 2004).

The process of risk management can be divided in two parts:

a) Risk Assessment. A process apt to identify and measure risks from natural events which involve people and environment.

b) Risk Evaluation. The social and political judgement of the importance of various risks by the individuals and communities that face them. This involves trading off perceived risks against potential benefits and also includes balancing scientific judgements against other factors and beliefs.

The estimation of probable future losses is a matter of increasing interest to those concerned with development planning in hazard-prone regions. Future loss estimates are of interest to those responsible for development and physical planning on an urban or regional scale, particularly where planning decisions can have an effect on future losses; for the same reason they are of interest to economic planners on a national or international scale.

Risk analysis methodologies have as a basis the concept of risk that may be defined as:

- the probability of an adverse impact occurrence multiplied by a measure of the consequence magnitude of that impact (J. G. Ganoulis, 1994).

or

- the expected losses from a given hazard to a given *element at risk,* over a specified future time period (Coburn et al. 1994).

According to the way in which the element at risk is defined, the risk may be measured in terms of expected economic loss, or in terms of numbers of lives lost or the extent of physical damage to property. The overall task of risk management must include both an estimation of the magnitude of a particular risk and the evaluation of how important to us the risk is.

Natural hazard is defined as a process or phenomenon which occurs in the bioshpere causing damages to people and objects. It is characterized by a certain frequence, magnitude, duration and harmed area extension (UNDP, 2005).

In particular, geohazard is the consequence of an adverse combination of geological processes and ground conditions precipitated by human activity, with the potential to cause harm (Rosenbaum and Culshaw, 2003).

The term implies that the event is unexpected, and likely to cause significant loss or harm.

Examples may be drawn for a wide range of situations selected from many parts of the world.

These include slope instability, subsidence, volume changes, hazards relating to water, erosion, seismicity, volcanism, glacial and periglacial phenomena and contamination.

Vulnerability is the propensity of things to be damaged by a hazard. People's lives, health and financial resources are directly at risk from the destructive effects of the hazard.

Each type of hazard puts a somewhat different set of elements at risk. Most of disaster mitigation work is focused on reducing vulnerability, and in order to act the reduction of vulnerability, development planners need an understanding of which elements are most at risk from the principal hazards which have been identified (Coburn et al., 1994).

To perform risk calculations, we need to know the probability of the occurrence of a hazard of a certain level of severity, within a specific period of time, in a given area. The level of severity of natural hazards can be quantified in terms of the magnitude of the occurrence as a whole (event parameter) or in terms of the effect the occurrence would have at a particular location (site parameter) (Coburn et al, 1994).

There are three essential components in the determination of risk:

a) *hazard occurrence probability:* the likelihood of experiencing any natural or technological hazard at a location or in a region;

b) *elements at risk:* identifying and making an inventory of people or buildings or other elements, which would be affected by the hazard if it should occurr and, where required, estimating their economic value;

c) *vulnerability* of the elements at risk: how damaged the buildings or people or other elements would be if they should experience some level of hazard.

The potential annual risk in a given area may be estimated using the formula (Varnes *1984*):

$$R = \sum H \times E \times V$$

where R is the risk, expressed in terms of victims per year or financial losses per year; H is the hazard; E the exposure or elements at risk; V the vulnerability, given by the unitary fraction of the exposure that is expected to be damaged if affected by an hazard.

7.1 TUZLA GEOHAZARD

Subsidence damage resulting from evaporite dissolution generates substantial losses throughout the world, but the causes are only well understood in a few areas (Cooper, 2002; Gutierrez and Cooper, 2002; Guerrero et al., 2004; Johnson, 2005). To deal with these hazards, a phased approach is needed in terms of identification, investigation, prediction, and mitigation (Gutierrez et al., 2008).

Tuzla subsidence, as many other natural or man-made phenomena, can be identified as geohazard. Taking into account the likelihood that a geohazard occurs, the assessment of the vulnerability of people, property and environment, provides support for decisions on what should be done to mitigate consequences (Rosenbaum and Culshaw, 2003).

The previous chapters dealt with the identification and quantification of the several factors involved in the collapsing phenomena occurring in Tuzla since about 60 years. These factors, which individually represent a single hazard, induce an overall risk to the town, in relation to the vulnerability of buildings and infrastructures. The time interval, chosen for the analysis, is the 2004-2005 because most of the available information are referred to this period.

The considered factors for the quantification of the total geohazard are:

- Annual subsidence rates;
- Shallow-fracturing intensity;
- Inferred-deep fracturing intensity;
- Annual water table rise rates.

The zone considered for the risk assessment procedure extends over an area where information about all factors are available.

All the considered hazards have been represented by a grid map with cell size of 50 meters, where the single value represents the intensity of the considered hazard for that determined cell.

Then, cell values have been divided into five classes of hazard magnitude. The cell size of 50 meters has been chosen on the basis of the available data and on the level of accuracy provided by the survey investigations and mathematical interpolations.

Most of the operations here described and in particular the overall hazard map, have been calculated by means of a map algebra tool (ESRI-ARcMap-Raster Calculator). The mathematical operations are performed between the single cell values of the considered grids, leading to the resulting grid map.

In the case of Tuzla the elements at risk are mainly buildings and infrastructures. Due to a lack of information, infrastructures are not included in the risk analysis. For what concerns inhabitants of Tuzla, the risk of death and injuries is very low or absent, because ground collapsing phenomena always occurred as gradual movements that never induced sudden building crashes.

A detailed analysis of buildings vulnerability should be done taking into account several parameters such as: age, materials, foundations, presence of cracks. Tuzla local government didn’t provide such information yet, hence the vulnerability map has been realized considering the building density in relation to presence/absence of hazards.

6.1.1 Actual subsidence rates

The annual subsidence rates calculated by means of GPS campaigns represent an important hazard for buildings stability. The subsidence map of fig. 3.8 has been recalculated over a 50 meters cell grid and then reclassified into 5 classes of hazard intensity (Fig. 6.1). Accuracy of the obtained hazard map is in the range of ± 1 cm.

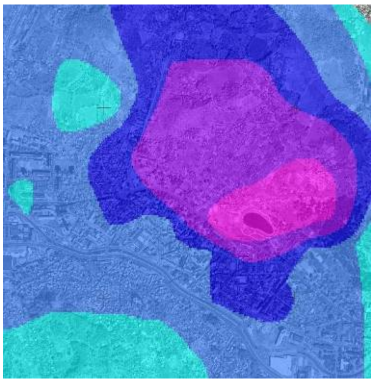

Cellsize 10 m

Annual Subsidence Rate (m)		Classes
From	To	
-0.01	0.00	1
-0.03	-0.01	2
-0.07	-0.03	3
-0.12	-0.07	4
-0.22	-0.12	5

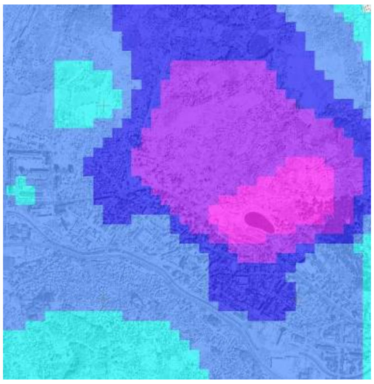

Cellsize 50 m

Fig.6.1: Annual subsidence rates have been reclassified into 5 classes of hazard intensity.

6.1.2 Visible shallow fractures

The strong subsidence that affected the area for more than 50 years has induced the formation of numerous shallow fractures which accommodated the ground movements. For what concerns the building stability, fractures represent a fundamental factor to be taken into account in the risk assessment.

During the year 2005, fractures have been mapped by DGPS technique. Unfortunately, as mentioned in chapter 5, the most fractured and faulted areas correspond to where the building have been demolished and the ground levelled. These areas, therefore, have been deeply modified by human restoring activities and it has been difficult to find clear evidence of fractures.

In order to classify the intensity of this hazard, the fractures have been analyzed by a specific ArcGIS Tool. *Line Density tool* calculates the density of linear features in the neighborhood of each output raster cell. Density is calculated in unit of length per unit of area. In this particular case the unit is expressed in meters per hectares.

Conceptually, a circle is drawn around each raster cell center using the search radius. The length of the portion of each line, that falls within the circle, is multiplied by its population field value. These figures are summed and the total is divided by the circle's area. The figure below illustrates this concept:

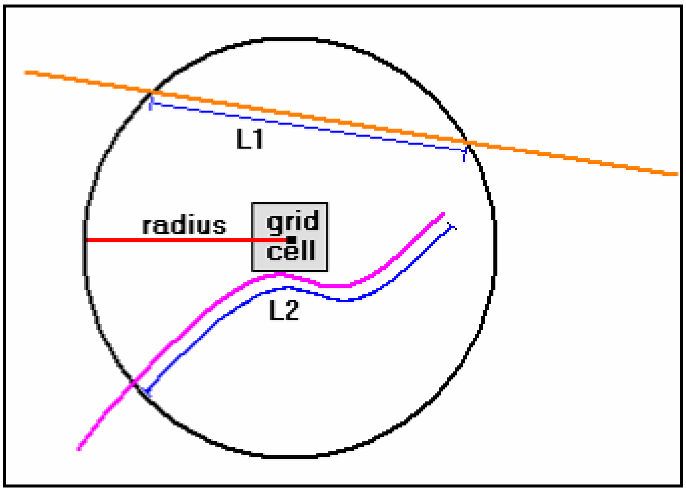

Fig. 6.2: Example showing how line density tool works.

In the illustration above, a raster cell is shown with its circular neighborhood. Lines L1 and L2 represent the length of the portion of each line that falls within the circle. The corresponding population field values are V1 and V2. Thus:

$$((L1 * V1) + (L2 * V2)) / (\text{area of circle}) = \text{Density}$$

Fracture density map and the reclassification of density values in five intensity classes, are shown in fig. 6.3. The accuracy of this method doesn't affect the precision of risk evaluation; as explained in chapter 4, the problem is connected with the absence of fractures in the area where the other analysis indicate very high likelihood of their presence.

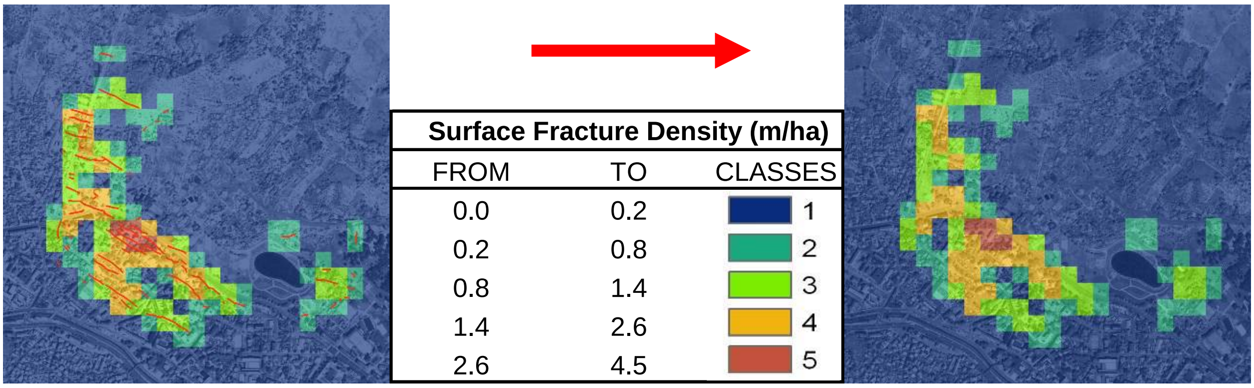

Surface Fracture Density (m/ha)

FROM	TO	CLASSES
0.0	0.2	🟦 1
0.2	0.8	🟩 2
0.8	1.4	🟩 3
1.4	2.6	🟧 4
2.6	4.5	🟥 5

Fig.6.3: Fracture density map, expressed in terms of m/ha, have been reclassified into 5 classes of hazard intensity.

6.1.3 Curvature analysis inferred fractures

Curvature analysis indicates where ground deformations appear to be more relevant. The inferred fractures obtained by the Gaussian curvature map (Fig. 6.4) have been processed by the same density tool of mapped fractures and reclassified in 5 hazard intensity classes (Fig. 6.5)

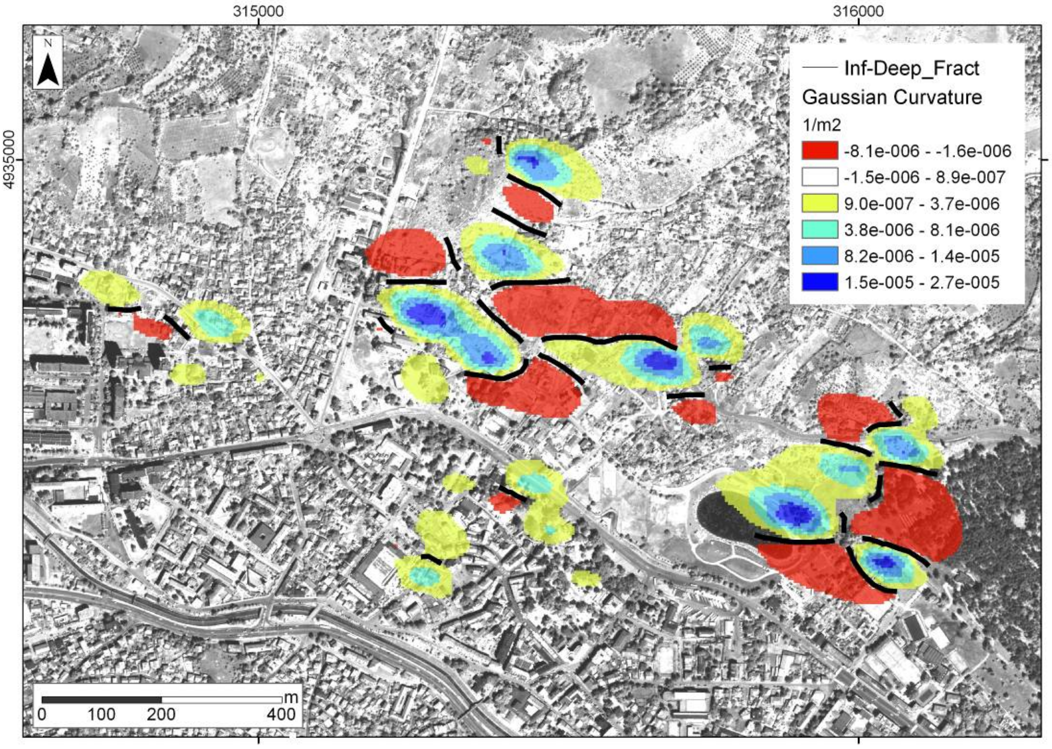

Fig.6.4: Inferred fractures have been extrapolated by the Gaussian curvature map.

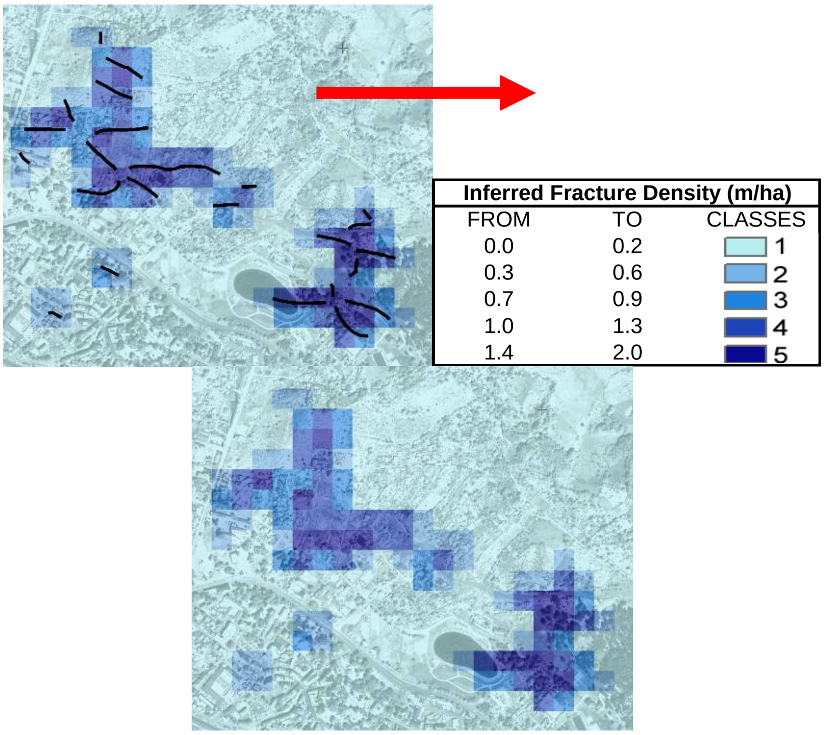

Fig.6.5: Inferred fracture density map, expressed in terms of m/ha, have been reclassified into 5 classes of hazard intensity

Accuracy of this methodology depends on the source surface used for the analytical calculation of curvature; the interpolation technique adopted for the creation of this surface is explained in paragraph 4.2.2. It is possible to argue that this approach confirms the hypothesis of intense presence of fractures where there is not evidence of deformation. In this way the parts of the town considered safe by the fracture density classification (cfr. previous paragraph) can be recasted as quite dangerous by this factor.

6.1.4 Water table rise

Even if not directly connected with subsidence and fractures, the water table rise that is currently occurring in Tuzla, represents a serious hazard to take into account for the risk assessment.

Results of the analysis explained in paragraph 2.3.1 provided two different informations:

- Water table level of different years along the period 1979-2004
- Rates of water table rise obtained by the correlation of different years

The principle adopted to quantify and classify this hazard, is that the most threatened areas are located where, given the present rates of water table rise (fig.6.6), the water will reach the surface in less years (fig. 6.7).

This has been accomplished by means of a map algebra tool (ESRI-Raster Calculator) dividing the annual water rise map by the water table level map (year 2004). The reclassification of the result leads to a map with five hazard intensity classes (fig. 6.8).

On the other hand, it could be possible to invert the ratio in the calculus, obtaining the number of years needed to the water for submerging the area. This relation is obviously more intuitive, but numerous cell values of the map showed in fig. 6.6 are very close to zero and the results of this map algebra calculus are not significant because of their too widely spaced statistical dispersion.

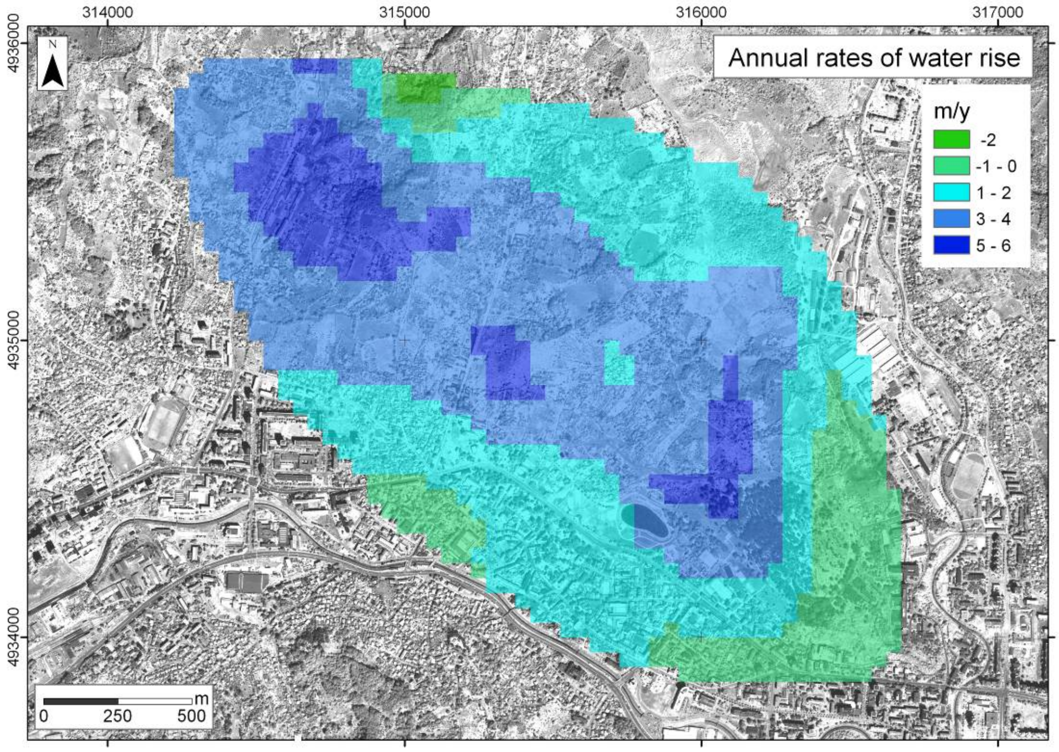

Fig.6.6: Annual rates of water rise, calculated by the comparison of water table levels map of the year 2000 and 2004.

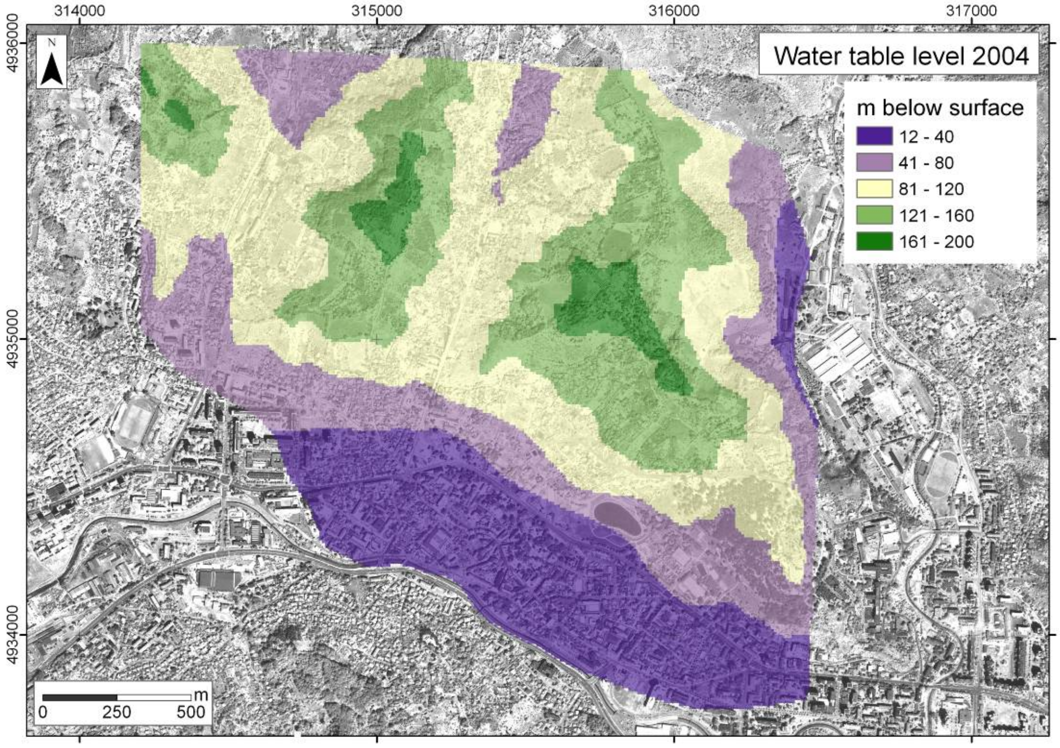

Fig.6.7: Water table level of the year 2004.

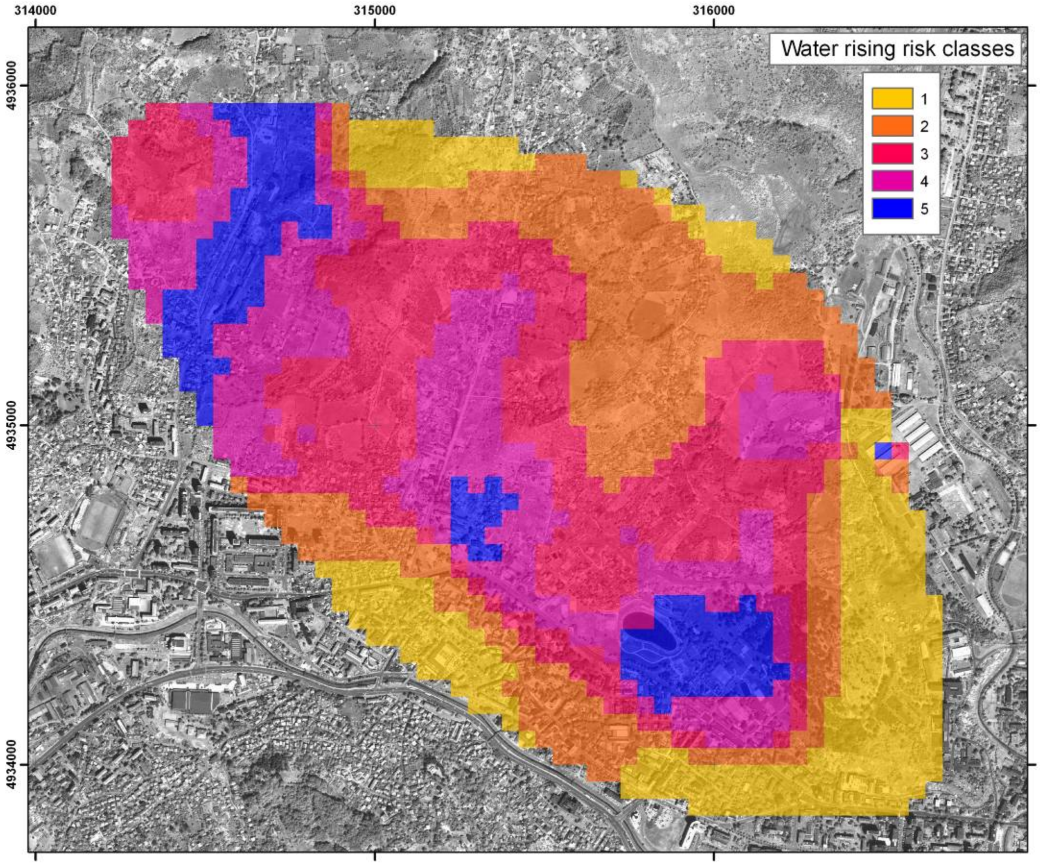

Fig. 6.8: Intensity classes map for water table rise hazard

6.2 OVERALL GEOHAZARD MAP

6.2.1 Multicriteria analysis

From selecting sites for new hospitals, schools, and factories, to managing natural hazards, forests and rivers, to creating and maintaining highways and bridges, public and private organizations are often called on to make decisions on geographic questions that involve a multitude of alternatives and often conflicting evaluation criteria (Malczewski, 1999).

In Tuzla study, the impact of the considered hazard factors on buildings is different; in order to create the overall hazard map, a multicriteria analysis has been implemented to define the relative weight of single hazards.

Multicriteria anlysis is a management procedure which decision-makers adopt to correlate different alternatives and to choose the most reliable. This techniques allow to create a classification of alternatives giving them a relative weight that represents the impact or performance of that choice.

Even if the decision process is strictly related with the personal opinion of decision-makers, multicriteria analysis sensibly reduces the subjective components of the specific alternative.

Generally this technique is used in managerial activities, but it is adopted also to evaluate risks connected to natural or man-made hazards (Chang et al, 2008; Gonçalves J.M. et al., 2007; Hermans, 2007; Malczewski, 2006).

Several typologies of multicriteria analysis are available depending on the application field. In this study the MacBeth model has been implemented (Bana e Costa et al., 2003; 2006). The relative weight of the considered hazards is obtained by means of a matrix of factors compared two at a time (Table 6.1 and 6.2).

In table 6.1 and 6.2, value 1 indicates that the factor in the matrix row is considered more important of the factor in the matrix column (value 0 indicates the contrary). In the column "Weight" values are given by the sum of row values divided by the sum of "Total" column values. The fictitious factor is introduced as reference scale (otherwise the weight of the less important factor should be zero) and by definition it looses all the comparisons.

Water table rise that is affecting Tuzla area represents a serious problem for the future urban development, but it is not strictly related to the other considered factors even if there should be some connections between fresh water infiltration and fractures; Furthermore the rates of water rise depends on the local planners decision because it is strongly influenced by the pumping wells which are currently used to limit the phenomenon.

Hence the two different scenarios have been created, and the second one includes the water rise factor.

Weight criterium is based on the hypothesis that building stability and integrity are more influenced respectively by fractures than by water flooding, subsidence and lastly by inferred fractures.

This choice is due to the fact that inferred fractures are obtained by a mathematical calculation, hence, even if their impact on building could be very high, their reliability is not enough consistent as subsidence and water table flooding.

Hazard	Subsidence Rates	Visible Fractures	Inferred Fractures	Fictitious F.	Total	Relative Weight
Subsidence Rates	\	0	1	1	2	0.33
Visible Fractures	1	\	1	1	3	0.50
Inferred Fractures	0	0	\	1	1	0.17
Fictitious F.	0	0	0	\	0	0.00

Table 6.1: Multicriteria analysis for Scenario 1

Hazard	Subsidence Rates	Water Rising	Visible Fractures	Inferred Fractures	Fictitious F.	Total	Relative Weight
Subsidence Rates	\	0	0	1	1	2	0.20
Water Rising	1	\	0	1	1	3	0.30
Visible Fractures	1	1	\	1	1	4	0.40
Inferred Fractures	0	0	0	\	1	1	0.10
Fictitious F.	0	0	0	0	\	0	0.00

Table 6.2: Multicriteria analysis for Scenario 2

The mathematical formulas adopted for the calculation of the overall hazard map are:

$$Hazard_1 = Subsidence \cdot 0.33 + Fractures \cdot 0.5 + Inferred\ Fractures \cdot 0.17$$

$$Hazard_2 = Subsidence \cdot 0.20 + Water\ rise \cdot 0.30 + Fractures \cdot 0.4 + Inferred\ Fractures \cdot 0.10$$

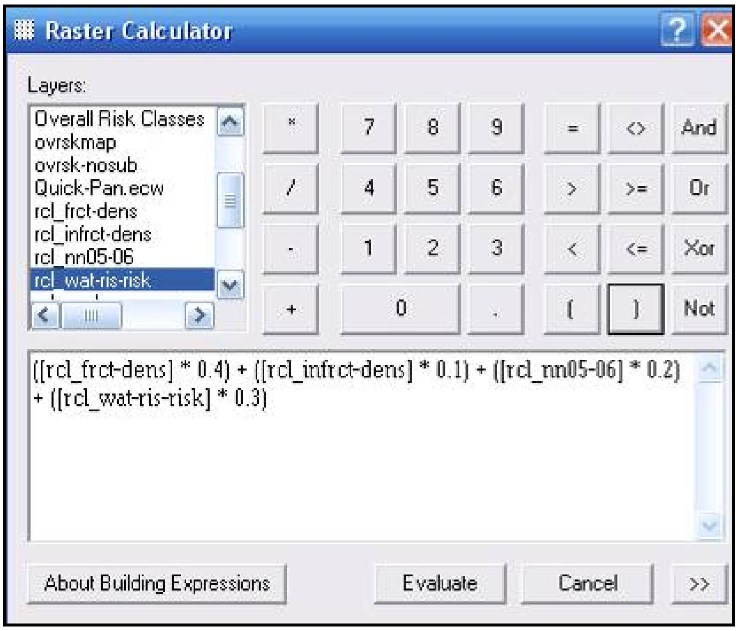

```
([rcl_frct-dens] * 0.4) + ([rcl_infrct-dens] * 0.1) + ([rcl_nn05-06] * 0.2)
+ ([rcl_wat-ris-risk] * 0.3)
```

Fig. 6.8: ESRI Raster Calculator window used for the creation of overall hazard maps

6.2.2 Results, Scenario1-2

Overall hazard map obtained for scenario 1 (Fig. 6.9) shows how just a small part of the town is influenced by ground movements. The cells belonging to classes 4 and 5 are the most threaten by fractures and subsidence.

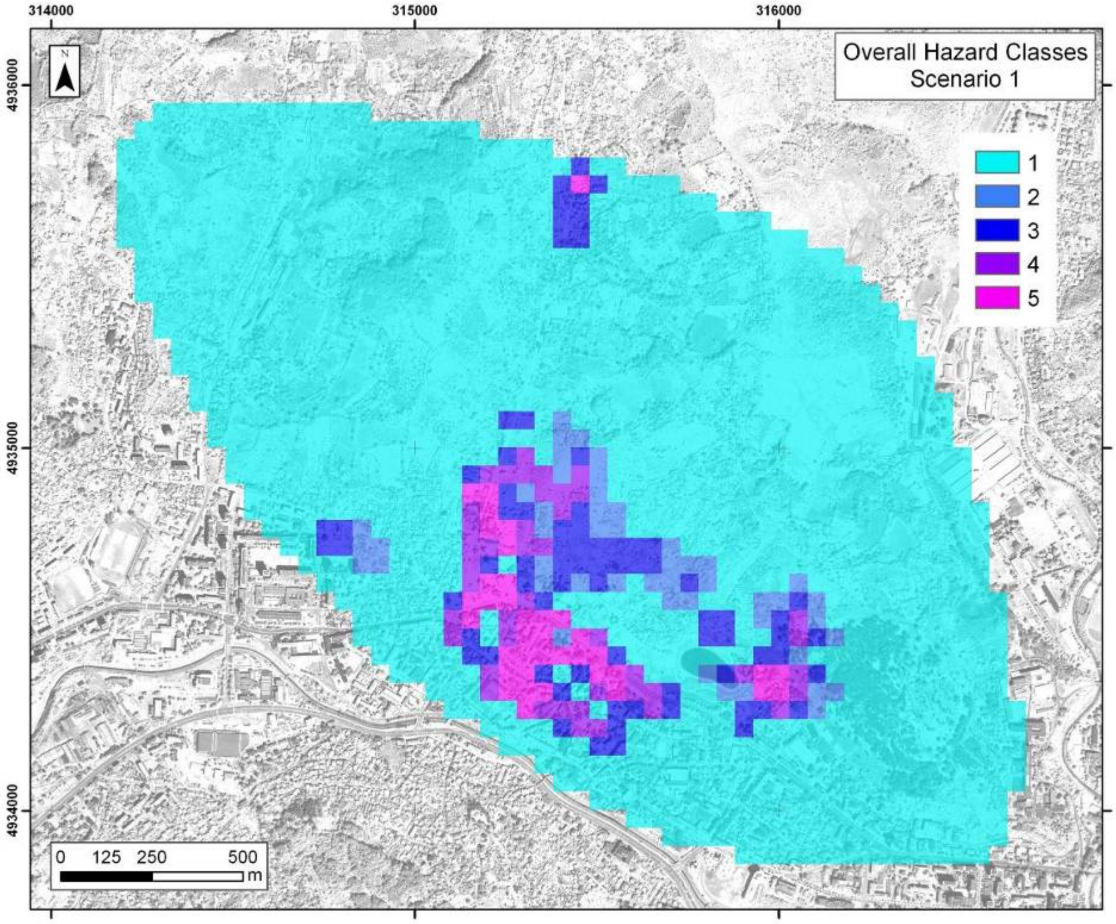

Fig. 6.9: Overall hazard map for Scenario 1 (Considered hazards: Visible Fractures, Inferred fractures, Subsidence)

Overall hazard map obtained for scenario 2 (Fig. 6.9) shows that high magnitude hazard is more widely spaced then Scenario 1, indicating how the flooding threaten could affects a considerable part of the town.

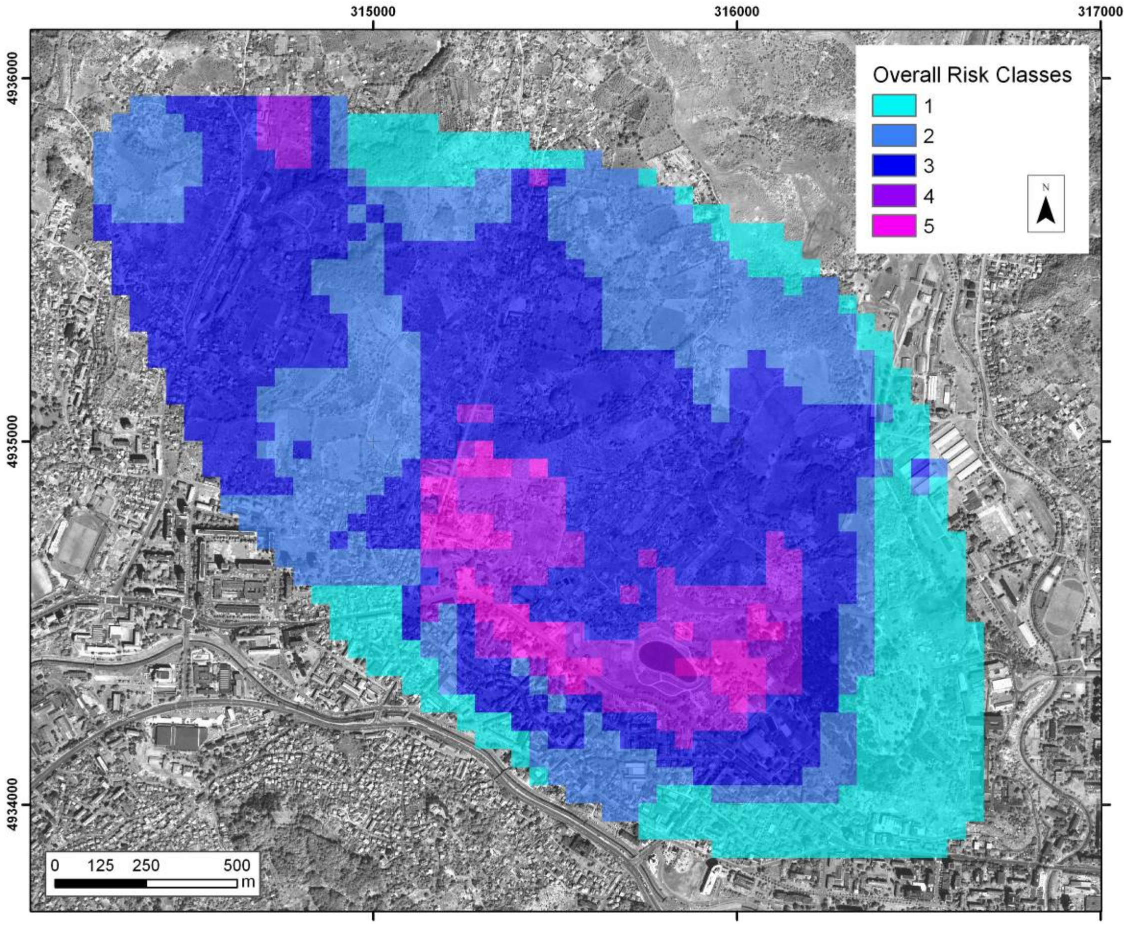

Fig. 6.10: Overall hazard map for Scenario 2 (Considered hazards: Visible Fractures, Inferred fractures, Subsidence and water table rise).

6.3 Buildings vulnerability

Because of the heterogeneous displacements of hazard magnitude, buildings vulnerability has been calculated considering their location: buildings located in a cell of high hazard intensity should be more vulnerable than buildings located in safe areas.

Building density has been calculated by means of the same procedure used for fracture density classifications. The building density map (fig. 6.11) is expressed in meters of walls per hectare, wile fig. 6.12 represents the map of buildings density classes.

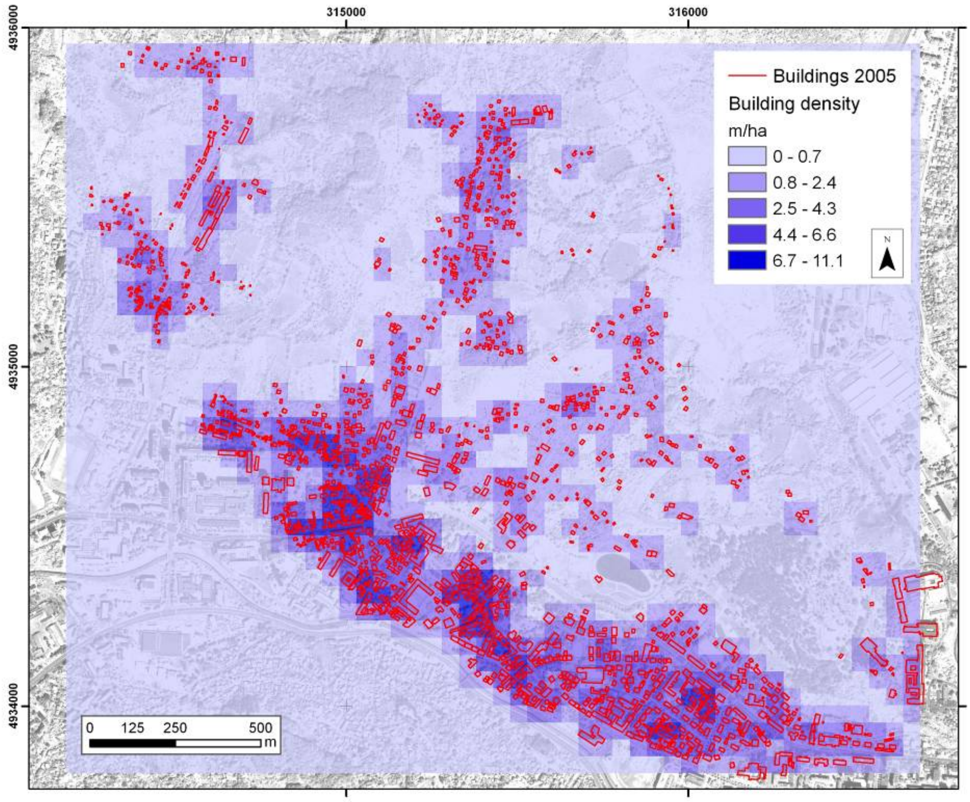

Fig. 6.11: Buildings density obtained by the Density Tool computation

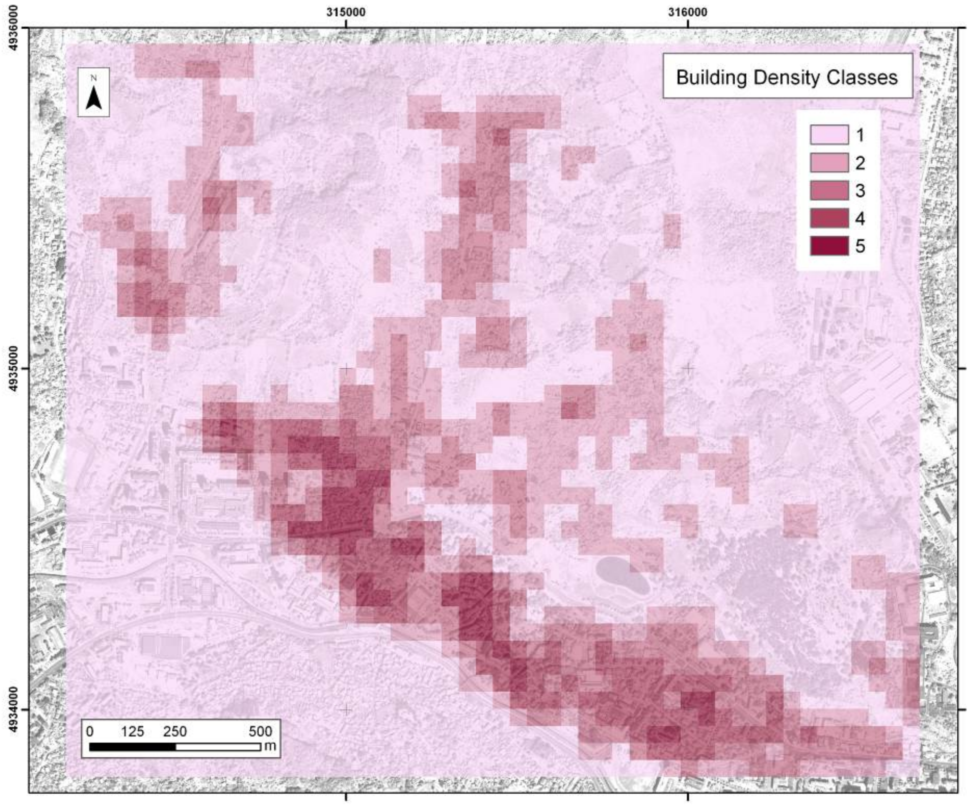

Fig. 6.12: Buildings density classes map

6.4 OVERALL RISK MAP

The previous paragraphs explained how to calculate the hazard affecting Tuzla and the vulnerability of buildings in function of their location.

As explained by the formula mentioned at the beginning of the chapter, risk can be calculated multiplying the hazard per the vulnerability.

6.4.1 Results - Scenario 1

The results of product between hazard map of scenario 1 and the building vulnerability map are shown in fig. 6.13

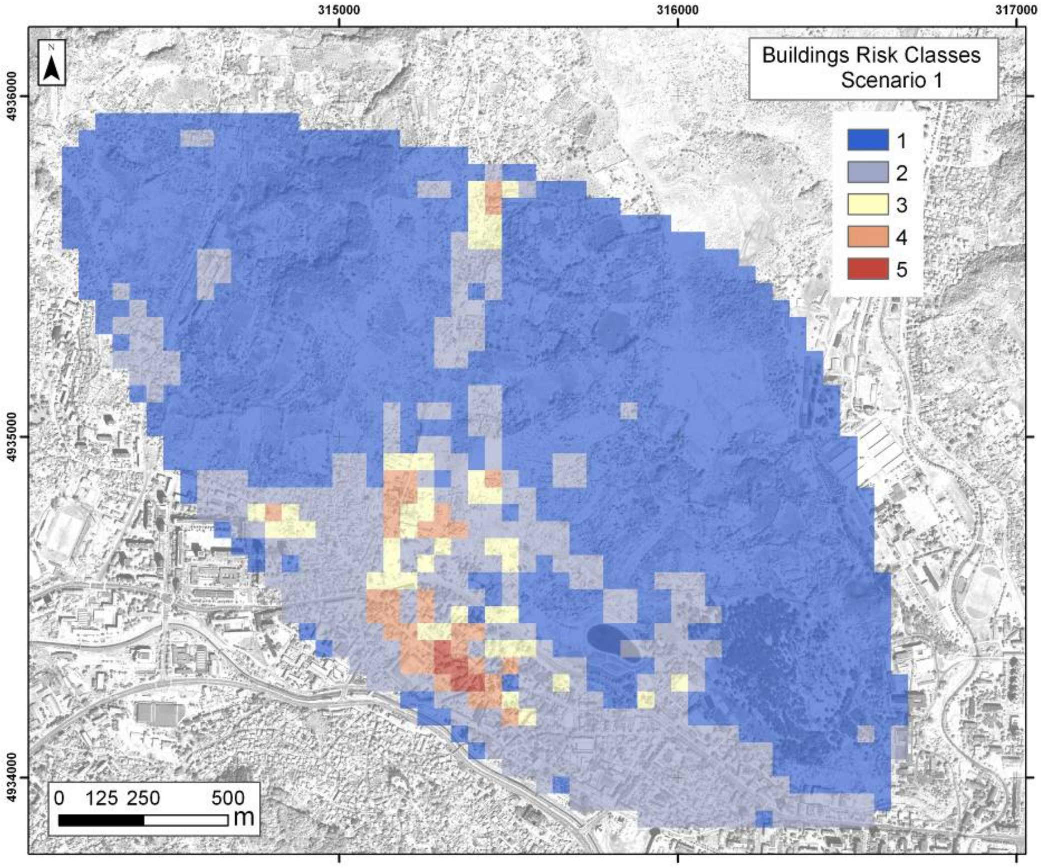

Fig. 6.13: Tuzla Risk map for Scenario1.

6.4.2 Results - Scenario 2

The results of product between hazard map of scenario 1 and the building vulnerability map are shown in fig. 6.14

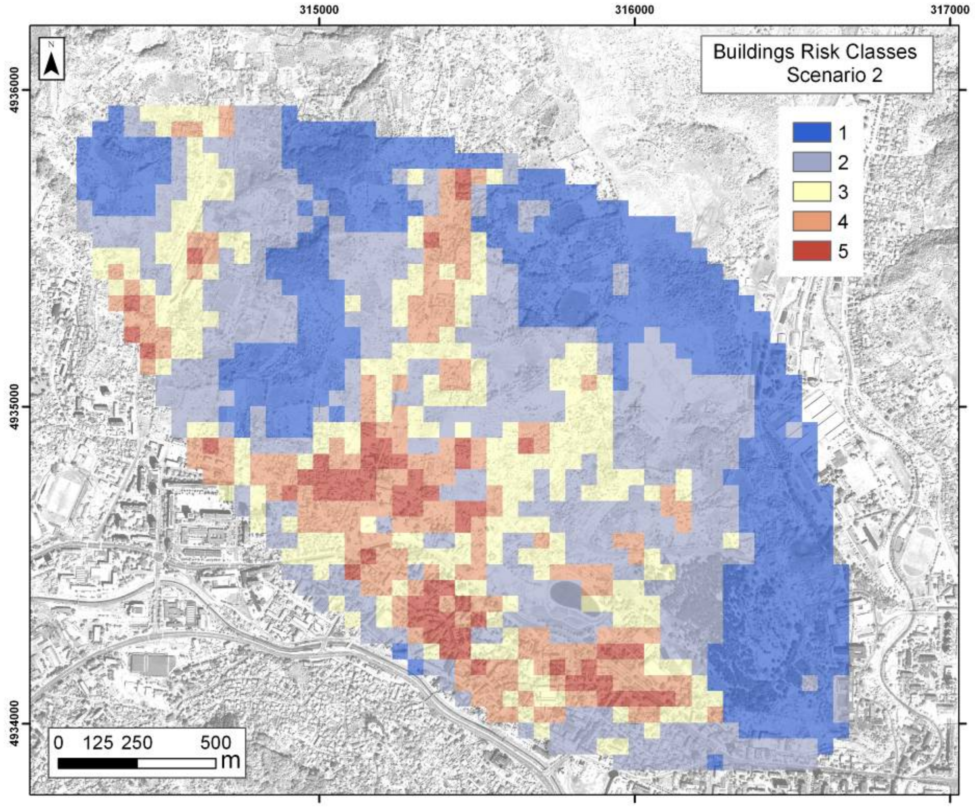

Fig. 6.14: Tuzla Risk map for Scenario1.

The overall risk maps, obtained by the multiplication of hazard and vulnerability maps, shows the most dangerous areas, in these zones the local administration must put their attention concerning the urban planning decisions.

Decision makers could take into account the provided maps in order to distinguish safe areas from the parts of the town where new constructions are not recommended.

As previously mentioned, the Scenario 2 considers the water table rise that seriously threatens the central part of the town. Nowadays local government is still extracting saltwater via wells in order to contain the water rise. This process unfortunately induces new salt dissolution as occurred in the past, favoring the creation or extension of fractures. Besides the area threatened by flooding is already deeply damaged by the collapsing phenomena and it is actually used as recreative park. This planning management doesn't consider the possibility of leaving that area to be flooded, stopping definitively the subsidence.

CONCLUSIONS

The collapsing phenomena that affect the town of Tuzla are the consequence of wild brine pumping activities carried out along the last 100 years. Solution mining processes have changed the natural groundwater system leading to uncontrolled salt dissolution of the underground karpathian evaporite deposits. Severe damages have been occurred to buildings and infrastructures.

Several factors are involved in the collapsing phenomena such as subsidence, water table oscillations, shallow and deep fractures.

The objective of this dissertation was the identification and quantification of the most important hazard factors, in order to evaluate the risk connected to buildings vulnerability. All data have been processed by means of a geographic information system, leading to the creation of geospatial referenced risk maps. Besides the new data collected along the investigation period, a large historical archive containing, topographic, geological, hydrogeological, salt extraction information, was available.

The subsidence has been monitored and investigated using geodetic surveying systems (GPS) along the last four years. This very accurate positioning methodology permitted to estimate the annual subsidence rates by means of a reference network installed around the town, and a more dense network within the subsidence area.

Surveys have been carried out performing a static relative positioning which allows to the elimination of the errors that normally affect the GPS system, estimating the benchmark positions with centimetric accuracy. Data have been post processed by means of specific geodetic software.

The obtained subsidence rates indicate an annual decrease of the phenomenon along the interval 2004-2007. In the 2004 the most collapsing area was subjected to more than 20 cm/y while in the 2007 it was subjected to about 10 cm/y.

The second considered hazard factor is represented by the numerous fractures that have been generated by the collapsing processes. These are the principal cause of building damages and collapses. The fractures identification have been carried out mapping with GPS the visible shallow fractures and estimating the covered shallow and deep fractures by means of the curvature analysis. This mathematical approach consists into the analysis of geometric surfaces identifying the areas where curvature values are subjected to rapid changes, which probably indicate where a fault or fracture is located. In particular the data source used for the surface calculation is represented by the overall subsidence rates over the period 1956-2003, while previous studies calculate curvature on topographic and seismic data; these surfaces need a previous data filtering operation in order to avoid from the calculation irrelevant information that negatively affect the results. The subsidence envelope surface used in this study represents just the ground movements representing an ideal surface to study curvature.

The mathematical calculation has been carried out in two and three dimensional ways leading to the identification of shallow and deep fractures respectively. The obtained curvature values maps helps in the identification of fractures where it was not materially possible to recognize them because of man-made ground restoration activities.

The last hazard analyzed factor is represented by the water table rise that is occurring in the most collapsed part of Tuzla. A systematic monitoring of the ground water level has been carried out by the University of Tuzla, leading to the identification of the water table oscillations occurred during the last 25 years.

Geospatial interpolations and numerical operations of water table levels leaded to the creation of maps indicating respectively the present (2004) water table level and the annual rates of water rise. These indicate that brine pumping activities strongly influenced the water table level, inducing a lowering of about 100 meters during the period of most intensive exploitation, but after the termination of the extraction the groundwater level began to rise rapidly and nowadays is threatening of flooding the central part of the town.

Finally a risk assessment procedure implemented in a geographic information system has been carried out assigning five intensity classes to the single hazard maps (represented by grid cells). All the identified hazards have been handled by a multicriteria decision making system that permitted to assign a relative weight to the single hazard in order to calculate the overall hazard map. The risk evaluation connected with buildings vulnerability has been realized considering the density of buildings in relation to the dangerousness that characterized the single grid cells.

Two different scenarios have been realized considering respectively the subsidence and the fractures for the scenario 1, and the subsidence, the fractures and the water table rise for the scenario 2. The obtained final risk maps shows the areas where buildings are threatening by land instability and risk of flooding.

The objectives achieved by this study could represent a useful tool for the local government in order to began a reliable urban planning of the town supported by scientific decision making procedures.

Between the several mitigation interventions that should be taken into account the suggestion is to persevere in the fractures monitoring because it is a very important aspect for the building stability and because fractures permit the infiltration of fresh water in the underground inducing new salt dissolution.

Nowadays the local government imposes brine pumping activities in order to prevent the submersion of the most collapsed area, but that induces further salt dissolution causing land subsidence. The possibility of leaving the most damaged area to his natural courses, investing funds and resources in safer areas, should be taken into account.

On the other hand it could be possible to perform a controlled brine pumping, injecting synthetics resins or similar viscous substances to diminish or arrest the water infiltration and salt dissolution.

AKNOWLEDGEMENTS

A sincere appreciation to the technical staff of the Municipality of Tuzla, in particular to Rusmir Salihović and Toni Nikolić who were indispensable for the installation of the GPS network and for all the field campaigns carried out along four years.

The scientific support of the University of Tuzla was fundamental for the characterization of the geological and hydrogeological features; a particular aknowledgement is for Dr. Zijad Ferhatbegović and Dr. Rejhana Redzepović who provided numerous documents and publications and helped in the translation from Bosnian language.

REFERENCES

AGUILAR F.J., AGÜERA F., AGUILAR M.A., CARVAJAL F. (2005). Effects of terrain morphology, sampling density, and interpolation methods on grid DEM accuracy. Photogrammetric Engineering and Remote Sensing 71, 805–816.

ALLWARDT P. F., BELLAHSEN N., POLLARD D. D. (2007). Curvature and fracturing based on global positioning system data collected at Sheep Mountain anticline, Wyoming. Geosphere vol. 3; no. 6; p. 408-421. Geological Society of America.

ANDRAJCHOUK V., KLIMCHOUK A. (1993). Environmental change and human Impact on karst in the Western Ukraine. In: Williams P (eds) Karst Terrains, Environmental Change and Human Impact, Vol. 25 Suppl., Catena, 147–160.

ARCGIS Desktop Help – ESRI 2006

ARINC RESEARCH CORPORATION (2000). Interfacew control document, Navstar GPS space segment/navigation user interfaces, ICD-GPS200, revision C (IRN-200C-004). Available under the Web site http://www.navcen.uscg.mil/gps.

ARUP GEOTECHNICS (1990). Review of mining instability in Great Britain, Stafford brine pumping. Arup Geotechnics for the Department of the Environment, vol 3/vi

BAKALOVIĆ, M. (2005). The city on a grain of salt. The Museum of Eastern Bosnia, Tuzla.

BANA E COSTA C.A., AÑTAO DA SILVA P., NUNES CORREIA F. (2003). Multicriteria evaluation of flood control measures: The case of Ribeira do Livramento. The London School of Economics and Political Science, London.

BANA E COSTA C.A, OLIVEIRA C. S., VIEIRA V. (2006). Prioritization of bridges and tunnels in earthquake risk mitigation using multicriteria decision analysis: Application to Lisbon. Omega,Vol. 36, Issue 3, pp. 442-450.

BELL. F.G. (1975). Salt and subsidence in Cheshire, England. Engineering Geology 9, 237-247.

BENITO G., GUTIÉRREZ F., PÉREZ-GONZÁLEZ A., MACHADO M.J. (1998). River response to Quaternary subsidence due to evaporite solution (Gallego River, Ebro Basin, Spain). Geomorphology 22, 243–263.

BENITO G., GUTIÉRREZ F., PÉREZ-GONZÁLEZ A., MACHADO M.J. (2000). Geomorphological and sedimentological features in Quaternary fluvial systems affected by solution-induced subsidence (Ebro Basin, Spain). Geomorphology 33, 209–224.

BITELLI G., BONSIGNORE F., UNGUENDOLI M. (2000). Levelling and GPS networks to monitor ground subsidence in the Southern Po Valley. Journal of Geodynamics 30(3), 355-369.

BRUS D.J., DE GRUIJTER J.J., MARSMAN B.A., VISSCHERS R., BREGT A.K., BREEUWSMA A. (1996). The performance of spatial interpolation methods and choropleth maps to estimate properties at points: a soil survey case study. Environmetrics 7, 1–16.

BURROUGH P.A., MCDONNELL R.A. (1998). Principles of Geographical Information Systems. Oxford University Press, New York. 333 pp.

CARRARA A., BITELLI G., CARLA R. (1997). Comparison of techniques for generating digital terrain models from contour lines. International Journal of Geographical Information Science 11, 451–473.

CALVERT A.F. (1915). Salt in Cheshire. Spon Ltd, London, 1206 pp.

CICIĆ S. (2002). Geological composition and tectonic terrain of Bosnia and Herzegovina(in Bosnian). In: Hrvatović H (eds) Geological Guidebook through Bosnia and Herzegovina, Sarajevo-Geological Survey of Federation Bosnia and Herzegovina, Ustanicka, Sarajevo.

CHANG N. B., PARVATHINATHAN G., BREEDEN J. B. (2008). Combining GIS with fuzzy multicriteria decision-making for landfill siting in a fast-growing urban region. Journal of Environmental Management, Vol. 87, Issue 1, pp 139-153.

CHAPLOT V., DARBOUX F., BOURENNANE H., LEGUEDOIS S., SILVERA N., PHACHOMPHON K. (2006). Accuracy of interpolation techniques for the derivation of digital elevation models in relation to landform types and data density. Geomorphology, Volume 77, Issues 1-2, Pages 126-141.

CHRZANOWSKI A., SZOSTAK-CHRZANOWSKI A., BASTIN G., LUTES J. (2000). Monitoring and modelling of ground subsidence in mining areas: case studies. Geomatica 54(4), 405-413.

CHILINGARIAN G.V., DONALDSON E.C., YEN T.F. (1996). Subsidence due to fluid withdrawal. International Journal of Rock Mechanics and Mining Sciences and Geomechanics Abstracts 33(3), 110A-110A(1).

COBURN A.W., SPENCE R.J.S., POMONIS A. (1994). Vulnerability and Risk Assessment. 2nd Edition. UNDP Disaster Management Training Programme

COE J.A., ELLIS W.L., GODT J.W., SAVAGE W.Z., SAVAGE J.E., MICHAEL J.A., KIBLER J.D., POWERS P.S., LIDKE D.J., DEBRAY S. (2003). Seasonal movement of the Slumgullion landslide determined from Global Positioning System surveys and field instrumentation, July 1998–March 2002. Engineering Geology 68, 67–101.

COLLINS J.F.N. (1971). Salt: a policy for the control of salt extraction in Cheshire. Cheshire County Council.

COOPER A.H. (1988). Subsidence resulting from the dissolution of Permian gypsum in the Ripon area; its relevance to mining and water abstraction. In Bell FG et al. (eds) Engineering Geology of Underground Movements 5, 387–390.

COOPER A.H. (1996). Gypsum Karst of Great Britain. In: Klimchouk A, Lowe D, Cooper A, Sauro U (eds) Gypsum Karst of the World, International Journal of Speleology 25(3– 4), 195– 202.

COOPER A.H., WALTHAM A.C. (1999). Subsidence caused by gypsum dissolution at Ripon, North Yorkshire. Quarterly Journal of Engineering Geology 32, 305–310.

COOPER A.H. (2002). Halite karst geohazards (natural and man-made) in the United Kingdom. Environmental Geology 42, 505– 512.

DECLERCQ F.A.N. (1996). Interpolation methods for scattered sample data: accuracy, spatial patterns, processing time. Cartography and Geographic Information Systems 23, 128–144.

DONIA R.J., FINE J.V.A. (1994). Bosnia-Hercegovina, a tradition betrayed. C Hurst & Co Publishers Ltd., 318 pp.

D.O.O. MINING INSTITUTE OF TUZLA (2000). Controlling subsidence problem in city Tuzla, Bosnia & Herzegovina. Technical Report.

FORD D.C., WILLIAMS P. (1989). Karst geomorphology and hydrology. Unwin Hyman, London, p 601.

GALLICHAND J., MARCOTTE D. (1993). Mapping clay content for subsurface drainage in the Nile delta. Geoderma 58, 165–179.

GANOULIS J. G. (1994). Engineering Risk analysis of Water Pollution. Probabilities and Fuzzy Sets. VCH, Weinheim.

GARLEFF K., KUGLER H., POSCHINGER A.V., STERR H., VILLWOCK G. (1997). Germany. In: Embleton C, (eds.) Geomorphological Hazards of Europe. Developments in Earth Surface Processes 5, 147– 177.

GILI J.A., COROMINAS J., RIUS J. (2000). Using Global Positioning System techniques in landslide monitoring. Engineering Geology 55, 167–192.

GONÇALVES J.M., PEREIRA L.S., FANG S.X., DONG B. (2007). Modelling and multicriteria analysis of water saving scenarios for an irrigation district in the upper Yellow River Basin. Agricultural Water Management,Vol. 94, Issues 1-3, pp. 93-108.

GUERRERO J., GUTIÉRREZ F., LUCHA P. (2004). Paleosubsidence and active subsidence due to evaporite dissolution in the Zaragoza area (Huerva River valley, NE Spain): processes, spatial distribution and protection measures for transport routes. Engineering Geology 72, 309–329.

GUTIÉRREZ M., GUTIÉRREZ F. (1998). Geomorphology of the tertiary gypsum formations in the Ebro Depression (Spain). Geoderma 87, 1– 29.

GUTIÉRREZ F., ORTÍ F., GUTIÉRREZ M., PÉREZ-GONZÁLEZ A., BENITO G., GRACIA J., DURÁN VALSERO J.J. (2001). The stratigraphical record and activity of evaporite dissolution subsidence in Spain. Carbonates and Evaporites 16(1), 46– 70.

GUTIÉRREZ F., ORTÍ F., GUTIÉRREZ M., PÉREZ-GONZÁLEZ A., BENITO G., GRACIA J., DURÁN VALSERO J.J. (2002). Paleosubsidence and active subsidence due to evaporite dissolution in Spain. Carbonates and Evaporites 17(2), 121– 133.

GUTIÉRREZ F., COOPER A.H. (2002). Evaporite dissolution subsidence in the historical city of Calatayud, Spain: damage appraisal and prevention. Natural Hazards 25, 259– 288.

GUTIÉRREZ-SANTOLALLA F., GUTIÉRREZ-ELORZA M., MARÍN C., MALDONADO C., YOUNGER P.L.(2005). Subsidence hazard avoidance based on geomorphological mapping in the Ebro River valley mantled evaporite karst terrain (NE Spain). Environmental Geology 48, 370-383.

GUTIERREZ F., COOPER A.H., JOHNSON K.S. (2008). Identification, prediction, and mitigation of sinkhole hazards in evaporite karst areas. Environmental Geology 53, 1007-1022

HERMANS C., ERICKSON J., NOORDEWIER T., SHELDON A., KLINE M. (2007). Collaborative environmental planning in river management: An application of multicriteria decision analysis in the White River Watershed in Vermont. Journal of Environmental Management,Vol. 84, Issue 4, pp. 534-546.

HOFMANN-WELLENHOF B., LICHTENEGGER H., COLLINS J. (2001). GPS, Theory and Practice (fifth revised ed.). Springer-Verlag New York Inc., New York.

HRVATOVIĆ H. (2006). Geological guidebook trough Bosnia and Herzegovina. Sarajevo-Geological Survey of Federation Bosnia Herzegovina, Ustanicka, Sarajevo.

IVANOV S. S. (1989). Effect of changes in curvature of the surface of the oceanic lithosphere on its stress state. Oceanology, vol. 29, p. 465-468.

JOHNSON K.S. (1997). Evaporite karst in the United States. Carbonates and Evaporites 12 (1), 2-14.

JOHNSON K.S. (2005). Subsidence hazards due to evaporite dissolution in the United States. Environmental Geology 48, 395-409.

JOVANOVIĆ O. (1980). Genesis of Pretortonian Miocene sediments in North Bosnia, between Una and Orina River (in Serbian).Geoloski glasnik, XVI. Sarajevo.

KATZER F. (1903). Geological guide through Bosnia and Herzegovina, Sarajevo (in Bosnian). In: Hrvatović H. (eds) Geological Guidebook through Bosnia and Herzegovina, Sarajevo-Geological Survey of Federation Bosnia and Herzegovina, Ustanicka, Sarajevo.

KIRKHAM R.M., STREUFERT R.K., KUNK M.J., BUDAHN JR., HUDSON MR., PERRY W. JR. (2002). Evaporite tectonism in the lower roaring fork river valley, west-central Colorado. In: Kirkham RM, Scott RB, Judkins W (eds) Late cenozoic evaporite tectonism and volcanism in west-central Colorado, vol 366, Geological Society of America special paper, Boulder, Colorado, pp 73–99.

LASLETT G.M. (1994). Kriging and splines: an empirical comparison of their predictive performance in some applications. Journal of the American Statistical Association 89, 391–409.

LI X., WANG S.J., LIU T.Y., MA F.S. (2004). Engineering geology, ground surface movement and fissures induced by underground mining in the Jinchuan Nickel Mine. Engineering Geology 76, 93-107.

MALCZEWSKI J. (1999). GIS and multicriteria decision analysis. Wiley J. and Sons ed. 408pp.

MALCZEWSKI J. (2006). Ordered weighted averaging with fuzzy quantifiers: GIS-based multicriteria evaluation for land-use suitability analysis. International Journal of Applied Earth Observation and Geoinformation, Vol. 8, Issue 4,pp. 270-277.

MALET J.P., MAQUAIRE O., CALAIS E. (2002). The use of Global Positioning System techniques for the continuous monitoring of landslides—application to the Super-Sauze earthflow (Alpesde Haute-Provence, France). Geomorphology 43, 33–54.

MANCINI F., STECCHI F., GABBIANELLI G., DZINDO A. (2005). Ground collapsing in the city of Tuzla (Bosnia & Herzegovina). 32th International Symposium on Remote Sensing of Environment, Saint Petersburg, Russian Federation, 20-24 June 2005.

MURRAY G. H. (1968). Quantitative fracture study-Sanish Pool, McKenzie County, North Dakota. American Association of Petroleum Geologists Bulletin, v. 52, p. 57-65.

NOTHARD S., MCKENZIE D., HAINES J. AND JACKSON J. (1996). Gaussian curvature and the relationship between the shape and the deformation of the Tonga slab: Geophysical Journal International, v. 127, p. 311-327.

ORUČ E., MANDŽIĆ E. (2005). Hydrological and hydrodynamic consideration about Tuzla salt deposit. Internal document of the Faculty of Mining, Geology and Civil Engineering (RFFG) of the University of Tuzla. Serbian-Croatian language.

PARISE M., GUNN J. (2007). Natural & anthropogenic hazards in karst areas: Recognition, Analysis, Mitigation. GSL Special Publication.

PAUKŠTYS B., COOPER A.H., ARUSTIENE J. (1999). Planning for gypsum geohazards in Lithuania and England. Engineering Geology 52, 93–103.

RAUCOULES D., MAISONS C., CARNEC C., LE MOUELIC S., KING C., HOSFORD S. (2003). Monitoring of slow ground deformation by ERS radar interferometry on the Vauvert salt mine (France). Comparison with ground-based measurement. Remote Sensing of Environment 88, 468–478.

REDŽEPOVIĆ R., MANDŽIĆ E. (2005). Geological, geotechnical and geomechanical characterization of Tuzla salt deposit. Internal document of the Faculty of Mining, Geology and Civil Engineering (RFFG) of the University of Tuzla. Serbian-Croatian language.

REUTER F., STOYAN D. (1993). Sinkholes in carbonate, sulphate and chloride karst regions: principles and problems of engineering geological investigations and predictions, with comments for the construction and mining industries. In: Beck BF (eds) Fourth Multidisciplinary Conference on Sinkholes and the Engineering and the Environmental Impacts of Karst. Panama City, Florida.

ROBESON S.M. (1997). Spherical methods for spatial interpolation: review and evaluation. Cartography and Geographic Information Systems 24, 3–20.

ROSENBAUM M.S. AND CULSHAW M.G. (2003). Communicating the risks arising from geohazards. Journal of Royal Statistic Society. Vol. 166, Part 2, pp. 261–270.

SIBSON R. (1981). A Brief Description of Natural Neighbour Interpolation. Chapter 2 in Interpolating multivariate data, John Wiley & Sons, New York, , pp. 21-36.

SORIANO M.A., SIMÓN J.L. (1995). Alluvial dolines in the central Ebro basin, Spain: a spatial and developmental hazard analysis. Geomorphology 11, 295–309.

SORIANO M.A., SIMÓN J.L. (2001). Subsidence rates of alluvial dolines in the central Ebro Basin, northeastern Spain. In: Beck B, Herring JG (eds) Geotechnical and environmental applications of karst geology and hydrology. Balkema, Rotterdam, 47–52.

SORIANO M.A., SIMÓN J.L. (2005). Subsidence rates and urban damages in alluvial dolines of the Central Ebro basin (NE Spain). Environmental Geology 42, 476-484.

SOKLIĆ I. (1959). Miocene Paleogeography and origin of salt deposits in Tuzla.(in Croatian). In: Hrvatović H (eds) Geological Guidebook through Bosnia and Herzegovina, Sarajevo-Geological Survey of Federation Bosnia and Herzegovina, Ustanicka, Sarajevo.

SOKLIĆ I. (1964). Origin and structures of the Tuzla basin. Geoloski glasnik. In: Hrvatović H (eds) Geological Guidebook through Bosnia and Herzegovina, Sarajevo-Geological Survey of Federation Bosnia and Herzegovina, Ustanicka, Sarajevo.

SOKLIĆ I. (1982). Stratigraphy and age of salt formations in Tuzla.(in Croatian), Radevi ANUBiH, Odj. teh. Nauka, 7, 135-151.

STECCHI F., MANCINI F., GABBIANELLI G. (2006). G.I.S. as a tool for data management and ground deformations analysis in the city of Tuzla (BiH). Proceedings of the 5th Congress on Regional Geological Cartography and Information Systems, Barcelona, Spain, 13-15 June.

STEVANOVIĆ P. (1977). Pont. (Ed. Geology of the Bosnia and Herzegovina), Book Ill-Cenozoic periods. In: Hrvatović H. (eds) Geological Guidebook through Bosnia and Herzegovina, Sarajevo-Geological Survey of Federation Bosnia and Herzegovina, Ustanicka, Sarajevo.

STEWART J. (1995). Multivariable calculus. Pacific Grove, Brooks/Cole Publishing Company, 1018 p.

STEWART S. A. AND PODOLSKI R. (1998). Curvature analysis of gridded surfaces, in M. P. Coward, T. S. Daltaban, and H. Johnson, eds., Structural Geology in Reservoir Characterization, v.

127: London, Geological Society, Special Publications, p. 133-147.

STRUIK D. J. (1961). Lectures on classical differential geometry. Addison-Wesley Series in

Mathematics. London, Addison-Wesley Publishing Company, Inc., 231 p.

TARI V., PAMIĆ J. (1998). Geodynamic evolution of the northern Dinarides and the southern part of the Pannonian Basin. Tectonophysics 297, 269-281.

TATIĆ M. (1979). Environment protection against the consequences of subsidence in town of Tuzla, Bosnia & Herzegovina. Community Head-Office for Construction of Tuzla.

TEATINI P., TOSI L., STROZZI T., CARBOGNIN L., WEGMÜLLER U., PIZZETTO F. (2005) Mapping regional land displacements in the Venice coastland by an integrated monitoring system. Remote Sensing of Environment, 98, 403 – 413

TOULEMONT M. (1984). Le karst gypseux du Lutétien supérieur de la région parisienne: Caractéristiques et impact sur le milieu ur bain. Revue de Géologie Dynamique et de Géographie Physique 25(3), 213– 228.

UNDP/BCPR (2004). “Reducing disaster risk. A challenge for development. A Global Report”. United Nations Development Programme / Bureau for Crisis Prevention and Recovery, New York.

UNDP / World Bank / FAO, 2005, “Report Joint Tsunami Disaster Assessment Mission: Livelihood Recovery & Environmental Rehabilitation” 4 - 8 January 2005.

VENI G., DUCHENE H., CRAWFORD N.C., GROVES C.G., KASTNING E.H., HUPPERT G., OLSON R.A., WHEELER B. (2001). Living With Karst: A Fragile Foundation. American Geological Institute, Environmental Awareness Series Vol. 4.

VRABAC S. (1999). Facial and biostratigraphic characteristics of Badenian and Sarmatian in North Bosnia (in Bosnian), Tuzla. In: Hrvatović H (eds) Geological Guidebook through Bosnia and Herzegovina, Sarajevo-Geological Survey of Federation Bosnia and Herzegovina, Ustanicka, Sarajevo.

WATSON D. (1992). Contouring: A Guide to the Analysis and Display of Spatial Data”. Pergamon Press, London.

WEBER D., ENGLUND E. (1992). Evaluation and comparison of spatial interpolators. Mathematical Geology 24, 381–391.

WEBER D., ENGLUND E. (1994). Evaluation and comparison of spatial interpolators II. Mathematical Geology 26, 589–603.

WILLIAMS P. (2003). Dolines. In: Gunn J (ed) Encyclopedia of caves and karst science. Fitzroy Dearborn, New York, pp 304–310.

WILSON J.P., GALLANT J.C. (2000). Terrain Analysis. Principles and Applications. Wiley, New York. 479 pp.

ZIMMERMAN D., PAVLIK C., RUGGLES A., ARMSTRONG M. (1999). An experimental comparison of ordinary and universal kriging and inverse distance weighting. Mathematical Geology 31, 375–390.

WEB-SITES

http://igs.bkg.bund.de/
http://igscb.jpl.nasa.gov
http://itrf.ensg.ign.fr/ITRF_solutions/2000/sol.php
http://www.navcen.uscg.mil/gps
http://www.undp.org/bcpr/

ANNEXES

---

www.terrasat.de ***GeoGenius 2000, Copyright (C) 1997 - 2000 by Spectra Precision Terrasat GmbH, 24/01/2008,17.13.06***

Reference network 2004

Statistiche	
Compensazione della Rete in WGS84.	
Numero di baselines	31
Numero di misure di campagna	0
Modello del Geoide	None
Numero di punti di controllo in WGS84	4
Numero di punti compensati	10
Livello di Confidenza	1 Sigma
Livello di Significanza per il tau test	1.00 %
Errore standard dell'unità di peso	3.565
Numero di iterazioni	1

Punto	Lat [Deg]	Lon [Deg]	H ell. [m]	ort.H [m]	geoid.H [m]	sN [mm]	sE [mm]	sH [mm]
0010	N 44° 31' 59.79808"	E 18° 40' 28.01302"	360.1966	360.1966	0.0000	9.7	20.3	18.8
0054	N 44° 33' 47.90127"	E 18° 40' 12.35330"	460.3608	460.3608	0.0000	12.2	21.0	22.1
0162	N 44° 32' 39.76865"	E 18° 41' 39.61416"	302.5869	302.5869	0.0000	10.4	20.5	19.9
0483	N 44° 32' 35.14992"	E 18° 38' 42.10832"	372.0535	372.0535	0.0000	9.0	20.2	17.7
0486	N 44° 31' 31.68378"	E 18° 39' 24.48981"	380.9431	380.9431	0.0000	10.5	20.8	20.6
5042	N 44° 31' 43.14581"	E 18° 41' 42.73620"	291.3023	291.3023	0.0000	12.2	20.6	22.1
MATE	N 40° 38' 56.87347"	E 16° 42' 16.05349"	535.6395	535.6395	0.0000	0.0	0.0	0.0
MEDI	N 44° 31' 11.84553"	E 11° 38' 48.53329"	50.0181	50.0181	0.0000	0.0	0.0	0.0
PENC	N 47° 47' 22.57049"	E 19° 16' 53.50316"	291.7425	291.7425	0.0000	0.0	0.0	0.0
SOFI	N 42° 33' 21.94003"	E 23° 23' 41.03711"	1119.5302	1119.5302	0.0000	0.0	0.0	0.0

Subsidence network 2004

Statistiche	
Compensazione della Rete in WGS84.	
Numero di baselines	83
Numero di misure di campagna	0
Modello del Geoide	None
Numero di punti di controllo in WGS84	6
Numero di punti compensati	60
Livello di Confidenza	1 Sigma
Livello di Significanza per il tau test	1.00 %
Errore standard dell'unità di peso	1.044
Numero di iterazioni	1

Punto	Lat [Deg]	Lon [Deg]	H ell. [m]	ort.H [m]	geoid.H [m]	sN [mm]	sE [mm]	sH [mm]
0003	N 44° 32' 04.68325"	E 18° 41' 14.28435"	282.6358	282.6358	0.0000	23.4	14.3	33.0
0005	N 44° 32' 09.87038"	E 18° 41' 10.12861"	282.4095	282.4095	0.0000	10.0	7.4	18.2
0010	N 44° 31' 59.79882"	E 18° 40' 28.01395"	360.1964	360.1964	0.0000	0.0	0.0	0.0
0012	N 44° 32' 16.27852"	E 18° 40' 18.46701"	274.8111	274.8111	0.0000	6.5	4.0	10.8
0028	N 44° 32' 28.66161"	E 18° 41' 02.77981"	341.8211	341.8211	0.0000	7.0	5.2	13.6
0030	N 44° 32' 25.56675"	E 18° 41' 06.81400"	326.1103	326.1103	0.0000	21.9	12.9	30.4
0032	N 44° 32' 40.39899"	E 18° 40' 37.10412"	331.0567	331.0567	0.0000	15.4	8.1	16.5
0033	N 44° 32' 41.16383"	E 18° 40' 17.76214"	348.3057	348.3057	0.0000	13.7	10.2	28.5
0038	N 44° 32' 46.45835"	E 18° 40' 52.27509"	392.3686	392.3686	0.0000	14.2	8.1	36.0
0041	N 44° 33' 16.01788"	E 18° 40' 48.99527"	423.2902	423.2902	0.0000	10.5	6.3	14.7
0044	N 44° 32' 12.81115"	E 18° 41' 02.54741"	279.6813	279.6813	0.0000	19.5	9.3	20.1
0045	N 44° 32' 09.11892"	E 18° 40' 58.72702"	279.0286	279.0286	0.0000	8.2	5.6	14.4
0046	N 44° 33' 16.42182"	E 18° 39' 36.84388"	436.2603	436.2603	0.0000	6.6	5.1	13.9
0051	N 44° 33' 10.82828"	E 18° 40' 05.08386"	298.2360	298.2360	0.0000	9.1	8.4	19.1
0052	N 44° 32' 17.74517"	E 18° 40' 54.46866"	274.7705	274.7705	0.0000	14.0	9.2	38.3
0054	N 44° 33' 47.90210"	E 18° 40' 12.35430"	460.3607	460.3607	0.0000	0.0	0.0	0.0
0054_2	N 44° 32' 18.64204"	E 18° 40' 47.02476"	273.7352	273.7352	0.0000	14.4	20.8	61.7
0055	N 44° 32' 16.31196"	E 18° 40' 45.90953"	275.1626	275.1626	0.0000	9.6	9.5	24.3
0059	N 44° 33' 00.32290"	E 18° 40' 00.90325"	290.7765	290.7765	0.0000	10.4	8.1	19.4
0062	N 44° 32' 09.43101"	E 18° 40' 46.97669"	277.9493	277.9493	0.0000	10.8	11.1	24.1
0066	N 44° 32' 12.91215"	E 18° 40' 54.72441"	277.4016	277.4016	0.0000	22.2	21.8	44.4
0085	N 44° 32' 15.39573"	E 18° 40' 26.03545"	275.5481	275.5481	0.0000	11.0	8.1	19.3
0095	N 44° 32' 16.42935"	E 18° 40' 42.20539"	274.8616	274.8616	0.0000	15.2	10.2	27.1
00F1	N 44° 32' 18.35272"	E 18° 40' 36.94207"	274.5887	274.5887	0.0000	8.7	7.8	18.6
00F2	N 44° 32' 18.45834"	E 18° 40' 33.73708"	276.7105	276.7105	0.0000	5.2	5.9	18.0
0105	N 44° 32' 25.32962"	E 18° 40' 22.50190"	280.5207	280.5207	0.0000	24.6	11.7	25.1
0107	N 44° 32' 32.77437"	E 18° 40' 24.88216"	284.2982	284.2982	0.0000	15.6	12.0	27.7
0116	N 44° 32' 28.14957"	E 18° 40' 30.67202"	275.8869	275.8869	0.0000	16.7	11.1	24.9
0119	N 44° 32' 24.18843"	E 18° 40' 35.60966"	272.7144	272.7144	0.0000	27.2	18.6	37.0
0121	N 44° 32' 22.61651"	E 18° 40' 39.06435"	272.0606	272.0606	0.0000	8.2	5.8	24.7
0124	N 44° 32' 21.35592"	E 18° 40' 31.47440"	276.2929	276.2929	0.0000	8.0	4.9	10.9
0134	N 44° 32' 19.80686"	E 18° 40' 16.40076"	274.1286	274.1286	0.0000	7.7	7.1	18.1

0155	N 44° 32' 18.02641"	E 18° 40' 08.86940"	273.7023	273.7023	0.0000	9.4	5.1	13.9
0162	N 44° 32' 39.76918"	E 18° 41' 39.61502"	302.5947	302.5947	0.0000	0.0	0.0	0.0
0183	N 44° 32' 48.22473"	E 18° 40' 31.70070"	296.8558	296.8558	0.0000	3.4	3.1	11.9
0190	N 44° 32' 29.91305"	E 18° 40' 48.57224"	291.4175	291.4175	0.0000	15.2	13.6	45.8
0256	N 44° 32' 56.83574"	E 18° 40' 03.52591"	313.6174	313.6174	0.0000	15.4	8.7	34.8
0318	N 44° 32' 28.74942"	E 18° 39' 47.23972"	276.0468	276.0468	0.0000	11.6	8.6	15.0
0333	N 44° 32' 32.55002"	E 18° 40' 05.67110"	276.5133	276.5133	0.0000	9.8	5.5	12.5
0347	N 44° 32' 25.26168"	E 18° 39' 54.73786"	273.4483	273.4483	0.0000	7.2	8.6	22.3
0470	N 44° 32' 20.26392"	E 18° 41' 19.02418"	349.3834	349.3834	0.0000	23.4	18.8	44.6
0483	N 44° 32' 35.15051"	E 18° 38' 42.10940"	372.0502	372.0502	0.0000	0.0	0.0	0.0
0486	N 44° 31' 31.68437"	E 18° 39' 24.49048"	380.9412	380.9412	0.0000	0.0	0.0	0.0
0531	N 44° 33' 08.21908"	E 18° 40' 39.55940"	332.3754	332.3754	0.0000	13.1	7.8	21.9
0552	N 44° 32' 14.53317"	E 18° 41' 14.21600"	297.8737	297.8737	0.0000	15.2	10.9	23.3
0553	N 44° 32' 12.97731"	E 18° 41' 17.18843"	304.4621	304.4621	0.0000	22.6	19.8	47.6
0561	N 44° 32' 04.56739"	E 18° 41' 24.17333"	283.0926	283.0926	0.0000	19.8	14.7	37.7
0562	N 44° 32' 04.56560"	E 18° 41' 24.17328"	283.0776	283.0776	0.0000	27.2	14.2	34.5
0633	N 44° 32' 17.07634"	E 18° 41' 06.29024"	284.6309	284.6309	0.0000	8.1	5.6	25.7
1381	N 44° 33' 01.98212"	E 18° 40' 21.44240"	404.6520	404.6520	0.0000	7.2	5.9	18.1
2124	N 44° 32' 16.60748"	E 18° 40' 01.95713"	273.3836	273.3836	0.0000	4.0	3.3	11.4
3010	N 44° 32' 21.83994"	E 18° 40' 47.68724"	272.9280	272.9280	0.0000	11.6	6.8	15.4
4795	N 44° 32' 15.92591"	E 18° 40' 38.44271"	276.5186	276.5186	0.0000	8.9	7.5	21.0
5042	N 44° 31' 43.14636"	E 18° 41' 42.73706"	291.2990	291.2990	0.0000	0.0	0.0	0.0
623	N 44° 32' 43.02887"	E 18° 41' 15.37657"	326.6064	326.6064	0.0000	7.1	6.4	18.0
DR-5	N 44° 31' 51.02112"	E 18° 41' 09.33981"	280.3068	280.3068	0.0000	15.1	7.9	36.9
DR-6	N 44° 32' 07.02557"	E 18° 40' 40.86967"	277.8978	277.8978	0.0000	4.8	3.6	12.0
DR-8	N 44° 32' 04.36214"	E 18° 41' 45.42597"	287.0279	287.0279	0.0000	15.7	14.2	66.7
DR-9	N 44° 32' 07.98790"	E 18° 41' 35.98202"	310.5854	310.5854	0.0000	5.7	5.3	12.6
DR10	N 44° 32' 36.16863"	E 18° 39' 52.55151"	278.1243	278.1243	0.0000	11.4	8.6	20.7

Reference network 2005

Statistiche	
Compensazione della Rete in WGS84.	
Numero di baselines	32
Numero di misure di campagna	0
Modello del Geoide	None
Numero di punti di controllo in WGS84	4
Numero di punti compensati	10
Livello di Confidenza	1 Sigma
Livello di Significanza per il tau test	1.00 %
Errore standard dell'unità di peso	3.407
Numero di iterazioni	1

Punto	Lat [Deg]	Lon [Deg]	H ell. [m]	ort.H [m]	geoid.H [m]	sN [mm]	sE [mm]	sH [mm]
0010	N 44° 31' 59.79845"	E 18° 40' 28.01241"	360.1687	360.1687	0.0000	10.1	22.3	18.7
0054	N 44° 33' 47.90159"	E 18° 40' 12.35264"	460.3372	460.3372	0.0000	10.2	22.5	18.7
0162	N 44° 32' 39.76883"	E 18° 41' 39.61328"	302.5653	302.5653	0.0000	9.8	22.3	18.4
0483	N 44° 32' 35.15003"	E 18° 38' 42.10761"	372.0223	372.0223	0.0000	10.8	22.7	20.1
0486	N 44° 31' 31.68393"	E 18° 39' 24.48872"	380.9331	380.9331	0.0000	14.5	23.8	29.3
5042	N 44° 31' 43.14589"	E 18° 41' 42.73535"	291.2757	291.2757	0.0000	9.7	22.3	18.1
MATE	N 40° 38' 56.87406"	E 16° 42' 16.05450"	535.6383	535.6383	0.0000	0.0	0.0	0.0
MEDI	N 44° 31' 11.84590"	E 11° 38' 48.53399"	50.0151	50.0151	0.0000	0.0	0.0	0.0
PENC	N 47° 47' 22.57089"	E 19° 16' 53.50423"	291.7423	291.7423	0.0000	0.0	0.0	0.0
SOFI	N 42° 33' 21.94040"	E 23° 23' 41.03817"	1119.5296	1119.5296	0.0000	0.0	0.0	0.0

Subsidence network 2005

Statistiche	
Compensazione della Rete in WGS84.	
Numero di baselines	103
Numero di misure di campagna	0
Modello del Geoide	None
Numero di punti di controllo in WGS84	6
Numero di punti compensati	52
Livello di Confidenza	1 Sigma
Livello di Significanza per il tau test	1.00 %
Errore standard dell'unità di peso	0.605
Numero di iterazioni	1

Punto	Lat [Deg]	Lon [Deg]	H ell. [m]	ort.H [m]	geoid.H [m]	sN [mm]	sE [mm]	sH [mm]
0004	N 44° 32' 09.90478"	E 18° 41' 22.41078"	334.3057	334.3057	0.0000	6.4	4.3	10.4
0010	N 44° 31' 59.79882"	E 18° 40' 28.01395"	360.1964	360.1964	0.0000	0.0	0.0	0.0
0012	N 44° 32' 16.27852"	E 18° 40' 18.46698"	274.8130	274.8130	0.0000	3.8	2.4	5.9
0028	N 44° 32' 28.65387"	E 18° 41' 02.78006"	341.6066	341.6066	0.0000	6.2	3.6	9.0
0030	N 44° 32' 25.56235"	E 18° 41' 06.81019"	325.9871	325.9871	0.0000	8.0	3.4	9.9
0032	N 44° 32' 40.39532"	E 18° 40' 37.10156"	330.9219	330.9219	0.0000	4.6	4.5	12.3
0033	N 44° 32' 41.16393"	E 18° 40' 17.76193"	348.2934	348.2934	0.0000	6.1	4.0	8.7
0038	N 44° 32' 46.45676"	E 18° 40' 52.27332"	392.2975	392.2975	0.0000	3.3	2.4	8.8
0041	N 44° 33' 16.01748"	E 18° 40' 48.99451"	423.2929	423.2929	0.0000	3.3	3.4	10.2
0044	N 44° 32' 12.81136"	E 18° 41' 02.54720"	279.6854	279.6854	0.0000	5.5	3.5	10.3
0045	N 44° 32' 09.11880"	E 18° 40' 58.72680"	279.0214	279.0214	0.0000	5.4	3.6	7.7
0046	N 44° 33' 16.42164"	E 18° 39' 36.84371"	436.2503	436.2503	0.0000	2.1	1.7	3.6
0051	N 44° 33' 10.82757"	E 18° 40' 05.08317"	298.2660	298.2660	0.0000	4.6	2.7	7.4
0054	N 44° 33' 47.90210"	E 18° 40' 12.35430"	460.3607	460.3607	0.0000	0.0	0.0	0.0
0055	N 44° 32' 16.31315"	E 18° 40' 45.90910"	275.1500	275.1500	0.0000	6.5	5.8	25.3
0059	N 44° 33' 00.32280"	E 18° 40' 00.90331"	290.7559	290.7559	0.0000	2.2	1.7	7.0
0062	N 44° 32' 09.43075"	E 18° 40' 46.97688"	277.9058	277.9058	0.0000	14.4	6.5	30.1
0085	N 44° 32' 15.39579"	E 18° 40' 26.03533"	275.5462	275.5462	0.0000	5.3	3.6	8.6
0089	N 44° 32' 13.64919"	E 18° 40' 33.33136"	275.2324	275.2324	0.0000	8.5	6.2	15.6
0095	N 44° 32' 16.43064"	E 18° 40' 42.20538"	274.8330	274.8330	0.0000	15.0	9.0	27.9
00F1	N 44° 32' 18.35406"	E 18° 40' 36.94241"	274.5485	274.5485	0.0000	2.6	1.9	7.8
00F2	N 44° 32' 18.45889"	E 18° 40' 33.73739"	276.6960	276.6960	0.0000	9.9	12.2	38.2
0105	N 44° 32' 25.33004"	E 18° 40' 22.50235"	280.4937	280.4937	0.0000	11.4	7.9	21.4
0107	N 44° 32' 32.77195"	E 18° 40' 24.87988"	284.2303	284.2303	0.0000	6.2	6.2	13.4
0119	N 44° 32' 24.18702"	E 18° 40' 35.60955"	272.6388	272.6388	0.0000	14.8	7.1	32.4
0121	N 44° 32' 22.61602"	E 18° 40' 39.06452"	271.9778	271.9778	0.0000	13.2	8.4	21.1
0124	N 44° 32' 21.35676"	E 18° 40' 31.47507"	276.2360	276.2360	0.0000	4.0	2.8	7.0
0134	N 44° 32' 19.80689"	E 18° 40' 16.40071"	274.1214	274.1214	0.0000	3.5	2.1	5.4
0155	N 44° 32' 18.02637"	E 18° 40' 08.86925"	273.7012	273.7012	0.0000	3.2	1.6	8.0
0162	N 44° 32' 39.76918"	E 18° 41' 39.61502"	302.5947	302.5947	0.0000	0.0	0.0	0.0

0183	N 44° 32' 48.22246"	E 18° 40' 31.70144"	296.8147	296.8147	0.0000	7.9	3.7	9.3
0190	N 44° 32' 29.90762"	E 18° 40' 48.56499"	291.3317	291.3317	0.0000	9.3	4.3	12.8
0256	N 44° 32' 56.83574"	E 18° 40' 03.52567"	313.5893	313.5893	0.0000	4.5	3.3	8.1
0318	N 44° 32' 28.74955"	E 18° 39' 47.24029"	276.0537	276.0537	0.0000	5.4	3.1	9.1
0333	N 44° 32' 32.54976"	E 18° 40' 05.67103"	276.5096	276.5096	0.0000	2.1	1.6	5.5
0347	N 44° 32' 25.26177"	E 18° 39' 54.73857"	273.4296	273.4296	0.0000	2.6	1.8	4.7
0470	N 44° 32' 20.26455"	E 18° 41' 19.02326"	349.3575	349.3575	0.0000	7.4	4.8	11.9
0483	N 44° 32' 35.15051"	E 18° 38' 42.10940"	372.0502	372.0502	0.0000	0.0	0.0	0.0
0486	N 44° 31' 31.68437"	E 18° 39' 24.49048"	380.9412	380.9412	0.0000	0.0	0.0	0.0
0531	N 44° 33' 08.21909"	E 18° 40' 39.55895"	332.3533	332.3533	0.0000	6.7	6.2	8.4
0552	N 44° 32' 14.53314"	E 18° 41' 14.21586"	297.8685	297.8685	0.0000	4.0	3.2	9.8
0623	N 44° 32' 43.02847"	E 18° 41' 15.37656"	326.6187	326.6187	0.0000	2.2	1.5	5.7
0633	N 44° 32' 17.07657"	E 18° 41' 06.28959"	284.6234	284.6234	0.0000	1.7	1.3	5.2
1000	N 44° 32' 17.97967"	E 18° 40' 32.84522"	277.2272	277.2272	0.0000	1.5	1.2	4.4
1381	N 44° 33' 01.98186"	E 18° 40' 21.44175"	404.6451	404.6451	0.0000	5.0	2.3	9.5
2124	N 44° 32' 16.60728"	E 18° 40' 01.95687"	273.3817	273.3817	0.0000	1.7	1.2	4.1
3010	N 44° 32' 21.83593"	E 18° 40' 47.68525"	272.7118	272.7118	0.0000	6.9	5.3	13.6
4795	N 44° 32' 15.92629"	E 18° 40' 38.44281"	276.5133	276.5133	0.0000	3.7	2.9	8.4
5042	N 44° 31' 43.14636"	E 18° 41' 42.73706"	291.2990	291.2990	0.0000	0.0	0.0	0.0
DR-10	N 44° 32' 36.16867"	E 18° 39' 52.55156"	278.1236	278.1236	0.0000	3.2	2.2	9.2
DR-5	N 44° 31' 51.02142"	E 18° 41' 09.33965"	280.3011	280.3011	0.0000	2.2	1.3	3.2
DR-6	N 44° 32' 07.02523"	E 18° 40' 40.86957"	277.9108	277.9108	0.0000	11.0	7.0	18.1

Subsidence network 2006

Statistiche	
Compensazione della Rete in WGS84.	
Numero di baselines	59
Numero di misure di campagna	0
Modello del Geoide	None
Numero di punti di controllo in WGS84	6
Numero di punti compensati	51
Livello di Confidenza	1 Sigma
Livello di Significanza per il tau test	1.00 %
Errore standard dell'unità di peso	1.754
Numero di iterazioni	1

Punto	Lat [Deg]	Lon [Deg]	H ell. [m]	ort.H [m]	geoid.H [m]	sN [mm]	sE [mm]	sH [mm]
0010	N 44° 31' 59.79882"	E 18° 40' 28.01395"	360.1964	360.1964	0.0000	0.0	0.0	0.0
0012	N 44° 32' 16.27859"	E 18° 40' 18.46674"	274.8078	274.8078	0.0000	11.4	6.4	18.9
0030	N 44° 32' 25.55919"	E 18° 41' 06.80568"	325.8061	325.8061	0.0000	14.8	9.5	22.0
0032	N 44° 32' 40.39240"	E 18° 40' 37.09940"	330.8299	330.8299	0.0000	6.6	4.3	11.0
0033	N 44° 32' 41.16359"	E 18° 40' 17.76213"	348.3008	348.3008	0.0000	8.3	5.5	15.2
0038	N 44° 32' 46.45545"	E 18° 40' 52.27202"	392.2405	392.2405	0.0000	4.9	3.2	8.1
0041	N 44° 33' 16.01765"	E 18° 40' 48.99529"	423.2836	423.2836	0.0000	9.3	8.5	25.3
0044	N 44° 32' 12.81101"	E 18° 41' 02.54685"	279.6777	279.6777	0.0000	7.3	4.6	16.6
0045	N 44° 32' 09.11885"	E 18° 40' 58.72682"	279.0046	279.0046	0.0000	8.8	8.1	25.0
0046	N 44° 33' 16.42143"	E 18° 39' 36.84406"	436.2591	436.2591	0.0000	6.9	3.5	12.1
0051	N 44° 33' 10.82726"	E 18° 40' 05.08355"	298.2418	298.2418	0.0000	14.3	9.5	42.3
0052	N 44° 32' 17.74710"	E 18° 40' 54.46802"	274.7229	274.7229	0.0000	18.3	12.0	30.7
0054	N 44° 33' 47.90210"	E 18° 40' 12.35430"	460.3607	460.3607	0.0000	0.0	0.0	0.0
0055	N 44° 32' 16.31445"	E 18° 40' 45.90915"	275.1208	275.1208	0.0000	23.1	14.3	35.1
0059	N 44° 33' 00.32297"	E 18° 40' 00.90334"	290.7543	290.7543	0.0000	10.6	7.7	23.2
0062	N 44° 32' 09.44001"	E 18° 40' 47.00919"	277.4532	277.4532	0.0000	25.5	16.7	45.6
0085	N 44° 32' 15.39587"	E 18° 40' 26.03522"	275.5475	275.5475	0.0000	4.8	4.3	13.5
0095	N 44° 32' 16.43122"	E 18° 40' 42.20608"	274.8229	274.8229	0.0000	29.2	15.8	32.5
00F1	N 44° 32' 18.35483"	E 18° 40' 36.94316"	274.5245	274.5245	0.0000	3.6	2.6	11.8
00F2	N 44° 32' 18.45627"	E 18° 40' 33.70136"	277.0415	277.0415	0.0000	23.7	15.5	55.3
00F3	N 44° 32' 17.98044"	E 18° 40' 32.84569"	277.2135	277.2135	0.0000	9.6	5.7	12.6
0105	N 44° 32' 25.33062"	E 18° 40' 22.50297"	280.0938	280.0938	0.0000	21.1	11.1	29.0
0107	N 44° 32' 32.77034"	E 18° 40' 24.87820"	284.1722	284.1722	0.0000	6.7	6.6	19.7
0119	N 44° 32' 24.18529"	E 18° 40' 35.60955"	272.5391	272.5391	0.0000	16.0	14.9	45.8
0121	N 44° 32' 22.61554"	E 18° 40' 39.06520"	271.9027	271.9027	0.0000	16.2	9.8	24.8
0124	N 44° 32' 21.35744"	E 18° 40' 31.47610"	276.2418	276.2418	0.0000	17.9	9.6	26.1
0134	N 44° 32' 19.80696"	E 18° 40' 16.40044"	274.1208	274.1208	0.0000	6.1	5.5	17.6
0155	N 44° 32' 18.02638"	E 18° 40' 08.86912"	273.7061	273.7061	0.0000	4.8	3.5	13.0
0162	N 44° 32' 39.76918"	E 18° 41' 39.61502"	302.5947	302.5947	0.0000	0.0	0.0	0.0
0183	N 44° 32' 48.22040"	E 18° 40' 31.70063"	296.7710	296.7710	0.0000	6.0	3.7	13.4
0190	N 44° 32' 29.90344"	E 18° 40' 48.55913"	291.2771	291.2771	0.0000	4.6	2.7	7.4
0256	N 44° 32' 56.83592"	E 18° 40' 03.52608"	313.5802	313.5802	0.0000	12.3	8.0	17.1
0318	N 44° 32' 28.74916"	E 18° 39' 47.24012"	276.0394	276.0394	0.0000	10.0	5.7	14.0

0333	N 44° 32' 32.54982"	E 18° 40' 05.67100"	276.5108	276.5108	0.0000	5.7	3.4	12.4
0347	N 44° 32' 25.26147"	E 18° 39' 54.73867"	273.4433	273.4433	0.0000	18.9	13.3	36.2
0470	N 44° 32' 20.26388"	E 18° 41' 19.02249"	349.3760	349.3760	0.0000	14.5	10.2	19.1
0483	N 44° 32' 35.15051"	E 18° 38' 42.10940"	372.0502	372.0502	0.0000	0.0	0.0	0.0
0486	N 44° 31' 31.68437"	E 18° 39' 24.49048"	380.9412	380.9412	0.0000	0.0	0.0	0.0
0531	N 44° 33' 08.21891"	E 18° 40' 39.55893"	332.3686	332.3686	0.0000	20.9	17.4	31.1
0552	N 44° 32' 14.53260"	E 18° 41' 14.21526"	297.8719	297.8719	0.0000	25.4	17.5	25.4
0623	N 44° 32' 43.02820"	E 18° 41' 15.37589"	326.6181	326.6181	0.0000	4.7	4.0	10.9
0633	N 44° 32' 17.07665"	E 18° 41' 06.28918"	284.6276	284.6276	0.0000	8.8	7.6	21.2
1381	N 44° 33' 01.98105"	E 18° 40' 21.44184"	404.6256	404.6256	0.0000	16.5	10.1	24.3
2124	N 44° 32' 16.60736"	E 18° 40' 01.95661"	273.3881	273.3881	0.0000	14.1	8.7	19.1
3010	N 44° 32' 21.83251"	E 18° 40' 47.68432"	272.5213	272.5213	0.0000	8.9	5.2	12.0
4795	N 44° 32' 15.92650"	E 18° 40' 38.44292"	276.5162	276.5162	0.0000	4.7	3.3	12.1
5042	N 44° 31' 43.14636"	E 18° 41' 42.73706"	291.2990	291.2990	0.0000	0.0	0.0	0.0
DR-5	N 44° 31' 51.02104"	E 18° 41' 09.33944"	280.3049	280.3049	0.0000	5.9	3.9	10.2
DR-6	N 44° 32' 07.02533"	E 18° 40' 40.86943"	277.8966	277.8966	0.0000	22.8	12.3	25.7
DR-9	N 44° 32' 07.98793"	E 18° 41' 35.98182"	310.5928	310.5928	0.0000	6.9	5.5	17.9
DR10	N 44° 32' 36.16880"	E 18° 39' 52.55139"	278.1309	278.1309	0.0000	3.3	2.4	9.4

Reference network 2007

Statistiche	
Compensazione della Rete in WGS84.	
Numero di baselines	44
Numero di misure di campagna	0
Modello del Geoide	None
Numero di punti di controllo in WGS84	4
Numero di punti compensati	10
Livello di Confidenza	1 Sigma
Livello di Significanza per il tau test	1.00 %
Errore standard dell'unità di peso	2.572
Numero di iterazioni	1

Punto	Lat [Deg]	Lon [Deg]	H ell. [m]	ort.H [m]	geoid.H [m]	sN [mm]	sE [mm]	sH [mm]
10	N 44° 31' 59.79994"	E 18° 40' 28.01649"	360.2234	360.2234	0.0000	8.7	13.8	14.7
162	N 44° 32' 39.77008"	E 18° 41' 39.61767"	302.6330	302.6330	0.0000	9.2	14.1	15.9
483	N 44° 32' 35.15157"	E 18° 38' 42.11222"	372.0746	372.0746	0.0000	8.9	13.8	14.9
486	N 44° 31' 31.68540"	E 18° 39' 24.49293"	380.9464	380.9464	0.0000	10.2	14.9	18.3
5042	N 44° 31' 43.14738"	E 18° 41' 42.73958"	291.3170	291.3170	0.0000	9.4	14.4	16.8
54	N 44° 33' 47.90351"	E 18° 40' 12.35692"	460.3835	460.3835	0.0000	9.1	13.8	15.0
MATE	N 40° 38' 56.87527"	E 16° 42' 16.05661"	535.6363	535.6363	0.0000	0.0	0.0	0.0
MEDI	N 44° 31' 11.84716"	E 11° 38' 48.53657"	50.0054	50.0054	0.0000	0.0	0.0	0.0
PENC	N 47° 47' 22.57176"	E 19° 16' 53.50647"	291.7409	291.7409	0.0000	0.0	0.0	0.0
SOFI	N 42° 33' 21.94110"	E 23° 23' 41.04033"	1119.5282	1119.5282	0.0000	0.0	0.0	0.0

Subsidence network 2007

Statistiche	
Compensazione della Rete in WGS84.	
Numero di baselines	114
Numero di misure di campagna	0
Modello del Geoide	None
Numero di punti di controllo in WGS84	6
Numero di punti compensati	51
Livello di Confidenza	1 Sigma
Livello di Significanza per il tau test	1.00 %
Errore standard dell'unità di peso	0.941
Numero di iterazioni	1

Punto	Lat [Deg]	Lon [Deg]	H ell. [m]	ort.H [m]	geoid.H [m]	sN [mm]	sE [mm]	sH [mm]
10	N 44° 31' 59.79882"	E 18° 40' 28.01395"	360.1964	360.1964	0.0000	0.0	0.0	0.0
105	N 44° 32' 25.33072"	E 18° 40' 22.50278"	280.4754	280.4754	0.0000	3.6	3.4	10.8
107	N 44° 32' 32.76954"	E 18° 40' 24.87689"	284.1678	284.1678	0.0000	11.8	8.4	17.3
116	N 44° 32' 28.14264"	E 18° 40' 30.66654"	275.6777	275.6777	0.0000	12.8	7.1	25.1
119	N 44° 32' 24.18445"	E 18° 40' 35.60950"	272.5482	272.5482	0.0000	4.2	3.8	14.3
12	N 44° 32' 16.27840"	E 18° 40' 18.46665"	274.8006	274.8006	0.0000	8.4	5.3	11.0
121	N 44° 32' 22.61491"	E 18° 40' 39.06579"	271.9139	271.9139	0.0000	14.3	5.7	13.0
124	N 44° 32' 21.35805"	E 18° 40' 31.47621"	276.2565	276.2565	0.0000	7.8	5.1	13.5
134	N 44° 32' 19.80648"	E 18° 40' 16.40040"	274.1333	274.1333	0.0000	5.8	2.4	13.5
1381	N 44° 33' 01.98094"	E 18° 40' 21.44138"	404.6251	404.6251	0.0000	9.5	5.7	12.0
155	N 44° 32' 18.02657"	E 18° 40' 08.86942"	273.7274	273.7274	0.0000	7.3	5.3	19.7
162	N 44° 32' 39.76918"	E 18° 41' 39.61502"	302.5947	302.5947	0.0000	0.0	0.0	0.0
183	N 44° 32' 48.22017"	E 18° 40' 31.70028"	296.7915	296.7915	0.0000	4.0	2.7	6.7
190	N 44° 32' 29.90166"	E 18° 40' 48.55779"	291.2975	291.2975	0.0000	11.2	5.6	10.5
2124	N 44° 32' 16.60744"	E 18° 40' 01.95698"	273.3943	273.3943	0.0000	5.4	3.5	7.2
256	N 44° 32' 56.83541"	E 18° 40' 03.52503"	313.5894	313.5894	0.0000	3.0	2.2	5.7
28	N 44° 32' 43.02825"	E 18° 41' 15.37593"	326.4983	326.4983	0.0000	5.1	3.3	8.4
30	N 44° 32' 25.55707"	E 18° 41' 06.80331"	325.7127	325.7127	0.0000	10.8	7.8	18.1
3050	N 44° 32' 23.57417"	E 18° 40' 56.69635"	277.8803	277.8803	0.0000	18.8	13.2	24.6
318	N 44° 32' 28.74906"	E 18° 39' 47.23993"	276.0636	276.0636	0.0000	8.9	6.7	16.4
32	N 44° 32' 40.39150"	E 18° 40' 37.09926"	330.8272	330.8272	0.0000	4.6	3.3	8.2
33	N 44° 32' 41.16370"	E 18° 40' 17.76154"	348.2996	348.2996	0.0000	8.3	4.7	9.7
333	N 44° 32' 32.55045"	E 18° 40' 05.67101"	276.5304	276.5304	0.0000	5.9	3.0	14.0
347	N 44° 32' 25.25827"	E 18° 39' 54.73062"	273.6284	273.6284	0.0000	16.3	11.4	31.4
38	N 44° 32' 46.45515"	E 18° 40' 52.27189"	392.2206	392.2206	0.0000	4.3	2.9	7.1
41	N 44° 33' 16.01752"	E 18° 40' 48.99456"	423.2721	423.2721	0.0000	2.8	2.6	8.7
44	N 44° 32' 12.81124"	E 18° 41' 02.54706"	279.6837	279.6837	0.0000	15.2	8.2	15.6
45	N 44° 32' 09.11882"	E 18° 40' 58.72679"	279.0320	279.0320	0.0000	11.7	7.1	15.3
46	N 44° 33' 16.42128"	E 18° 39' 36.84330"	436.2609	436.2609	0.0000	2.9	2.1	5.0
470	N 44° 32' 20.26442"	E 18° 41' 19.02269"	349.3840	349.3840	0.0000	12.5	12.3	47.4

4795	N 44° 32' 15.92627"	E 18° 40' 38.44263"	276.5308	276.5308	0.0000	5.5	4.3	8.3
483	N 44° 32' 35.15051"	E 18° 38' 42.10940"	372.0502	372.0502	0.0000	0.0	0.0	0.0
486	N 44° 31' 31.68437"	E 18° 39' 24.49048"	380.9412	380.9412	0.0000	0.0	0.0	0.0
5042	N 44° 31' 43.14636"	E 18° 41' 42.73706"	291.2990	291.2990	0.0000	0.0	0.0	0.0
52	N 44° 32' 17.74787"	E 18° 40' 54.46802"	274.7535	274.7535	0.0000	22.8	12.4	51.5
531	N 44° 33' 08.21862"	E 18° 40' 39.55835"	332.8744	332.8744	0.0000	15.6	8.1	14.2
54	N 44° 33' 47.90210"	E 18° 40' 12.35430"	460.3607	460.3607	0.0000	0.0	0.0	0.0
55	N 44° 32' 16.31408"	E 18° 40' 45.90880"	275.1793	275.1793	0.0000	8.0	6.9	26.7
552	N 44° 32' 14.53245"	E 18° 41' 14.21556"	297.8558	297.8558	0.0000	8.9	8.0	26.7
59	N 44° 33' 00.32289"	E 18° 40' 00.90341"	290.7626	290.7626	0.0000	5.0	2.5	5.5
62	N 44° 32' 09.43131"	E 18° 40' 46.97713"	277.9525	277.9525	0.0000	13.2	8.5	20.7
623	N 44° 32' 28.64245"	E 18° 41' 02.77950"	341.3701	341.3701	0.0000	5.8	4.0	10.1
633	N 44° 32' 17.07685"	E 18° 41' 06.28969"	284.6106	284.6106	0.0000	13.7	10.1	24.4
85	N 44° 32' 15.39547"	E 18° 40' 26.03528"	275.5455	275.5455	0.0000	5.6	3.5	6.8
95	N 44° 32' 16.43197"	E 18° 40' 42.20642"	274.8471	274.8471	0.0000	14.5	9.0	20.1
DR10	N 44° 32' 36.16873"	E 18° 39' 52.55149"	278.1411	278.1411	0.0000	3.1	1.9	5.5
DR5	N 44° 31' 51.02104"	E 18° 41' 09.33944"	280.2938	280.2938	0.0000	6.2	4.1	10.2
DR6	N 44° 32' 07.02551"	E 18° 40' 40.86969"	277.8989	277.8989	0.0000	8.2	5.3	13.4
DR9	N 44° 32' 07.98839"	E 18° 41' 35.98239"	310.6173	310.6173	0.0000	14.5	6.5	26.8
F1	N 44° 32' 18.35510"	E 18° 40' 36.94349"	274.5479	274.5479	0.0000	8.0	4.0	8.4
F2	N 44° 32' 18.45893"	E 18° 40' 33.73716"	276.7221	276.7221	0.0000	13.5	11.0	27.2

Curvature Calculation MatLab Script (Bergbauer and Pollard, 2003a)

First partial derivatives in x and y

```
% function [dZx, dZy]=firstpartial(Z)
% Matlab script based on the finite-differences technique to
% calculate first partial derivatives in x, dZx, and y, dZy,
% of matrix Z
% calculate dZ/dx
dZx=ones(n,l);
for k=1:n
for i=2:l-1
dZx(k,i)=(Z(k,i+1)-Z(k,i-1))/(2*dx);
end
end
dZx=dZx(2:n-1,2:l-1);
% calculate dZ/dy
dZy=ones(n,l);
for i=1:l
for k=2:n-1
dZy(k,i)=(Z(k+1,i)-Z(k-1,i))/(2*dy);
end
end
dZy=dZy(2:n-1,2:l-1);
clear k I
```

Second partial derivatives in x, y, and mixed partial

```
% function [d2Zx2, d2Zy2, d2Zxy]=secondpartial(Z)
% Matlab code based on the finite-differences technique to
% calculate second partial derivatives in x, d2Zx2, y, d2Zy2, and % mixed partial, d2Zxy,
% of matrix Z
% calculate d2Z/dx2
d2Zx2=ones(n,l);
for k=1:n
for i=2:l-1
d2Zx2(k,i)=-(Z(k,i+1)+Z(k,i-1)-2*Z(k,i))/dx^2;
end
end
d2Zx2=d2Zx2(2:n-1,2:l-1);
% calculate d2Z/dy2
d2Zy2=ones(n,l);
for i=1:l
for k=2:n-1
d2Zy2(k,i)=-(Z(k+1,i)+Z(k-1,i)-2*Z(k,i))/dy^2;
end
end
d2Zy2=d2Zy2(2:n-1,2:l-1);
% calculate d2Z/dxdy
d2Zxy=ones(n,l);
for k=2:n-1
for i=2:l-1
d2Zxy(k,i)=-(Z(k-1,i-1)-Z(k-1,i+1)-Z(k+1,i-1)+Z(k+1,i+1))/
```

```
(4*dx*dy);
end
end
d2Zxy=d2Zxy(2:n-1,2:l-1);
clear k I
```

Normal surface curvature

```
% curvature.m
% Matlab script for the calculation of normal surface curvatures
% Calculates principal magnitudes and directions (Kmax, Kmin, trajmax, trajmin)
% as well as Gaussian curvature, G, mean curvature, M, and shape-curvature L1
% calculating First Fundamental Form
alpha11=ones(size(dZx))+(dZx).^2;
alpha12=(dZx).*(dZy);
alpha22=ones(size(dZx))+(dZy).^2;
% calculating Second Fundamental Form
alpha3=1./(sqrt(alpha11.*alpha22-(alpha12).^2));
beta11=alpha3.*d2Zx2;
beta12=alpha3.*d2Zxy;
beta22=alpha3.*d2Zy2;
% calculating principal directions & principal curvatures
p=zeros(size(dZx));q=p;lambda1=p; lambda2=p;K1=p; K2=p;
a=alpha12.*beta22-alpha22.*beta12;
b=alpha11.*beta22-alpha22.*beta11;
c=alpha11.*beta12-alpha12.*beta11;
a1=find(a~=0);
p(a1)=(b(a1))./(a(a1)); % formulas triple checked
q(a1)=(c(a1))./(a(a1));
lambda1(a1)=-0.5.*p(a1)+sqrt((0.5.*p(a1)).^2-q(a1));
lambda2(a1)=-0.5.*p(a1)-sqrt((0.5.*p(a1)).^2-q(a1));
K1(a1)=(beta11(a1)+2.*beta12(a1).*lambda1(a1)+beta22(a1).*lambda1(a1).^2)./
(alpha11(a1)+2.*alpha12(a1).*lambda1(a1)+alpha22(a1).*lambda1(a1).^2);
K2(a1)=(beta11(a1)+2.*beta12(a1).*lambda2(a1)+beta22(a1).*lambda2(a1).^2)./
(alpha11(a1)+2.*alpha12(a1).*lambda2(a1)+alpha22(a1).*lambda2(a1).^2);
lambda1(a1)=atan(lambda1(a1));
lambda2(a1)=atan(lambda2(a1));
% find zero components (cylinder parallel to x)
a2=find(a==0);
lambda1(a2)=-alpha12(a2)./alpha22(a2);
lambda1(a2)=atan(lambda1(a2));
lambda2(a2)=lambda1(a2)+pi/2;
K1(a2)=(beta11(a2))./(alpha11(a2)-2.*(alpha12(a2).^2./alpha22(a2))+alpha12(a2).^2./
alpha22(a2));
K2(a2)=0;
d=find(a==0 & c==0);
lambda2(d)=zeros(size(d));
lambda1(d)=0.5*pi.*ones(size(d));
K2(d)=beta11(d)./alpha11(d);
K1(d)=beta22(d)./alpha22(d);
% find umbilical points
```

```
e=find(a==0 & b==0 & c==0);
if length(e)>0
E=(‘umbilical points’)
length(e)
end
% sort results into Kmin and Kmax, trajmax and trajmin
k=find(K1>=K2);
Kmin=K1; Kmax=K2; trajmin=lambda1; trajmax=lambda2;
Kmin(k)=K2(k);
Kmax(k)=K1(k);
trajmin(k)=lambda2(k);
trajmax(k)=lambda1(k);
% threshold curvature below which it is assumed zero
i=find(abs(Kmin)<kl);
Kmin(i)=0;
i=find(abs(Kmax)<kl);
Kmax(i)=0;
% Gaussian, mean, and shape-curvature
G=Kmax.*Kmin;
%G=(beta11.*beta22-beta12.^2)./(alpha11.*alpha22-alpha12.^2);
e=find(G<0);
f=find(G>0);
G1=G;
G1(e)=-1.*ones(size(e));
G1(f)=ones(size(f));
M=0.5.*(Kmax+Kmin);
%M=(alpha11.*beta22+alpha22.*beta11-2.*alpha12.*beta12)./(2.*alpha11.*alpha22-
alpha12.^2);
e=find(M<0);
f=find(M>0);
M1=M;
M1(e)=-1.*ones(size(e));
M1(f)=ones(size(f));
L1=G1;
e=find(G1<0);
L1(e)=-3.*ones(size(e));
e=find(G1==0 & M1>0);
L1(e)=-1.*ones(size(e));
e=find(G1==0 & M1<0);
L1(e)=ones(size(e));
e=find(G1>0 & M1>0);
L1(e)=-2.*ones(size(e));
e=find(G1>0 & M1<0);
L1(e)=2.*ones(size(e));
% normal vector
Nz=alpha3; % normal vector
Nx=-dZx.*alpha3;
Ny=-dZy.*alpha3;
clear alpha11 alpha12 alpha22 alpha3 beta11 beta12 beta22 p a b c a1 a2 d k e f K1 K2
lambda1 lambda2
```